

University of Windsor

## Scholarship at UWindor

---

Electronic Theses and Dissertations

Theses, Dissertations, and Major Papers

---

1-24-2019

# Two-Phase Flows With Dynamic Contact Angle Effects For Fuel Cell Applications

Mengcheng Jiang  
*University of Windsor*

Follow this and additional works at: <https://scholar.uwindsor.ca/etd>

---

### Recommended Citation

Jiang, Mengcheng, "Two-Phase Flows With Dynamic Contact Angle Effects For Fuel Cell Applications" (2019). *Electronic Theses and Dissertations*. 7640.  
<https://scholar.uwindsor.ca/etd/7640>

This online database contains the full-text of PhD dissertations and Masters' theses of University of Windsor students from 1954 forward. These documents are made available for personal study and research purposes only, in accordance with the Canadian Copyright Act and the Creative Commons license—CC BY-NC-ND (Attribution, Non-Commercial, No Derivative Works). Under this license, works must always be attributed to the copyright holder (original author), cannot be used for any commercial purposes, and may not be altered. Any other use would require the permission of the copyright holder. Students may inquire about withdrawing their dissertation and/or thesis from this database. For additional inquiries, please contact the repository administrator via email ([scholarship@uwindsor.ca](mailto:scholarship@uwindsor.ca)) or by telephone at 519-253-3000ext. 3208.

**TWO-PHASE FLOWS WITH DYNAMIC CONTACT ANGLE EFFECTS FOR  
FUEL CELL APPLICATIONS**

By

Mengcheng Jiang

A Thesis

Submitted to the Faculty of Graduate Studies  
through the Department of Mechanical, Automotive & Materials Engineering  
in Partial Fulfillment of the Requirements for  
the Degree of Master of Applied Science  
at the University of Windsor

Windsor, Ontario, Canada

2019

© 2019 Mengcheng Jiang

**TWO-PHASE FLOWS WITH DYNAMIC CONTACT ANGLE EFFECTS FOR  
FUEL CELL APPLICATIONS**

by

Mengcheng Jiang

APPROVED BY:

---

S. Cheng

Department of Civil and Environmental Engineering

---

J. Defoe

Department of Mechanical, Automotive & Materials Engineering

---

B. Zhou, Advisor

Department of Mechanical, Automotive & Materials Engineering

January 7, 2019

## DECLARATION OF CO-AUTHORSHIP / PREVIOUS PUBLICATION

### I. Co-Authorship

I hereby declare that this thesis incorporates material that is result of joint research. Chapter 2 of the thesis (*Comparisons and validations of contact angle models*) was co-authored with Dr. Biao Zhou and Xichen Wang. For this paper, Dr. Zhou contributed to the refinement of main ideas, the follow-up discussions and the revision of the manuscript. Xichen Wang assisted in the initial numerical model set up. Part of Chapter 3 in this thesis (*Numerical Study of Droplet Impact on Inclined Surface: Viscosity Effects*) was co-authored with Dr. Zhou and presented at Fuel Cell Seminar & Energy Exposition on November 9, 2017 at Long Beach, California.

I am aware of the University of Windsor Senate Policy on Authorship and I certify that I have properly acknowledged the contribution of other researchers to my thesis, and have obtained written permission from each of the co-author(s) to include the above material(s) in my thesis.

I certify that, with the above qualification, this thesis, and the research to which it refers, is the product of my own work.

### II. Previous Publication

This thesis includes two original papers that have been previously published/submitted for publication in peer reviewed journals/conference proceedings, as follows:

Thesis Chapter	Publication title/full citation	Publication status
<i>Chapter 2</i>	Jiang M, Zhou B, Wang X. Comparisons and validations of contact angle models. International Journal of Hydrogen Energy. 2018 Mar 22;43(12):6364-78. <i>doi: 10.1016/j.ijhydene.2018.02.016</i>	<i>Published</i>

<i>Chapter 3</i> <i>(partial)</i>	Jiang M, Zhou B. Numerical Study of Droplet Impact on Inclined Surface: Viscosity Effects. ECS Transactions. 2018 Jan 4;83(1):127-36. <i>doi: 10.1149/08301.0127ecst</i>	<i>Published</i>
--------------------------------------	---	------------------

I certify that I have obtained a written permission from the copyright owner(s) to include the above published material(s) in my thesis. I certify that the above material describes work completed during my registration as a graduate student at the University of Windsor.

### **III. General**

I declare that, to the best of my knowledge, my thesis does not infringe upon anyone's copyright nor violate any proprietary rights and that any ideas, techniques, quotations, or any other material from the work of other people included in my thesis, published or otherwise, are fully acknowledged in accordance with the standard referencing practices. Furthermore, to the extent that I have included copyrighted material that surpasses the bounds of fair dealing within the meaning of the Canada Copyright Act, I certify that I have obtained a written permission from the copyright owner(s) to include such material(s) in my thesis.

I declare that this is a true copy of my thesis, including any final revisions, as approved by my thesis committee and the Graduate Studies office, and that this thesis has not been submitted for a higher degree to any other University or Institution.

## ABSTRACT

Liquid water management is still a very critical challenge in the commercialization of proton exchange membrane fuel cell (PEMFC). Fundamental understanding of two-phase flow behaviors is of crucial importance to the investigation of water management issues. Recently, it has been noted that the dynamic contact angle (DCA) plays a critical role in the two-phase flow simulations and the conventional static contact angle (SCA) model has obvious limitations in the prediction of droplet behaviors. This thesis mainly focuses on the numerical modeling and simulation of two-phase flow problems with dynamic contact angle (DCA) and is presented by four papers. The first paper proposes and validates an advancing-and-receding DCA (AR-DCA) model that is able to predict both advancing and receding dynamic contact angles using Hoffman function (*Chapter 2*). In the second paper, the AR-DCA model is further applied to simulate droplet behaviors on inclined surfaces with different impact velocities, impact angles and droplet viscosities (*Chapter 3*). The third paper introduces a methodology to improve the evaluation method of contact line velocity in the AR-DCA model and an improved-AR-DCA (i-AR-DCA) model is developed (*Chapter 4*). The last paper presents different flow regimes in a single straight microchannel under various air and water inlet flow rates (*Chapter 5*).

## DEDICATION

*To my parents, my family and close friends*

*and*

*To the memory of my loving grandmother*

## ACKNOWLEDGEMENTS

I would first like to express my sincerest thanks to my supervisor, Dr. Biao Zhou, for providing me the opportunity to pursue my Master degree at the University of Windsor and Clean Powertrain Lab. His guidance, patience and inspiration lead me to the right direction for my research during my master study. I would also like to express my deep gratitude to all my committee members, Dr. Jeff Defoe and Dr. Shaohong Cheng, for their insightful comments and suggestions on my thesis; Dr. Shahpour Alirezaee, for serving as the chair of my oral defense.

I am also very grateful for Compute Canada and Sharcnet for providing computing resources which greatly accelerated the simulation progress and made this research possible. I would also like to acknowledge the support from the Natural Sciences and Engineering Research Council of Canada (NSERC), the Clean Rail Academic Grant Program from Transport Canada, and the University of Windsor.

Special appreciation goes to my colleagues in Dr. Zhou's research group, especially Iman Azarian Borojeni, and all my close friends in Windsor. Thank you for your encouragement and companion in these years, which comfort me a lot and help me face the challenges in my study and life.

Finally, I would like to express my heartfelt gratitude to my family and my parents. Mom and Dad, thank you for your unconditional love. I would not be able to complete this work without your support, care and patience.



## TABLE OF CONTENTS

DECLARATION OF CO-AUTHORSHIP / PREVIOUS PUBLICATION .....	iii
ABSTRACT .....	v
DEDICATION .....	vi
ACKNOWLEDGEMENTS .....	vii
LIST OF TABLES .....	xi
LIST OF FIGURES .....	xii
LIST OF ABBREVIATIONS/SYMBOLS .....	xvii
NOMENCLATURE .....	xviii
CHAPTER 1 INTRODUCTION .....	1
1.1. Proton Exchange Membrane Fuel Cell .....	1
1.2. Water Management and Two-phase Flow in Proton Exchange Membrane Fuel Cells ...	2
1.3. Contact Angle Definition and Dynamic Contact Angle .....	4
1.4. Challenges.....	5
1.5. Objectives and Thesis Overview.....	6
References.....	8
CHAPTER 2 COMPARISONS AND VALIDATIONS OF CONTACT ANGLE MODELS .....	12
2.1. Introduction.....	12
2.1.1. Dynamic Contact Angle Formulation – Hoffman function .....	12
2.1.2. Numerical Studies on Dynamic Contact Angle .....	14
2.1.3. Summary .....	16
2.2. Fundamental Understanding of Hoffman Function .....	18
2.3. Numerical Methodology .....	19
2.3.1. Governing Equations with Volume of Fluid (VOF) Method.....	20
2.3.2. Implementation of Contact Angle Models.....	21
2.4. Numerical Model Description.....	22
2.4.1. Experiments for Validation.....	22
2.4.2. Computational Domain and Input Parameters .....	23
2.4.3. Mesh Independency .....	25
2.5. Results and Discussion .....	27
2.5.1. Qualitative Results .....	27

2.5.2. Quantitative Results .....	35
2.6. Conclusions.....	39
Acknowledgements.....	42
References.....	42
 CHAPTER 3 DROPLET BEHAVIORS ON INCLINED SURFACES WITH DYNAMIC CONTACT ANGLES .....	46
3.1. Introduction.....	46
3.2. Numerical Methodology .....	49
3.3. Numerical Model Description.....	49
3.3.1. Experiments for Validation.....	49
3.3.2. Computational Domain and Grid Independency.....	51
3.4. Results and Discussion .....	51
3.4.1. Effects of Impact Velocity .....	51
3.4.2. Effects of Impact Angle .....	56
3.4.3. Effects of Droplet Viscosity.....	60
3.5. Conclusions.....	66
References.....	68
 CHAPTER 4 IMPROVEMENT AND FURTHER INVESTIGATION ON HOFFMAN- FUNCTION-BASED DYNAMIC CONTACT ANGLE MODEL .....	72
4.1. Introduction.....	72
4.2. Numerical Methodology .....	75
4.2.1. Governing Equations and Dynamic Contact Angle .....	75
4.2.2. Modification of the Evaluation Method of Contact Line Velocity .....	75
4.3. Numerical Model Description.....	77
4.3.1. Computational Domain and Boundary Conditions .....	77
4.3.2. Grid Independency.....	78
4.4. Results and Discussion .....	80
4.4.1. Droplet Impact on Inclined Surface .....	80
4.4.2. Liquid Water Behaviors in a Single Straight Microchannel .....	84
4.5. Conclusions.....	85
References.....	86
 CHAPTER 5 NUMERICAL STUDY OF FLOW REGIMES IN MICROCHANNEL WITH DYNAMIC CONTACT ANGLE.....	90
5.1. Introduction.....	90
5.2. Numerical Model Description.....	94
5.2.1. Computational Domain and Boundary Conditions .....	94

5.2.2.	Governing Equations and Dynamic Contact Angle .....	95
5.2.3.	Grid Independency .....	96
5.3.	Results and Discussion .....	96
5.3.1.	Liquid Water Behaviors under Different Water Inlet Flow Rates .....	97
5.3.2.	Liquid Water Behaviors under Different Air Inlet Flow Rates.....	102
5.4.	Conclusions.....	105
	References.....	106
CHAPTER 6 CONCLUSIONS AND FUTURE WORKS.....		110
6.1.	Summary and Conclusions .....	110
6.2.	Recommendations and Future Works .....	112
APPENDICES .....		114
<i>Appendix A</i> .....		114
NUMERICAL SIMULATION OF LIQUID WATER BEHAVIORS IN MICROCHANNEL USING THE MULTI-FLUID VOLUME OF FLUID METHOD .....		114
A.1.	Introduction.....	114
A.2.	Numerical Model Description.....	117
A.2.1.	Computational Domain and Boundary Conditions .....	117
A.2.2.	Numerical Methodology .....	118
A.3.	Preliminary Results and Discussion.....	121
A.4.	Summary and Future Work.....	123
	References.....	123
<i>Appendix B</i> .....		128
PERMISSIONS FOR PREVIOUS PUBLISHED WORKS .....		128
VITA AUCTORIS .....		130

## LIST OF TABLES

Table 2.1: Correlations Used in DCA Simulations from Available Literature.....	17
Table 2.2: Detailed Liquid Property, Surface Wettability and Impact Velocity for Selected Cases .....	23
Table 2.3: Simulation Parameters for Selected Cases .....	24
Table 2.4: Information of Different Grid Resolutions in the Present Study .....	25
Table 3.1 Detailed Liquid Property, Surface Wettability and Impact Velocity for Selected Cases [15] .....	50
Table 3.2 Calculation Results for the Viscosity of the Glycerin Solution based on Refutas Equation.....	63
Table 4.1: Information of Different Grid Resolutions for Microchannel Domain .....	79
Table 4.2: Comparison of Numerical Results under Different Grid Resolutions ( $Re =$ $49.2$ , $Ca = 0.0023$ ) .....	80
Table 5.1: Comparison of Liquid Water Behavior between the Numerical Simulation and Experimental Visualization [16] under $Ca = 0.011$ .....	97
Table 5.2: Simulation Cases under Various Water Inlet Flow Rates with Fixed Air $Re$ $66.6$ .....	98

## LIST OF FIGURES

Figure 1.1: Schematic of a PEMFC [3]. .....	2
Figure 1.2: Definition of contact angle. ....	4
Figure 2.1: Dynamic contact angle evolution map. ....	19
Figure 2.2: Schematic of droplet impact on a surface [25].....	22
Figure 2.3: (a) Schematic of computational domain used in the numerical simulation; (b) Schematic of the droplet initial and impact position in the computational domain (side-view). ....	24
Figure 2.4: Effects of computational domain size on the numerical results: (a) Case 1; (b) Case 2.....	25
Figure 2.5: Numerical results of Case 1 under different grid resolution: (a) grid resolution type A; (b) grid resolution type B; (c) grid resolution type C; (d) grid resolution type D.....	26
Figure 2.6: Numerical results of Case 2 under different grid resolution: (a) grid resolution type A; (b) grid resolution type B; (c) grid resolution type C; (d) grid resolution type D.....	27
Figure 2.7: Comparison of numerical and experimental results for Case 1 (side-view). (a) Experiment at 0.100, 0.260, 2.020 ms (last three profiles) after impact [34]; (b) A-DCA model (c) AR-DCA model. (d) SCA model.....	28
Figure 2.8: Comparison of numerical results for Case 1 (3D-view). (a) A-DCA model; (b) AR-DCA model; (c) SCA model.....	29
Figure 2.9: Comparison of numerical and experimental results for Case 2 (side-view). (a) Experiment [34]; (b) A-DCA model; (c) AR-DCA model; (d) SCA model. ....	30
Figure 2.10: Comparison of numerical results for Case 2 (3D-view). (a) A-DCA model; (b) AR-DCA model; (c) SCA model. ....	30
Figure 2.11: Comparison of numerical and experimental results for Case 3 (side-view) (a) Experiment [25]; (b) A-DCA model; (c) AR-DCA model; (d) SCA model. ....	32

Figure 2.12: Comparison of numerical results for Case 3 (3D-view) (a) A-DCA model; (b) AR-DCA model; (c) SCA model. ....	33
Figure 2.13: Comparison of numerical and experimental results for Case 4 (side-view) (a) Experiment [25]; (b) A-DCA model; (c) AR-DCA model; (d) SCA model. 34	
Figure 2.14: Comparison of numerical results for Case 4 (3D-view) (a) A-DCA model; (b) AR-DCA model; (c) SCA model. ....	34
Figure 2.15: Comparisons of the spreading factor $x/D$ (left column) and dimensionless droplet spreading length $l/D$ (right column). (a) Case 2; (b) Case 3; (c) Case 4. ....	36
Figure 3.1: Impact of water droplet on smooth glass with $\alpha = 10^\circ$ and different impact velocities (Left side: experiment from Sikalo [15]; Right side: numerical results in the present study): (a) $We = 50$ , $t = 0, 1, 2, 9$ ms; (b) $We = 161$ , $t = 0,$ $1, 2, 5$ ms; (c) $We = 391$ , $t = 0, 1, 2$ ms. ....	52
Figure 3.2: Impact of water droplet on wax with $\alpha = 10^\circ$ and different impact velocities (Left side: experiment from Sikalo [15]; Right side: numerical results in the present study): (a) $We = 50$ , $t = 0, 1, 2, 9$ ms; (b) $We = 161$ , $t = 0, 1, 2, 5$ ms; (c) $We = 391$ , $t = 0, 1, 2$ ms. ....	53
Figure 3.3: Comparison of spreading factor under different impact velocities ( $We = 50,$ $161, 391$ ) for water droplet impact on $10^\circ$ smooth glass: a) simulation and b) experiment [15]. ....	54
Figure 3.4: Comparison of dimensionless spreading length under different impact velocities ( $We = 50, 161, 391$ ) for water droplet impact on $10^\circ$ smooth glass (simulation). ....	54
Figure 3.5: Comparison of spreading factor under different impact velocities ( $We = 50,$ $161, 391$ ) for water droplet impact on $10^\circ$ wax: a) simulation and b) experiment [15]. ....	55
Figure 3.6: Comparison of dimensionless spreading length under different impact velocities ( $We = 50, 161, 391$ ) for water droplet impact on $10^\circ$ wax (simulation). ....	56

Figure 3.7: Impact of water droplet on smooth glass with $We = 50$ and different impact angle $\alpha$ (Left side: experiment from Sikalo [15]; Right side: numerical results in the present study): (a) $\alpha = 9.5^\circ$ ; $t = 0, 2, 4, 6, 8$ ms; (b) $\alpha = 10^\circ$ ; $t = 0, 1, 2, 9$ ms; (c) $\alpha = 20^\circ$ ; $t = 0, 1, 2, 9$ ms. ....	57
Figure 3.8: Impact of water droplet on wax with $We = 50$ and different impact angle $\alpha$ (Left side: experiment from Sikalo [15]; Right side: numerical results in the present study): (a) $\alpha = 5^\circ$ ; $t = 0, 2, 4, 6, 8$ ms; (b) $\alpha = 10^\circ$ ; $t = 0, 1, 2, 9$ ms; (c) $\alpha = 20^\circ$ ; $t = 0, 1, 2, 9$ ms. ....	58
Figure 3.9: Comparison of spreading factor under different impact angles ( $\alpha = 9.5^\circ, 10^\circ, 20^\circ$ ) for water droplet impact on smooth glass with $We = 50$ : a) simulation and b) experiment [15].....	59
Figure 3.10: Comparison of dimensionless spreading length different impact angles ( $\alpha = 9.5^\circ, 10^\circ, 20^\circ$ ) for water droplet impact on smooth glass with $We = 50$ (simulation).....	59
Figure 3.11: Comparison of spreading factor under different impact angles ( $\alpha = 5^\circ, 10^\circ, 20^\circ$ ) for water droplet impact on wax with $We = 50$ : a) simulation and b) experiment [15].....	60
Figure 3.12: Comparison of dimensionless spreading length different impact angles ( $\alpha = 5^\circ, 10^\circ, 20^\circ$ ) for water droplet impact on wax with $We = 50$ (simulation)....	60
Figure 3.13: Impact of glycerin droplet onto wax with $We = 391$ : (a) droplet partial rebound in the experiment [15]; (b) droplet deposition in the experiment [15]; (c) simulation results.....	61
Figure 3.14: Comparison of numerical results with different viscosities (side-view): a) $\mu^*$ ; b) $1.5\mu^*$ ; c) $2\mu^*$ ; d) $3\mu^*$ .....	64
Figure 3.15: Comparison of numerical results with different viscosities (3D-view): a) $\mu^*$ ; b) $1.5\mu^*$ ; c) $2\mu^*$ ; d) $3\mu^*$ . ....	64
Figure 3.16: Comparison of a) spreading factors and b) dimensionless spreading length ( $l/D$ ) for glycerin droplet with different viscosities impact on smooth glass.	66

Figure 4.1: Contact angle at the interaction of gas, liquid and solid phases.....	72
Figure 4.2: Evaluation of contact line velocity in the previous works [15, 16, 20].....	74
Figure 4.3: Schematic of contact line velocity evaluation in AR-DCA model (a) and modification (b). .....	77
Figure 4.4: Schematic of computational domains used in the present study: (a) droplet impact on inclined surface; (b) liquid water behaviors in a single straight microchannel.....	78
Figure 4.5: Schematic of a liquid water slug in microchannel with the length $l$ and height $h$ . .....	79
Figure 4.6: Comparison of the ratio of water slug length to height ( $l/h$ ) under different grid resolution.....	80
Figure 4.7: Comparison of numerical results for water droplet impact on wax (Case 3 in Ref. [20]) from AR-DCA and i-AR-DCA models. ....	81
Figure 4.8: Comparison of numerical results for water droplet impact on wax (Case 4 in Ref. [20]) from AR-DCA and i-AR-DCA models. ....	82
Figure 4.9: Comparison of the spreading factor $x/D$ from AR-DCA and i-AR-DCA models: (a) water droplet impact on smooth glass (Case 3 in Ref. [20]); (b) water droplet impact on wax (Case 4 in Ref. [20]).....	82
Figure 4.10: Comparison of contact angles at the leading and trailing edges from AR- DCA and i-AR-DCA models: (a) water droplet impact on smooth glass (Case 3 in Ref. [20]); (b) water droplet impact on wax (Case 4 in Ref. [20]). .....	83
Figure 4.11: Comparison of liquid water evolvement process based on AR-DCA and i- AR-DCA models ( $Re = 66.6$ , $Ca = 0.0023$ ).....	85
Figure 4.12: Comparison of the ratio of water slug length to height ( $l/h$ ) before detachment under AR-DCA and i-AR-DCA models. ....	85
Figure 5.1: Schematic of computational domain for microchannel.....	95



Figure 5.2: Liquid water evolvment (squeezing flow) at $V_{\text{air}} = 10.7 \text{ m/s}$ ( $Re = 66.6$ ) under various water injection rates: (a) $5 \text{ } \mu\text{L/min}$ ( $Ca = 0.0011$ ); (b) $10 \text{ } \mu\text{L/min}$ ( $Ca = 0.0023$ ).	99
Figure 5.3: Liquid water evolvment (partial-jetting flow) at $V_{\text{air}} = 10.7 \text{ m/s}$ ( $Re = 66.6$ ) and water injection rate $15 \text{ } \mu\text{L/min}$ ( $Ca = 0.0034$ ).	100
Figure 5.4: Liquid water evolvment (squeezing flow) at $V_{\text{air}} = 10.7 \text{ m/s}$ ( $Re = 66.6$ ) under various water injection rates: (a) $20 \text{ } \mu\text{L/min}$ ( $Ca = 0.0046$ ); (b) $25 \text{ } \mu\text{L/min}$ ( $Ca = 0.0057$ ); (c) $30 \text{ } \mu\text{L/min}$ ( $Ca = 0.0069$ ); (d) $50 \text{ } \mu\text{L/min}$ ( $Ca = 0.011$ ).	101
Figure 5.5: Liquid water evolvment under different air inlet velocities at $Q_{\text{water}} = 5 \text{ } \mu\text{L/min}$ ( $Ca = 0.0011$ ): (a) $V_{\text{air}} = 4.8 \text{ m/s}$ ( $Re = 29.9$ ) (b) $V_{\text{air}} = 10.7 \text{ m/s}$ ( $Re = 66.6$ ), (c) $V_{\text{air}} = 18.1 \text{ m/s}$ ( $Re = 112.7$ ).	103
Figure 5.6: Liquid water evolvment under different air inlet velocities at $Q_{\text{water}} = 10 \text{ } \mu\text{L/min}$ ( $Ca = 0.0023$ ): (a) $V_{\text{air}} = 4.8 \text{ m/s}$ ( $Re = 29.9$ ) (b) $V_{\text{air}} = 10.7 \text{ m/s}$ ( $Re = 66.6$ ), (c) $V_{\text{air}} = 18.1 \text{ m/s}$ ( $Re = 112.7$ ).	104
Figure 5.7: Liquid water evolvment under different air inlet velocities at $Q_{\text{water}} = 25 \text{ } \mu\text{L/min}$ ( $Ca = 0.0057$ ): (a) $V_{\text{air}} = 4.8 \text{ m/s}$ ( $Re = 29.9$ ) (b) $V_{\text{air}} = 10.7 \text{ m/s}$ ( $Re = 66.6$ ), (c) $V_{\text{air}} = 18.1 \text{ m/s}$ ( $Re = 112.7$ ).	105
Figure A.1: Schematic of computational domain for microchannel.	118
Figure A.2: Numerical results of liquid water evolvment based on the VOF method (left column) and the multi-fluid VOF method (right column).	122
Figure A.3: Comparison of the ratio of water slug length to height ( $l/h$ ) before detachment of the first slug from VOF model and multi-fluid VOF model.	122

## LIST OF ABBREVIATIONS/SYMBOLS

### *Abbreviations*

A-DCA	Advancing dynamic contact angle
AR-DCA	Advancing-receding dynamic contact angle
CL	Catalyst layer
CFD	Computational fluid dynamics
DCA	Dynamic contact angle
GDL	Gas diffusion layer
i-AR-DCA	Improved advancing-receding dynamic contact angle
PEMFC	Proton exchange membrane fuel cell
SCA	Static contact angle
UDF	User defined function
VBN	Viscosity bending number
VOF	Volume of fluid

### *Greek symbols*

$\alpha$	Inclined angle of surface
$\gamma$	Surface tension
$\theta$	Contact angle
$\kappa$	Surface curvature
$\mu$	Dynamic viscosity
$\rho$	Density
$\nu$	Kinematic viscosity

## NOMENCLATURE

$Ca$	Capillary number
$Co$	Courant number
$D$	Initial droplet diameter
$d_0$	Droplet falling distance
$F$	Shift factor
$f_{Hoff}$	Hoffman function
$f_{Hoff}^{-1}$	Inverse of Hoffman function
$H_c$	Height of the microchannel
$L_c$	Length of the microchannel
$l$	Droplet spreading length
$Re$	Reynolds number
$S$	Source term
$s$	Phase volume fraction
$t^*$	Dimensionless time for cases of droplet impact on surfaces
$t_a$	Dimensionless time for microchannel cases (under same air inlet velocity)
$t_w$	Dimensionless time for microchannel cases (under same water inlet velocity)
$\vec{u}$	Velocity vector
$V_0$	Droplet initial velocity
$V_{cl}$	Contact line velocity
$V_i$	Interface velocity
$V_p$	Droplet impact velocity
$We$	Weber number

***Subscripts***

<i>LG</i>	liquid/gas interface
<i>SG</i>	Solid/gas interface
<i>SL</i>	Solid/liquid interface
<i>a</i>	Advancing
<i>cl</i>	Contact line
<i>d</i>	Dynamic
<i>e</i>	Equilibrium
<i>g</i>	Gas phase
<i>l</i>	Liquid phase
<i>m</i>	Momentum
<i>r</i>	Receding
<i>s</i>	Static

# CHAPTER 1

## INTRODUCTION

### 1.1. Proton Exchange Membrane Fuel Cell

Fuel cells are energy conversion devices that produce electricity through electrochemical reaction. Generally, a fuel cell consists of three components: 1) Anode, an electrode where the oxidation reaction occurs and the electrons are released in the process; 2) Cathode, an electrode where the reduction reaction occurs and the electrons are consumed in the process; 3) Electrolyte, a substance that only allows ions to pass through instead of electrons. One of the remarkable distinctions of fuel cells to the conventional power sources (batteries, combustion engines) is that fuel cells can be recharged directly by refueling rather than the time-consuming charging (plugged in) like batteries. Also, fuel cells are far more efficient and environmentally friendly than combustion engines [1].

In general, fuel cells can be classified into the following major categories: 1) Proton exchange membrane or Polymer Electrolyte Membrane fuel cell (PEMFC); 2) Direct methanol fuel cell (DMFC); 3) Alkaline fuel cell (AFC); 4) Phosphoric acid fuel cell (PAFC); 5) Molten carbonate fuel cell (MCFC); 6) Solid-oxide fuel cell (SOFC) [2]. In recent years, PEMFCs have received extensive attentions due to their abilities such as quick start-up, frequent start-and-stop, low operating temperature, quietness and high power density. These notable features of PEMFCs make them as one of the most promising and suitable energy power sources for transportation, portable and stationary applications [3].

Figure 1.1 shows a schematic of a PEMFC and the basic PEMFC operation process can be described as follows: on the anode side, hydrogen is delivered as fuel and electrons are separated from protons ( $H^+$ ) through electrochemical reaction on the catalyst surface; then the protons will flow through the electrolyte (polymer membrane) to the cathode side whereas the electrons ( $e^-$ ) will flow through external circuit and generate the electricity; on the cathode side, the electrons recombine with protons and oxygen to produce water. The two electrochemical half reactions in a PEMFC are as follows [1]:

Anode side (Oxidation):  $H_2 \rightleftharpoons 2H^+ + 2e^-$

Cathode side (Reduction):  $\frac{1}{2} O_2 + 2H^+ + 2e^- \rightleftharpoons H_2O$

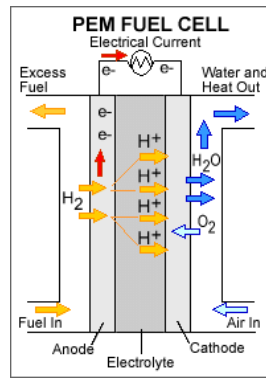


Figure 1.1: Schematic of a PEMFC [3].

## 1.2. Water Management and Two-phase Flow in Proton Exchange Membrane Fuel Cells

Although PEMFCs have numerous advantages compared to the conventional power sources, there are still many technical barriers that prevent PEMFCs from commercialization and broad applicability, mainly in durability, cost and performance [2]. Water management has significant effects on PEMFC performance and is one of the most critical challenges in recent research progress. On one hand, liquid water is needed to ensure the membrane is hydrated enough so that good proton conductivity is

maintained [4]; on the other hand, excessive water may block the pores of the gas diffusion layer (GDL) and the catalyst layer (CL) and cause the flooding issues, which consequently limits the mass transport of reactant. Therefore, it is very important to maintain a proper balance between membrane humidification and liquid water flooding in order to optimize PEMFC performance.

Numerical modeling and simulation based on computational fluid dynamics (CFD) are promising approaches to obtain basic understanding on liquid water behaviors in PEMFCs, especially in gas flow channels [5], which help conquer the difficulties in performing experiments. Over the last decades, several numerical models have been employed to investigate two-phase flow phenomena in PEMFCs, such as the multi-phase mixture (M2) model, the multi-fluid model, Lattice Boltzmann method, the level set method, the volume of fluid (VOF) method, etc. The most recent comprehensive review and summary of these models have been reported by Ferreira et al. [5] and Anderson et al. [6]. Among these numerical models, the VOF method is considered as the most popular approach because it is capable of simulating immiscible fluid and effectively tracking the gas-liquid interface so that the liquid water distribution and transport can be well described. Zhou's research group at the University of Windsor pioneered the numerical study on two-phase flow in PEMFCs using VOF method with the first study in this area by Quan et al. [7] in 2005. Afterwards, numerous works have been reported for two-phase flow and water management simulations in PEMFCs [8-18].

However, among the available literature, it is found that the static contact angle (SCA) is generally used as wall boundary condition while very limited amount of works consider dynamic contact angle (DCA) for two-phase flow simulation in PEMFC with complex

flow field. In order to apply DCA in PEMFC simulations, first, it is very important to understand the fundamentals of DCA.

### 1.3. Contact Angle Definition and Dynamic Contact Angle

The contact angle, i.e., the angle between the liquid/gas interface and the solid surface (Figure 1.2), plays an important role in gas-liquid dynamics. The value of the contact angle is determined by the relationship of interfacial energy among the three phases (gas, liquid, and solid) at the equilibrium state [19]. The state of equilibrium has the property of not varying so long as the external conditions remain unchanged [20]. Therefore, Young's equation [19] can be used to describe the contact angle:

$$\gamma_{LG} \cos \theta_e = \gamma_{SG} - \gamma_{SL} \quad (1.1)$$

where  $\theta_e$  is the contact angle at equilibrium, and  $\gamma_{LG}$ ,  $\gamma_{SG}$ , and  $\gamma_{SL}$  are the surface tension of the liquid/gas interface, the solid/gas interface, and the solid/liquid interface, respectively. In the case of a droplet resting on a flat surface, the contact angle is referred to as the static contact angle (SCA),  $\theta_s$ . If a small enough amount of liquid is added to/removed from a drop, while the contact line does not move, the contact angle will increase/decrease. Before the contact line starts to move, the maximum contact angle is the advancing contact angle,  $\theta_a$ , whereas the minimum is the receding contact angle,  $\theta_r$ . The contact angle  $\theta_e$  is somewhere between  $\theta_a$  and  $\theta_r$ , and the difference between  $\theta_a$  and  $\theta_r$ , i.e.,  $(\theta_a - \theta_r)$ , is usually defined as the contact angle hysteresis.

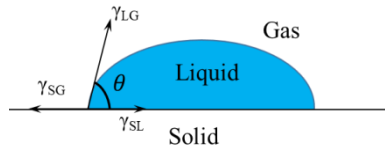


Figure 1.2: Definition of contact angle.



However, in many practical applications involving droplets, the surrounding gas will flow around and interact with the droplets, thus the contact angle is unlikely to stay at static equilibrium and will become dynamic contact angle (DCA). In general, SCA is a property of the gas-liquid and surfaces whereas DCA is influenced by both gas-liquid and surface properties and the gas-liquid interactions. In the gas-liquid two-phase flow modeling and simulation, as a critical parameter at the surface boundaries, DCA rather than SCA should be used.

#### **1.4. Challenges**

Based on the literature review, it is known that the numerical simulation based on the VOF method is a very promising and powerful research tool in the investigation of water management issues in PEMFCs. However, a general DCA model that is able to well predict the gas-liquid phenomena in PEMFCs needs to be further developed, and the complex flow field design of the PEMFC cathode brings about significant challenges in the DCA implementation method and evaluation process. Over the past few years, the DCA simulations have been conducted to investigate droplet behaviors on a single surface or in a microchannel [21-25], which provides an alternative approach that some simple geometry can be used as computational domain at first in the DCA model development. Among the available literature, Hoffman function (an empirical correlation for DCA, also known as Kistler's law) has been considered as a promising formula to predict the DCA value [26-31]. However, a proper manner to implement the Hoffman function still needs to be clarified. Also, some previous studies [29, 31] indicated that the Hoffman function has some obvious limitations in the simulation of gas-liquid behaviors in microchannels, e.g., the droplet detachment is earlier than that observed in the

experiments. Therefore, some necessary modifications for the DCA model implemented with Hoffman function should be further conducted.

## **1.5. Objectives and Thesis Overview**

This thesis is aimed to develop a more robust DCA model that is capable of simulating liquid water behaviors on surfaces or in microchannels and understand the two-phase flow behaviors. The contents of each chapter are summarized as follows:

### **Chapter 1**

The background of this research is introduced, including the basic knowledge of PEMFC and its category, water management problems in PEMFC, definition of contact angle and the difference between SCA and DCA, the challenges in the current research progress, objectives of this research and the organization of the thesis.

### **Chapter 2**

In this chapter, a DCA evolution map is created based on Hoffman function and related experiments to better understand the DCA evolving mechanism; based on this evolution map, the Advancing-Receding DCA (AR-DCA) model is proposed and explained, in addition to the Advancing DCA (A-DCA) model that is based on the original Hoffman's experiments; using user defined function (UDF), the A-DCA and AR-DCA models are implemented with Volume of Fluid (VOF) method in ANSYS Fluent; a series of numerical simulations are conducted with the SCA, A-DCA and AR-DCA models for droplet impact on horizontal and inclined surfaces; the validations of these contact angle models are performed, qualitatively and quantitatively, by comparing the numerical simulation results with the corresponding experimental results from the literature.

### **Chapter 3**

The validated AR-DCA model is further applied to simulate droplet behaviors on inclined surfaces with different droplet impact velocities, impact angles and viscosities, in order to investigate the potential of this model in the numerical prediction of droplet deformation and evolvement under various conditions. The qualitative results for the droplet spreading process are compared to the corresponding experiments from the available literature. Also, the quantitative analysis is conducted by comparing the droplet spreading factor and spreading length.

### **Chapter 4**

This chapter focuses on the improvement and further investigation for the Hoffman-function-based DCA model. The evaluation method of the contact line velocity in the AR-DCA model is modified for the DCA calculation and an i-AR-DCA model is proposed. To investigate the effects of the improved strategy for contact line velocity treatment, the simulations of droplet impact on inclined surface and liquid water behavior in a microchannel are conducted based on AR-DCA and i-AR-DCA model.

### **Chapter 5**

The liquid water behavior and flow regimes in a single straight microchannel are studied using the VOF method and i-AR-DCA model. On one hand, the simulation is performed under a range of water injection rates with fixed air inlet velocity, in order to investigate the water inlet flow rate effects on the flow regime; on the other hand, the simulation is conducted with different air inlet velocities under specific water injection rates. The flow regimes and two-phase flow patterns under these various air/water inlet flow rates will be presented and discussed.

## Chapter 6

The conclusions and main research findings of this thesis are summarized. Some recommendations for the future work are also proposed.

## References

- [1] O'hayre R, Cha SW, Prinz FB, Colella W. Fuel cell fundamentals. John Wiley & Sons; 2016 May 2.
- [2] U.S. Dept. of Energy, Hydrogen, fuel cells & infrastructure technologies program: Multi-year research, development and demonstration plan (Section 3.4: Fuel Cells), Updated May 2017.  
[https://www.energy.gov/sites/prod/files/2017/05/f34/fcto\\_myrd\\_d\\_fuel\\_cells.pdf](https://www.energy.gov/sites/prod/files/2017/05/f34/fcto_myrd_d_fuel_cells.pdf)
- [3] Wang Y, Chen KS, Mishler J, Cho SC, Adroher XC. A review of polymer electrolyte membrane fuel cells: technology, applications, and needs on fundamental research. Applied Energy. 2011 Apr 1;88(4):981-1007.
- [4] Ji M, Wei Z. A review of water management in polymer electrolyte membrane fuel cells. Energies. 2009 Nov 17;2(4):1057-106.
- [5] Ferreira RB, Falcão DS, Oliveira VB, Pinto AM. Numerical simulations of two-phase flow in proton exchange membrane fuel cells using the volume of fluid method—A review. Journal of Power Sources. 2015 Mar 1;277:329-42.
- [6] Anderson R, Zhang L, Ding Y, Blanco M, Bi X, Wilkinson DP. A critical review of two-phase flow in gas flow channels of proton exchange membrane fuel cells. Journal of Power Sources. 2010 Aug 1;195(15):4531-53.
- [7] Quan P, Zhou B, Sobiesiak A, Liu Z. Water behavior in serpentine micro-channel for proton exchange membrane fuel cell cathode. Journal of Power Sources. 2005 Dec 1;152:131-45.
- [8] Le AD, Zhou B. A general model of proton exchange membrane fuel cell. Journal of Power Sources. 2008 Jul 15;182(1):197-222.

- [9] Le AD, Zhou B, Shiu HR, Lee CI, Chang WC. Numerical simulation and experimental validation of liquid water behaviors in a proton exchange membrane fuel cell cathode with serpentine channels. *Journal of Power Sources*. 2010 Nov 1;195(21):7302-15.
- [10] Wang X, Zhou B. Liquid water flooding process in proton exchange membrane fuel cell cathode with straight parallel channels and porous layer. *Journal of Power Sources*. 2011 Feb 15;196(4):1776-94.
- [11] Kang S, Zhou B, Cheng CH, Shiu HR, Lee CI. Liquid water flooding in a proton exchange membrane fuel cell cathode with an interdigitated design. *International Journal of Energy Research*. 2011 Dec 1;35(15):1292-311.
- [12] Kang S, Zhou B. Numerical study of bubble generation and transport in a serpentine channel with a T-junction. *International Journal of Hydrogen Energy*. 2014 Feb 4;39(5):2325-33.
- [13] Kang S, Zhou B, Jiang M. Bubble behaviors in direct methanol fuel cell anode with parallel design. *International Journal of Hydrogen Energy*. 2017 Aug 3;42(31):20201-15.
- [14] Qin Y, Du Q, Yin Y, Jiao K, Li X. Numerical investigation of water dynamics in a novel proton exchange membrane fuel cell flow channel. *Journal of Power Sources*. 2013 Jan 15;222:150-60.
- [15] Ferreira RB, Falcão DS, Oliveira VB, Pinto AM. Numerical simulations of two-phase flow in an anode gas channel of a proton exchange membrane fuel cell. *Energy*. 2015 Mar 15;82:619-28.
- [16] Ferreira RB, Falcão DS, Oliveira VB, Pinto AM. 1D+ 3D two-phase flow numerical model of a proton exchange membrane fuel cell. *Applied Energy*. 2017 Oct 1;203:474-95.
- [17] Niu Z, Jiao K, Zhang F, Du Q, Yin Y. Direct numerical simulation of two-phase turbulent flow in fuel cell flow channel. *International Journal of Hydrogen Energy*. 2016 Jan 30;41(4):3147-52.

- [18]Niu Z, Wang R, Jiao K, Du Q, Yin Y. Direct numerical simulation of low Reynolds number turbulent air-water transport in fuel cell flow channel. *Science Bulletin*. 2017 Jan 15;62(1):31-9.
- [19]Young T. An essay on the cohesion of fluids. *Philosophical Transactions of the Royal Society of London*. 1805 Jan 1;95:65-87.
- [20]Fermi, Enrico. (1936). *Thermodynamics*. Dover Publications. Online version available at:  
<http://app.knovel.com/hotlink/toc/id:kpT0000001/thermodynamics/thermodynamics>
- [21]Lunkad SF, Buwa VV, Nigam KD. Numerical simulations of drop impact and spreading on horizontal and inclined surfaces. *Chemical Engineering Science*. 2007 Dec 31;62(24):7214-24.
- [22]Legendre D, Maglio M. Numerical simulation of spreading drops. *Colloids and Surfaces A: Physicochemical and Engineering Aspects*. 2013 Sep 5;432:29-37.
- [23]Margarinos I, Nikolopoulos N, Marengo M, Antonini C, Gavaises M. VOF simulations of the contact angle dynamics during the drop spreading: standard models and a new wetting force model. *Advances in Colloid and Interface Science*. 2014 Oct 31;212:1-20.
- [24]Fang C, Hidrovo C, Wang FM, Eaton J, Goodson K. 3-D numerical simulation of contact angle hysteresis for microscale two phase flow. *International Journal of Multiphase Flow*. 2008 Jul 31;34(7):690-705.
- [25]Qin Y, Li X, Yin Y. Modeling of liquid water transport in a proton exchange membrane fuel cell gas flow channel with dynamic wettability. *International Journal of Energy Research*. 2018.
- [26]Šikalo Š, Wilhelm HD, Roisman IV, Jakirlić S, Tropea C. Dynamic contact angle of spreading droplets: Experiments and simulations. *Physics of Fluids*. 2005 Jun;17(6):062103.
- [27]Mukherjee S, Abraham J. Investigations of drop impact on dry walls with a lattice-Boltzmann model. *Journal of Colloid and Interface Science*. 2007 Aug 15;312(2):341-54.

- [28] Miller C. Liquid water dynamics in a model polymer electrolyte fuel cell flow channel, MSc Thesis, University of Victoria, 2009.
- [29] Wu TC. Two-phase flow in microchannels with application to PEM fuel cells, PhD Dissertation, University of Victoria, 2015.
- [30] Roisman IV, Opfer L, Tropea C, Raessi M, Mostaghimi J, Chandra S. Drop impact onto a dry surface: Role of the dynamic contact angle. *Colloids and Surfaces A: Physicochemical and Engineering Aspects*. 2008 Jun 5;322(1):183-91.
- [31] Wang X. Gas-liquid phenomena with dynamic contact angle in cathode of proton exchange membrane fuel cells, MSc Thesis, University of Windsor, 2011.

## CHAPTER 2

### COMPARISONS AND VALIDATIONS OF CONTACT ANGLE MODELS

#### 2.1. Introduction

Liquid water management is still one of the most challenging issues for the commercialization of proton exchange membrane fuel cells (PEMFCs). Numerical modeling and simulation can effectively predict liquid water behaviors in gas channels, which provide viable approaches to the investigation of two-phase flow in PEMFCs. Contact angle, as a crucial parameter in the boundary conditions for numerical simulation, has significant effects on droplet deformation and evolvment. However, from available literature, it is known that the static contact angle (SCA) is usually considered in PEMFC modelling (e.g., the previous works conducted by Zhou et al. [1-6], Zhu et al. [7, 8], Qin et al. [9, 10], Ding et al. [11-13], Niu et al. [14, 15], etc.), and the dynamic contact angle (DCA) model has not been reported for PEMFC simulations mainly because of the complex flow field design.

In order to apply DCA in PEMFC simulations, first, it is very important to thoroughly understand the fundamentals of DCA and its correlations.

##### 2.1.1. Dynamic Contact Angle Formulation – Hoffman function

Richard L. Hoffman is one of the pioneers in the experimental investigation of the advancing dynamic contact angle (A-DCA) [16]. Hoffman conducted a systematic study in flow regime where the viscous and interfacial forces play a dominant role on the interface shape. He built up a meniscus type of apparatus to obtain the advancing liquid-air interface with varying interface velocity through a glass capillary tube, and the liquid



moves over a solid surface and displaces a gas. A microscope was utilized to view the interface and capture the images. The interface velocity was evaluated from the plunger velocity with a correction factor which is required due to the backflow of the liquid into the space between the plunger and the glass tube. The experimental data was obtained from five different liquid systems and the capillary number  $Ca$  was ranged from approximately  $4 \times 10^{-5}$  to 35.4 ( $Ca = \mu V_i / \gamma$ , where  $\mu$  is the dynamic viscosity of the liquid,  $V_i$  is the interface velocity and  $\gamma$  is the surface tension of gas-liquid interface). By plotting the data from these experiments, Hoffman noticed, for the first time, that the apparent contact angle (essentially the advancing contact angle)  $\theta_a$  can be determined as a function of  $Ca + F(\theta_s)$ , where  $F(\theta_s)$  is defined as the shift factor, which is dependent only on the static contact angle  $\theta_s$ .

However, Hoffman did not provide a formula for the correlation between the dynamic contact angle and the sum of  $Ca$  and shift factor. In 1993, Kistler [17] proposed the so-called Hoffman function, also known as Kistler's law, as follows:

$$f_{Hoff}(x) = \arccos \left\{ 1 - 2 \tanh \left[ 5.16 \left( \frac{x}{1 + 1.31x^{0.99}} \right)^{0.706} \right] \right\} \quad (2.1)$$

and the dynamic contact angle  $\theta_d$  can be described by using the following formula:

$$\theta_d = f_{Hoff} [Ca + f_{Hoff}^{-1}(\theta_s)] \quad (2.2)$$

where the shift factor,  $f_{Hoff}^{-1}(\theta_s)$ , is obtained from the inverse of the Hoffman function when the DCA is reduced to the SCA.

### 2.1.2. Numerical Studies on Dynamic Contact Angle

In the last decade, several researchers have made efforts in DCA simulations using Hoffman function. Sikalo et al. [18] numerically studied the droplet impact on horizontal surfaces. Hoffman function was used in the simulation for both spreading process ( $Ca > 0$ ) and receding process ( $Ca < 0$ ). The numerical results were compared with the corresponding experimental results and it was concluded that using fixed contact angle as one of the boundary conditions is not sufficient and it has obvious limitations in the prediction of receding phase. Mukherjee et al. [19] conducted 2-D axisymmetric simulation to investigate droplet impact on dry walls using lattice Boltzmann method. Hoffman function was employed in this work to calculate DCAs at either advancing or receding phase. In Mukherjee's work [19], the receding contact angle was evaluated by directly reversing the advancing contact angle from the equilibrium contact angle. The numerical results showed a good consistency with the experiments for the evolution of spreading factor and contact angle. Miller [20] and Wu [21] developed DCA model implemented with Hoffman function to investigate the dynamics of two-phase flow. The authors directly followed the theory of the Hoffman's experiments [16] by considering only the advancing dynamic contact angles in the simulation. It was concluded that the dynamic contact line treatment is critical in the numerical simulation of two-phase flow. Roisman et al. [22] proposed a new mathematic function to estimate the contact line velocity, and Hoffman function was used to calculate the dynamic contact angle  $\theta_d$ . A two-phase flow model (2-D axisymmetric) implemented with this methodology was employed to predict the droplet spreading diameter, drop impacting shape and the

apparent contact angle. The results showed that these parameters are in good agreement with the experiment.

From these previous works, it is known that the Hoffman function has been applied in the numerical simulations for DCA and recognized as one of the popular formulae for DCA research. However, the fundamental understanding on the Hoffman function and a proper methodology to implement it in DCA simulations still need to be established.

In addition to Hoffman function, some other contact angle formulae and models have also been used in the numerical studies of dynamic wetting behaviors. Bussmann et al. [23] proposed a model coupled with VOF-based code and volume tracking algorithm to study the droplet impact and deformation on the inclined surface and sharp edge. Two different methods were used to predict contact angles: using measured contact angles at the leading and trailing edges from the experiment; modeling contact angle as a function of contact line velocity. The numerical results from both scenarios showed excellent agreement with the experiments in the droplet shape and spreading factor. However, the authors claimed that a more accurate model for the simulation of contact angle versus contact line velocity needs to be developed, in order to predict the droplet impact under significant inertial or viscous effects. Lunkad et al. [24] numerically simulated the droplet behaviors on both horizontal and inclined surfaces by VOF method, using the SCA and DCA models. The numerical results are compared to the corresponding experiments from Sikalo et al. [25, 26]. It was indicated that both SCA and DCA models are applicable for less wettable ( $\text{SCA} > 90^\circ$ ) horizontal surface. However, when the surface is more wettable ( $\text{SCA} < 90^\circ$ ), only DCA model is able to predict the droplet impact and

spreading. Fang et al. [27] simulated the liquid-gas microscale flows by a contact angle hysteresis model using VOF method. The Hoffman-Jiang correlation [28] and Hoffman-Tan law [29] were used to simulate the advancing contact angle and receding contact angle respectively. The results indicated that the contact angle distribution can affect the slug elongation and instability in the microchannel. Legendre et al. [30] investigated the effects of different parameters (including liquid viscosity, surface tension, liquid density, droplet radius and static contact angle  $\theta_s$ ) on the droplet spreading on a horizontal surface, and the dynamic contact angle is modeled by Cox's correlation [31]. The simulation results showed that  $\theta_s$  and viscosity can significantly affect the spreading phenomena of droplets. Malgarinos et al. [32] presented a novel wetting force model based on VOF method in which an additional force term was considered in the momentum equation of the mathematical modeling, and the dynamic contact angle is directly obtained from the interface shape and adhesion force instead of being considered as a boundary condition. The numerical results fit well with the experimental data, as well as three different dynamic contact angle models (i.e., the simple advancing-receding model [32], DCA model based on Hoffman function [17], and DCA model by Shikhmurzaev [33]). It was suggested that this model can effectively predict the droplet spreading under low and moderate Weber number ( $We = \rho V_p^2 D / \gamma$ , where  $\rho$  is the droplet density,  $V_p$  is the impact velocity,  $D$  is the droplet initial diameter).

### 2.1.3. Summary

From the literature review, it is known that over the last decades, a series of numerical studies were conducted to investigate the contact angle effects on dynamic wetting behaviors, and it is found that DCA model is more applicable than SCA model in the

corresponding numerical simulations. The correlations used in DCA simulations from available literature are summarized in Table 2.1 and it can be found that Hoffman function is one of the promising formulae for researchers to conduct DCA simulations.

**Table 2.1: Correlations Used in DCA Simulations from Available Literature**

Authors and published year	Numerical model	Contact angle model/correlations
Bussmann et al. [23] (1999)	3-D model, Eulerian fixed-grid algorithm and VOF-based code	a) Measured contact angles at the leading and trailing edge; b) A simpler model: $\theta_d = \theta_d(V_{cl})$
Sikalo et al. [18] (2005)	2-D axisymmetric model, VOF based free-surface capturing method	Hoffman function (spreading process: $Ca > 0$ ; receding process: $Ca < 0$ )
Mukherjee et al. [19] (2007)	2-D axisymmetric model, lattice Boltzmann method	Hoffman function
Roisman et al. [22] (2008)	2-D axisymmetric model, VOF method	Hoffman function
Fang et al. [27] (2008)	3-D model, VOF method	$\theta_a$ : Hoffman-Jiang correlation [28] $\theta_r$ : Hoffman-Tan law [29]
Miller [20] (2009)	2-D axisymmetric and 3-D model, VOF method	Hoffman function
Legendre et al. [30] (2013)	2-D axisymmetric model, VOF method	Cox's correlation [31]
Malgarinos et al. [32] (2014)	Wetting force model and VOF method	a) Simple advancing-receding model b) Hoffman function c) Shikhmurzaev's model [33]

In this Chapter, a DCA evolution map is created to clarify the fundamental understanding of Hoffman function and illustrate the DCA evolving mechanism; based on this evolution map, the Advancing-Receding DCA (AR-DCA) model is proposed and explained, in addition to the Advancing DCA (A-DCA) model directly correlated from the original

Hoffman's experiments. Using User Defined Function (UDF), the Hoffman function is implemented into A-DCA and AR-DCA models. Then, with VOF method, a series of simulations for droplet (water and glycerin) impact on horizontal and inclined surfaces are conducted based on the A-DCA, AR-DCA and SCA models. The numerical results from these three models are compared qualitatively and quantitatively to the corresponding experimental results from Sikalo et al [25, 34].

## 2.2. Fundamental Understanding of Hoffman Function

From Hoffman's original experiments [16], it is known that the advancing liquid-air interface was captured to investigate the relation between the advancing contact angle and capillary number. Thus, the A-DCA model is developed by following the basic understanding of Hoffman function, and the Equation (2.2) is utilized to predict the advancing contact angle. For  $Ca > 0$ ,  $Ca + f_{Hoff}^{-1}(\theta_s) > f_{Hoff}^{-1}(\theta_s)$ , then the value of  $\theta_d$  ( $\theta_d = f_{Hoff}[Ca + f_{Hoff}^{-1}(\theta_s)]$ ) will be always greater than that of the static contact angle  $\theta_s$ , which refers to the advancing phase. In the previous research work by Miller [20], the 2-D axisymmetric simulation of water droplet impact on horizontal surface was conducted with DCA model, which considered only the advancing dynamic contact angles: the capillary number in the UDF code of Ref. [20] was assumed to be always positive while the advancing dynamic contact angle was calculated.

In addition to A-DCA model, another method to employ Hoffman function is to consider both advancing and receding contact angles, defined as AR-DCA model in this thesis. Figure 2.1 shows a dynamic contact angle evolution map which is used to better illustrate the advancing and receding process using Hoffman function (the data is extracted from

Hoffman's experiments [16]). We assume a point  $p$  on the curve where the liquid system reaches the equilibrium state and the contact angle at this moment will be the static contact angle  $\theta_s$ . The  $x$ -coordinate of point  $p$ ,  $x_p$ , is the shift factor of this liquid system, because when the contact line velocity  $V_{cl} = 0$ ,  $x_p = \mu V_{cl}/\gamma + f_{Hoff}^{-1}(\theta_s) = f_{Hoff}^{-1}(\theta_s)$ . When  $V_{cl} > 0$ ,  $\mu V_{cl}/\gamma + f_{Hoff}^{-1}(\theta_s) > x_p$ ,  $\theta_d = f_{Hoff}[\mu V_{cl}/\gamma + f_{Hoff}^{-1}(\theta_s)] > \theta_s$ , which refers to the advancing phase (on the right side of point  $p$  along the curve as shown in Figure 2.1; when  $V_{cl} < 0$ ,  $\mu V_{cl}/\gamma + f_{Hoff}^{-1}(\theta_s) < x_p$ ,  $\theta_d = f_{Hoff}[\mu V_{cl}/\gamma + f_{Hoff}^{-1}(\theta_s)] < \theta_s$ , which refers to the receding phase (on the left side of point  $p$  along the curve as shown in Figure 2.1.

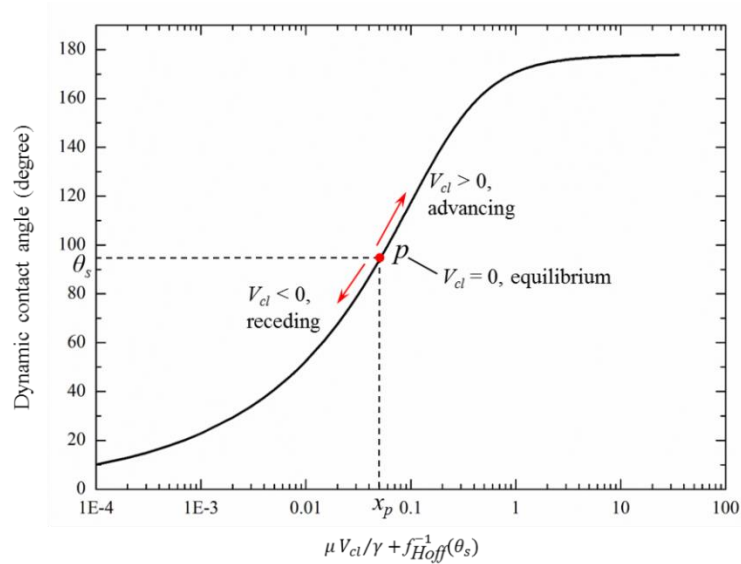


Figure 2.1: Dynamic contact angle evolution map.

### 2.3. Numerical Methodology

In this study, by creating a UDF code in ANSYS Fluent, the A-DCA and AR-DCA models are developed with the implementation of DCA at the wall boundary. The VOF method is used to track the liquid-gas flow interface.

### 2.3.1. Governing Equations with Volume of Fluid (VOF) Method

The mass conservation equation is expressed as:

$$\frac{\partial(\rho)}{\partial t} + \nabla \cdot (\rho \vec{u}) = 0 \quad (2.3)$$

In the VOF model, the gas and liquid phases can be considered as a two-phase mixture flow. The mixture density and viscosity can be calculated by:

$$\rho = s_l \rho_l + s_g \rho_g \quad (2.4)$$

$$\mu = s_l \mu_l + s_g \mu_g \quad (2.5)$$

where  $s_l$  is the volume fraction of liquid phase and  $s_g$  is the volume fraction of gas phase.

The sum of the volume fraction is:

$$s_l + s_g = 1 \quad (2.6)$$

The interface between the gas and liquid phase is tracked by solving the continuity equation for the volume fraction of one of the phases, e.g., for liquid phase:

$$\frac{\partial(s_l \rho_l)}{\partial t} + \nabla \cdot (s_l \rho_l \vec{u}) = 0 \quad (2.7)$$

A single momentum equation is given by:

$$\frac{\partial}{\partial t}(\rho \vec{u}) + \nabla \cdot (\rho \vec{u} \vec{u}) = -\nabla p + \nabla \cdot [\mu(\nabla \vec{u} + \nabla \vec{u}^T)] + S_m \quad (2.8)$$

The momentum source term  $S_m$ , which includes the surface tension and gravity force, can



be expressed as:

$$S_m = \rho g + \gamma \kappa \frac{\rho \nabla s_l}{(\rho_l + \rho_g)/2} \quad (2.9)$$

where  $\gamma$  is the surface tension coefficient and  $\kappa$  is the surface curvature.

For the numerical simulation for droplet impact on horizontal and inclined surface in this study, the time step is set as  $1 \times 10^{-6}$  s for all the cases to keep the Courant number ( $Co$ ) less than 0.5, in order to ensure the calculation stability.

### 2.3.2. Implementation of Contact Angle Models

Using ANSYS Fluent, the SCA model is employed with the input static contact angle  $\theta_s$  at the wall boundaries. The surface unit normal  $\hat{n}$  is determined by:

$$\hat{n} = \hat{n}_w \cos \theta_s + \hat{t}_w \sin \theta_s \quad (2.10)$$

where  $\hat{n}_w$  and  $\hat{t}_w$  refer to the unit vectors normal and tangential to the wall respectively.

In A-DCA and AR-DCA models, Equation (2.11) is used instead of Equation (2.10):

$$\hat{n} = \hat{n}_w \cos \theta_d + \hat{t}_w \sin \theta_d \quad (2.11)$$

$\theta_d$  is the dynamic contact angle applied at the wall boundaries through a UDF code based on the Hoffman function, i.e., Equation (2.1) and (2.2).

In order to implement the DCA models, the authors have used the original UDF code from Ref. [20] to try a few simple tests and found that it did not work properly for our cases. The UDF code in Ref. [20] has its own limitations, e.g., it artificially sets the

capillary number  $Ca$  to be the absolute value of  $\mu V_{cl}/\gamma$ , i.e.,  $Ca = \mu|V_{cl}|/\gamma$ . Therefore, for the results reported in this Chapter, we build our own UDF code to implement both A-DCA and AR-DCA models, based on the experience we learned through testing the original UDF code in Ref. [20].

## 2.4. Numerical Model Description

### 2.4.1. Experiments for Validation

Sikalo et al. [25, 34] conducted a series of experiments for droplet impact on horizontal and inclined surfaces, and investigated the droplet dynamic behaviors and phenomena. A schematic diagram for the droplet impact on the inclined surface in the experiment is shown in Figure 2.2: the droplet falls down vertically with an angle  $\alpha$  between the falling direction and the surface. In the case of the horizontal surface, the angle  $\alpha$  becomes  $90^\circ$ .

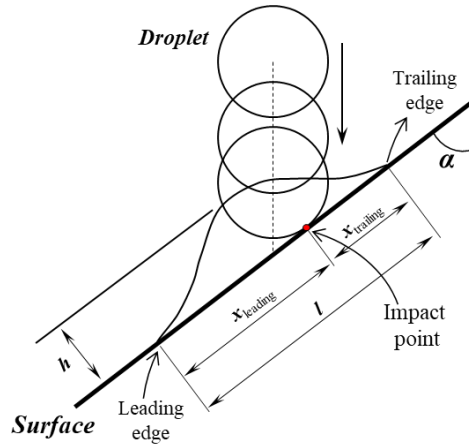


Figure 2.2: Schematic of droplet impact on a surface [25].

In the present study, four cases are selected and simulated: 1) glycerin droplet impact on horizontal smooth glass [34]. 2) water droplet impact on smooth glass ( $\alpha = 45^\circ$ ) [34]; 3) water droplet impact on smooth glass ( $\alpha = 10^\circ$ ) [25]; 4) water droplet impact on wax ( $\alpha = 10^\circ$ ) [25]; The detailed liquid property, surface wettability and impact velocity are given

in Table 2.2.

**Table 2.2: Detailed Liquid Property, Surface Wettability and Impact Velocity for Selected Cases**

Case #	Liquid	Initial droplet diameter $D$ (mm)	Impact angle $\alpha$ (°)	Surface tension $\gamma$ (N/m)	Viscosity $\mu$ (mPa s)	Density $\rho$ (kg/m <sup>3</sup> )	$\theta_a - \theta_r$ (°)	Weber number ( $We$ )	Impact velocity $V_p$ (m/s)
1	Glycerin	2.45	90	0.063	116	1220	17-13	391	2.871
2	Water	2.7	45	0.073	1.0	996	10-6	391	3.253
3	Water	2.7	10	0.073	1.0	996	10-6	391	3.253
4	Water	2.7	10	0.073	1.0	996	105-95	391	3.253

#### 2.4.2. Computational Domain and Input Parameters

For the numerical simulation, a three-dimensional cylinder computational domain is employed in the present study, as shown in Figure 2.3(a), with the radius ( $R$ ) of 7.5 mm and height ( $H$ ) of 4 mm. The direction of gravity is set along the negative Y-axis. The mesh type is triangular wedge and a refinement of the mesh near the bottom wall is conducted in order to better simulate the droplet interface near the boundary wall. The no-slip boundary condition is applied on the bottom wall. The pressure-inlet boundary is implemented on the remaining surfaces to represent the surrounding atmosphere with gauge total pressure set as zero. Figure 2.3(b) is a schematic of the droplet initial and impact positions in the computational domain. In the beginning of the numerical simulation, the droplet is patched in the domain with an initial velocity  $V_0$  (negative Y-axis direction) and falling distance  $d_0$  in order to achieve the impact velocity  $V_p$  in the corresponding experiment. The input SCA in the simulation for the shift factor  $f_{Hoff}^{-1}(\theta_s)$  is determined by the equilibrium value between  $\theta_a$  and  $\theta_r$ . The detailed input parameters for each case are shown in Table 2.3.

First, in order to ensure the computational domain is sufficiently reliable for the simulation, the effect of domain size on the simulation results is tested based on the current domain ( $R = 7.5$  mm and  $H = 4$  mm) and another domain with larger radius ( $R = 9$  mm and  $H = 4$  mm). Figure 2.4(a) and (b) show the comparison of the ratio  $l/h$  (droplet spreading length/droplet apex height) in terms of a dimensionless time  $t^*$  ( $t^* = t V_p/D$  [25], where  $t$  is the time from impact) based on these two domains for Case 1 and Case 2 respectively and the results are nearly identical, indicating that the increase of domain size has no significant effects on the simulation for droplet deformation.

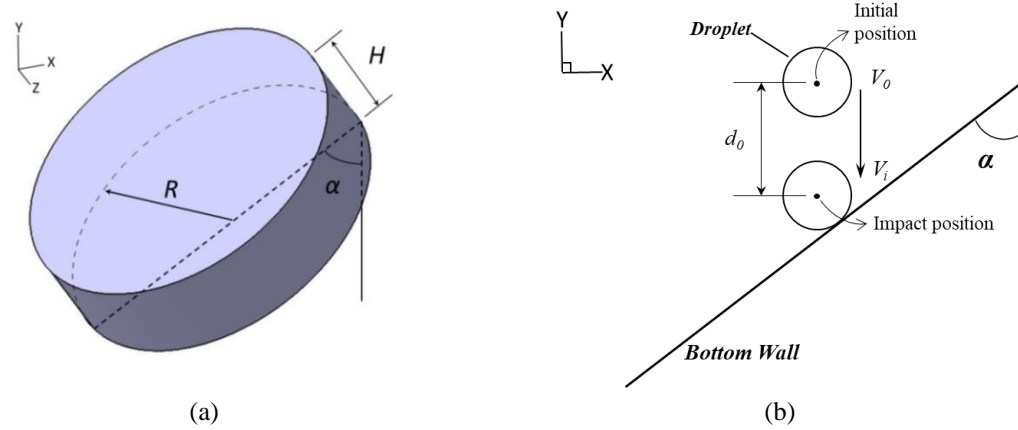


Figure 2.3: (a) Schematic of computational domain used in the numerical simulation; (b) Schematic of the droplet initial and impact position in the computational domain (side-view).

**Table 2.3: Simulation Parameters for Selected Cases**

Case #	Droplet initial velocity $V_0$ (m/s)	Falling distance $d_0$ (mm)	Impact time $t_i$ (ms)	Droplet Impact velocity $V_p$ (m/s)	Input SCA ( $^\circ$ )
1	2.867	1.225	0.42	2.871	15
2	3.250	1.100	0.33	3.253	8
3	3.250	1.100	0.33	3.253	8
4	3.250	1.100	0.33	3.253	100

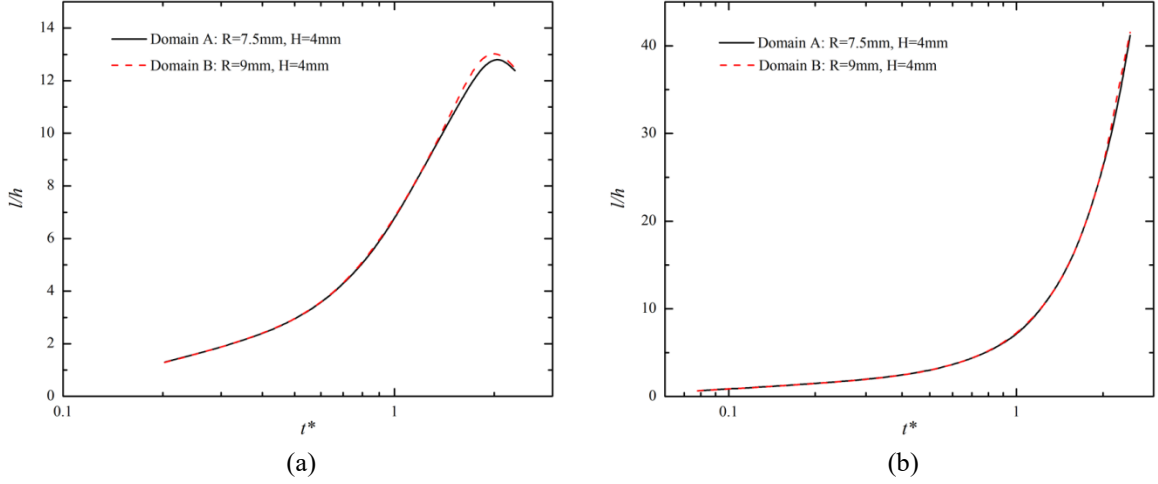


Figure 2.4: Effects of computational domain size on the numerical results: (a) Case 1; (b) Case 2.

### 2.4.3. Mesh Independency

In the present study, the mesh independency is performed by applying different number of nodes along the side edge (i.e., the direction along the height ( $H = 4\text{ mm}$ )) and the bottom edge. The information of different grid resolutions is shown in Table 2.4.

**Table 2.4: Information of Different Grid Resolutions in the Present Study**

Grid Resolution Type	Number of nodes along the height (H)	Number of nodes along the bottom edge	Total number of nodes (approximately)	Maximum cell volume ( $\text{mm}^3$ )	Minimum cell volume ( $\text{mm}^3$ )
A	21	235	108,000	$6.09 \times 10^{-3}$	$1.34 \times 10^{-3}$
B	41	471	835,000	$9.24 \times 10^{-4}$	$1.43 \times 10^{-4}$
C	68	589	2,160,000	$4.83 \times 10^{-4}$	$3.69 \times 10^{-5}$
D	81	673	3,345,000	$3.16 \times 10^{-4}$	$1.98 \times 10^{-5}$

Figure 2.5 and Figure 2.6 show the numerical results under different grid resolutions (under Case 1 and 2) for both qualitative and quantitative comparisons. It can be noted that for the glycerin droplet impact on horizontal surface (Case 1), the droplet profile becomes smoother from Resolution A to B, and the droplet deformation from Resolution

B, C and D is quite similar, as shown in Figure 2.5(a). However, from Figure 2.5(b), it can be seen that the evolutions of  $l/h$  versus  $t^*$  from all the grid resolution types are close before approximately  $t^* = 1.6$ ; after that, the values of  $l/h$  from Resolution C and D (finer grid) have a sudden drop at about  $t^* = 2.0$ , which is not reflected in coarser grids (Resolution A and B). For the water droplet impact on  $45^\circ$  inclined surface (Case 2), an obvious improvement on the simulation quality can be observed from Resolution A and B to Resolution C and D, as shown in Figure 2.6(a): under coarse grid (Resolution A), the droplet forms liquid slug when it slides along the surface while under Resolution B, C and D, the droplet can fully spread on the surface and form liquid film; also, for the last profile (2.0 ms), the leading edge of the liquid film breaks up into small parts under Resolution B whereas the finer grid (Resolution C and D) can generate smooth rim and the major features are identical. The quantitative comparison for Case 2 (Figure 2.6(b)) also shows that the Resolution A results in lower value of  $l/h$ . Considering the increased computational cost with the increase of the number of nodes, the grid resolution type C is adopted for all the four cases in the present study.

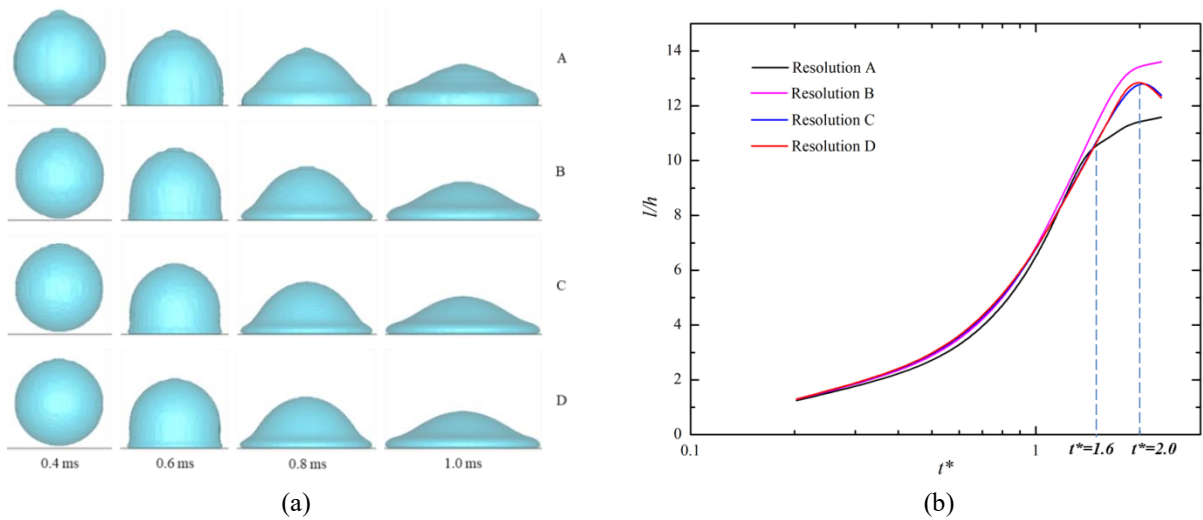


Figure 2.5: Numerical results of Case 1 under different grid resolution: (a) grid resolution type A; (b) grid resolution type B; (c) grid resolution type C; (d) grid resolution type D.

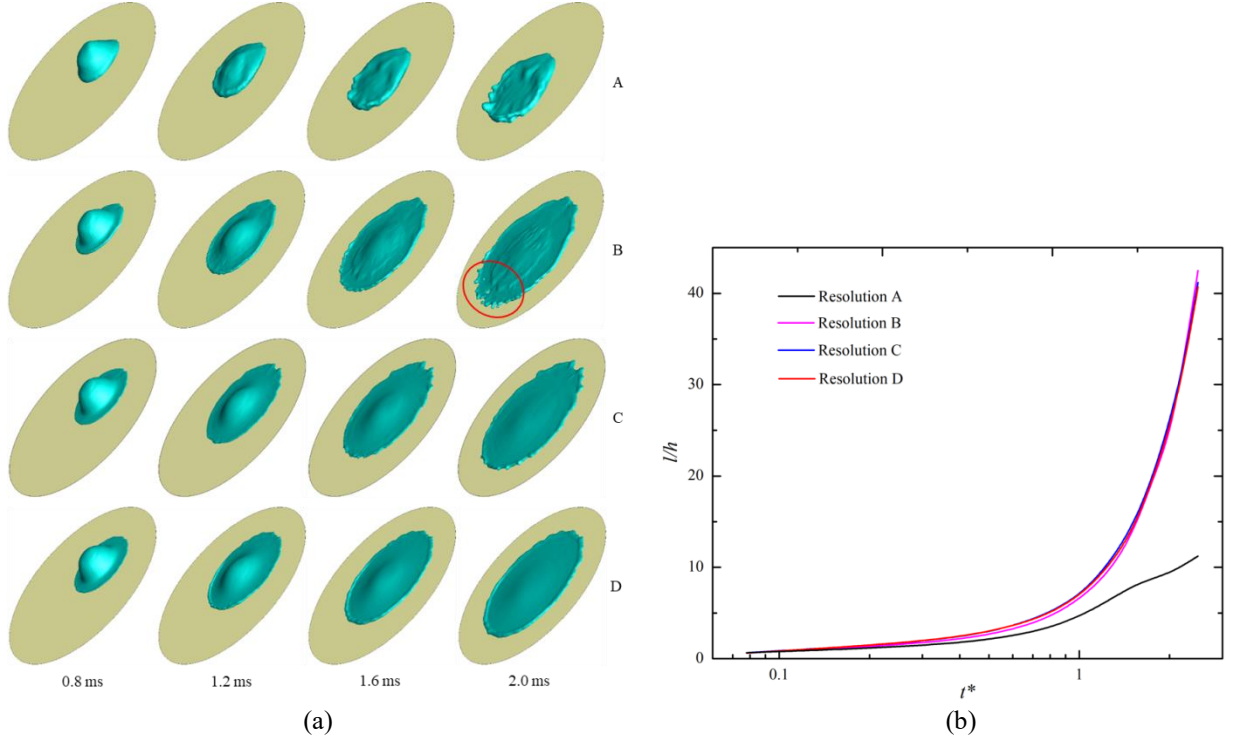


Figure 2.6: Numerical results of Case 2 under different grid resolution: (a) grid resolution type A; (b) grid resolution type B; (c) grid resolution type C; (d) grid resolution type D.

## 2.5. Results and Discussion

In the present study, the dynamic contact angle is evaluated by Hoffman function using two different methods: 1) only advancing dynamic contact angles are considered in the simulation (A-DCA model); 2) both advancing and receding dynamic contact angles are considered (AR-DCA model). The simulations using static contact angle (SCA) model are also conducted. The numerical results from these three models for all the four selected cases are shown as follows, with the comparisons to the corresponding experiments.

### 2.5.1. Qualitative Results

#### 2.5.1.1. Comparisons of the Numerical Results for Case 1

Figure 2.7 shows the side view of the comparison of the numerical results for Case 1 from A-DCA, AR-DCA and SCA models. The time intervals of the droplet profiles from

the simulation (Figure 2.7(b), (c) and (d)) are identical to those from the experiment (Figure 2.7(a)) in Ref. [34]. The droplet impact time  $t_i$  in the simulation is 0.42 ms (as shown in Table 2.3), thus the last three profiles (0.520 ms, 0.680 ms and 2.440 ms) are corresponding to the experimental results at 0.100 ms, 0.260 ms, and 2.020 ms. Figure 2.8 shows the 3D-view of the numerical results at different time instants in the simulation. From both the side-view and 3D-view, it is noted that the numerical results from these three models are almost the same and all of them perfectly match the experimental results. This is because in Case 1, only the advancing phase is captured in the experiment (Figure 2.7(a)) for the droplet spreading process and thus the receding effect is not reflected in the simulation. Also, in the early spreading process of Case 1, because of the dominated gravitational force and higher Weber number (391) at the impact instant, the DCA effects are not significantly reflected in DCA models.

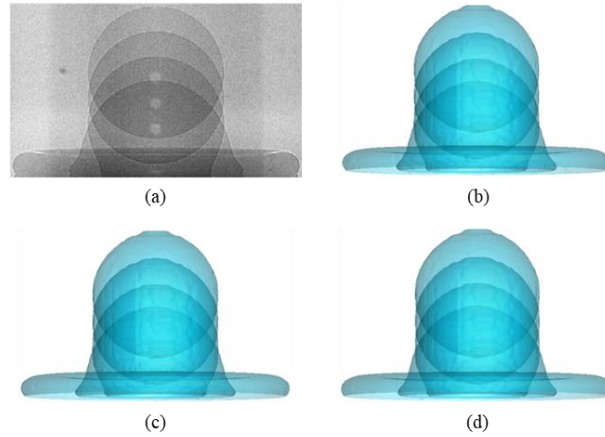


Figure 2.7: Comparison of numerical and experimental results for Case 1 (side-view). (a) Experiment at 0.100, 0.260, 2.020 ms (last three profiles) after impact [34]; (b) A-DCA model (c) AR-DCA model. (d) SCA model.



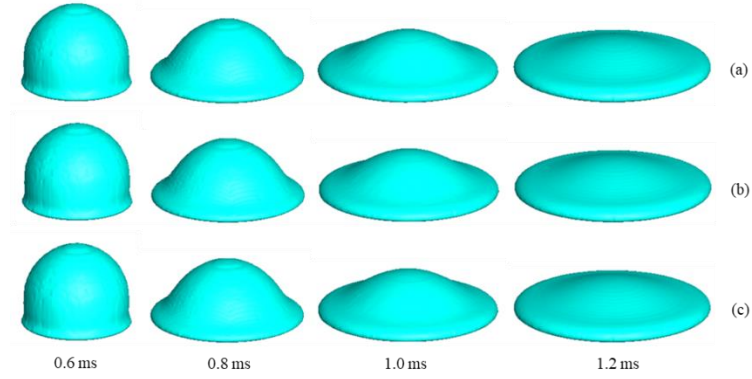


Figure 2.8: Comparison of numerical results for Case 1 (3D-view). (a) A-DCA model; (b) AR-DCA model; (c) SCA model.

### 2.5.1.2. Comparisons of the Numerical Results for Case 2

In order to further investigate the advancing and receding effects on the simulation, another three cases for droplet impingement on inclined surfaces are also simulated with these three models and the results are compared qualitatively.

Figure 2.9 and Figure 2.10 show the comparison of the numerical results from A-DCA, AR-DCA and SCA models for Case 2 by side-view and 3D-view respectively. The time instant of the droplet impact is 0.33 ms in the numerical simulation (as shown in Table 2.3), thus the droplet at 0.42 ms, 1.08 ms, and 2.45 ms are selected for the comparison, which is corresponding to the droplet at 0.09 ms, 0.75 ms and 2.12 ms respectively in the experiment (Figure 2.9(a)). From the side-view, it is noted that the simulation results from these three models for the first two droplet profiles (0.42 ms, 1.08 ms) are all very similar to the experiment. However, for the last profile (2.45 ms), when the droplet almost fully spreads onto the surface, the surface of liquid film from SCA model is smoother than that of the A-DCA and AR-DCA models.

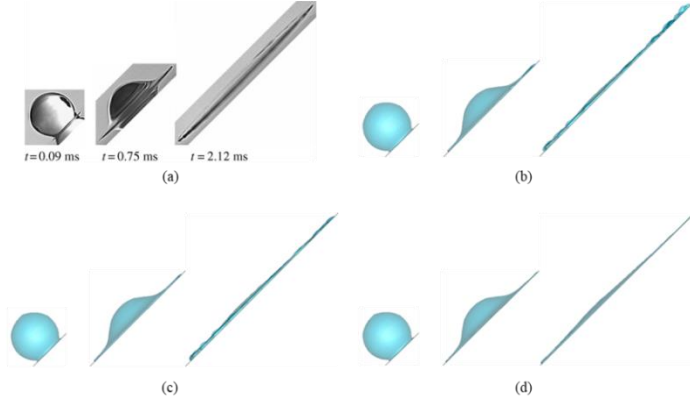


Figure 2.9: Comparison of numerical and experimental results for Case 2 (side-view). (a) Experiment [34]; (b) A-DCA model; (c) AR-DCA model; (d) SCA model.

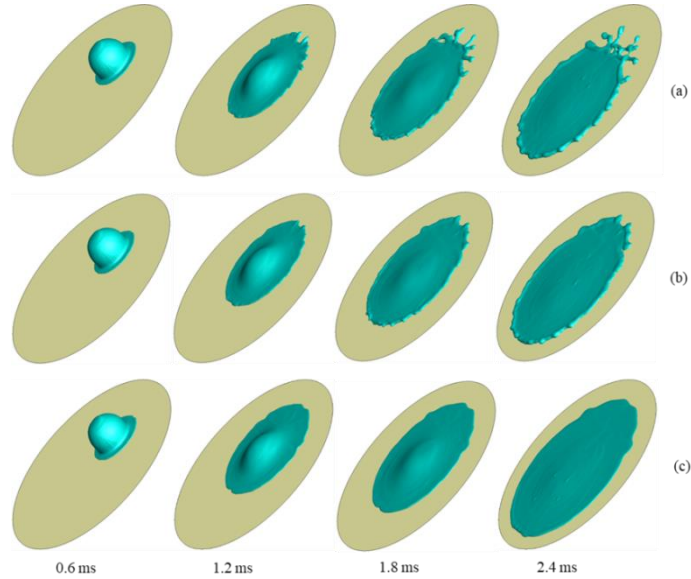


Figure 2.10: Comparison of numerical results for Case 2 (3D-view). (a) A-DCA model; (b) AR-DCA model; (c) SCA model.

From the 3D-view, the distinction of the numerical results from the three models can be observed: on one hand, for A-DCA and AR-DCA models, when the droplet spreads and moves downwards along the surface, the trailing edge of the droplet from A-DCA model starts to break into several small parts (child droplets) and tends to separate from the main part (mother droplet), as shown in Figure 2.10(a); whereas for AR-DCA model, there is some raised rim on the edge area and the droplet shape tends to vary more regularly than that from A-DCA model, as shown in Figure 2.10(b). The reason for these

two distinct phenomena is that, for A-DCA model, only the advancing phase is considered in the process and the contact line velocity is always positive, which results in higher dynamic contact angle values than that of the AR-DCA model (in AR-DCA model, receding phase is also considered and contact line velocity can be negative). Then the higher dynamic contact angles at the trailing edge will break up the droplet and facilitate the formation of child droplets. It is also observed that the droplet deformation at the leading edge area from these two models is very similar, because for the cases of droplet inclined spreading, the advancing phase is dominant at the droplet leading edge, and both A-DCA and AR-DCA models can simulate the advancing dynamic contact angles.

On the other hand, comparing the numerical results of SCA model to the two DCA models, it can be seen that the droplet from SCA model constantly spreads stably and the edge is smoother. This is because in SCA model, the contact angle is not affected by the contact line velocity and surrounding flow, which will result in a more stable process for the droplet spreading and deformation. Although only the side view of the droplet profiles from the experiment is provided as shown in Figure 2.9(a), it still can be observed that in the later spreading phase, the droplet edge is not able to remain in a smooth profile. It is indicated that for Case 2, the numerical results from AR-DCA model are closer to the experiment, especially for the last droplet profile.

#### **2.5.1.3. Comparisons of the Numerical Results for Case 3**

As shown in Figure 2.11 and Figure 2.12, comparing with the experimental results of Case 3 (Figure 2.11(a)), the numerical results from A-DCA model is not able to capture

the spreading phenomena in this case while the results from AR-DCA model have an excellent agreement with the experiment: for A-DCA model, the trailing edge of the droplet slides down with the moving of the main part because of the higher dynamic contact angles; whereas for AR-DCA model, the trailing edge of the droplet tends to be fixed on the glass surface when the main part of the droplet moves downwards, because the receding phase is considered and dynamic contact angles become smaller. In this case, the SCA value for the water on smooth glass is set as  $8^\circ$  in the simulation, which indicates the high wettability. Also, from the comparison of the numerical results based on SCA model and AR-DCA model, it can be seen that the first two droplet profiles (from top to bottom) are very similar and can match the experimental results very well. However, for the last droplet profile, only the result from AR-DCA model is similar to the experiment: the apparent contact angle observed at the front interface of the droplet from AR-DCA model is larger than that of the SCA model, as shown in Figure 2.11(c) and Figure 2.11(d). This is because in AR-DCA model the contact angle is varied from the equilibrium point with the moving of contact line, and it will further lead to the increase of apparent contact angle at the droplet front interface.

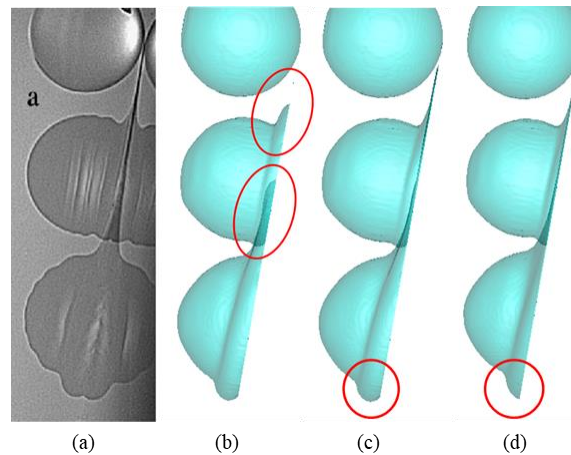


Figure 2.11: Comparison of numerical and experimental results for Case 3 (side-view) (a) Experiment [25]; (b) A-DCA model; (c) AR-DCA model; (d) SCA model.

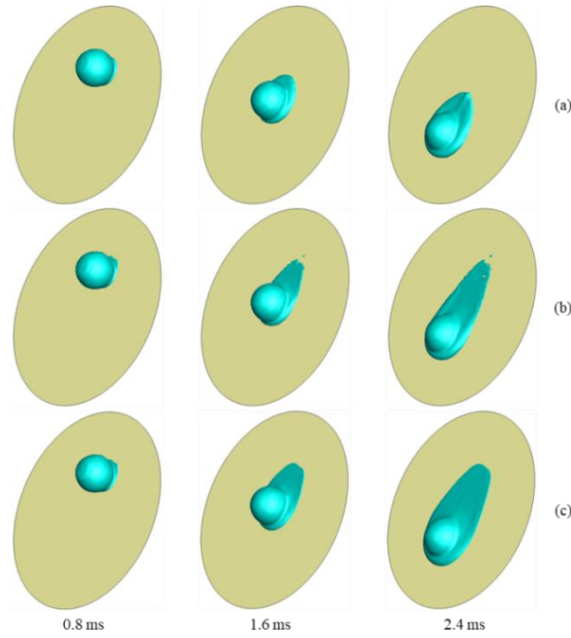


Figure 2.12: Comparison of numerical results for Case 3 (3D-view) (a) A-DCA model; (b) AR-DCA model; (c) SCA model.

#### 2.5.1.4. Comparisons of the Numerical Results for Case 4

For Case 4, from the side-view (Figure 2.13), some differences between the results from A-DCA and AR-DCA models can also be observed: the length of the trailing part of the last droplet (marked in the red circle) from AR-DCA model is longer, because in AR-DCA model, the receding effect is considered and the trailing edge tends to rebound when the droplet slides down, which is closer to the experiment. From the 3D-view of the results from A-DCA model, it can be observed that there are several sharp edges emerged on the trailing edge of the droplet at  $t = 2.4$  ms, as shown in Figure 2.14(a); whereas for AR-DCA model, at the same instant, the trailing edge of the droplet tends to converge to one sharp edge and rebound at the end of the droplet tail, as shown in Figure 2.14(b).

Also, comparing the numerical results of SCA model and AR-DCA model, it is observed that, the length of the trailing part in the last droplet profile from AR-DCA model is

longer than that of SCA model, as shown in Figure 2.13(c) and (d), and the rebound phenomenon of the droplet tail cannot be well simulated and reflected in SCA model.

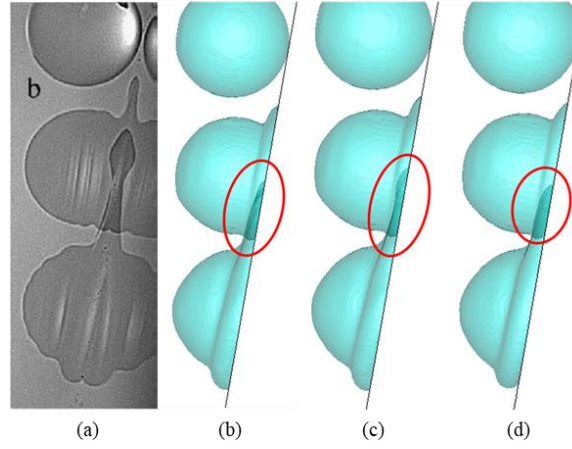


Figure 2.13: Comparison of numerical and experimental results for Case 4 (side-view) (a) Experiment [25]; (b) A-DCA model; (c) AR-DCA model; (d) SCA model.

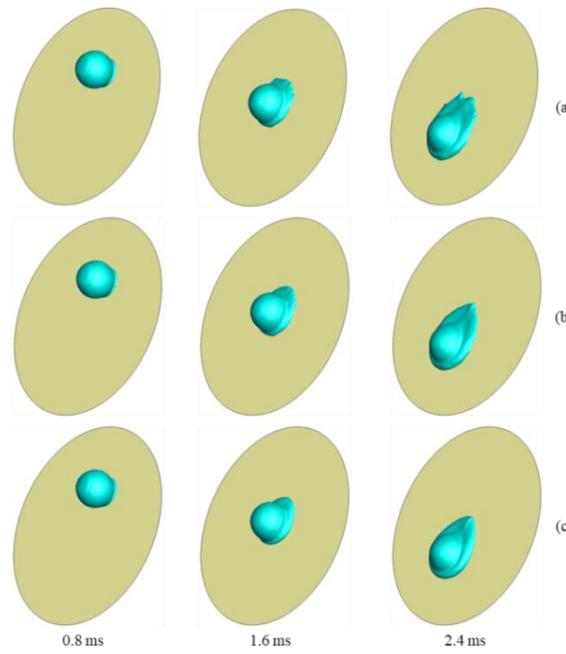


Figure 2.14: Comparison of numerical results for Case 4 (3D-view) (a) A-DCA model; (b) AR-DCA model; (c) SCA model.

In summary, from the qualitative comparisons, it can be concluded that for Case 1, the A-DCA, AR-DCA and SCA models are all able to simulate the droplet spreading phenomena after impingement on the horizontal surface. However, for the droplet impact

on inclined surfaces (Case 2, Case 3 and Case 4), only the AR-DCA model can well simulate the droplet dynamics and deformation for all the selected cases, and the numerical results have excellent agreement with the corresponding experimental results.

### 2.5.2. Quantitative Results

In order to quantitatively compare the numerical results from the A-DCA, AR-DCA and SCA models against the corresponding experimental results, the spreading factor  $x/D$  at the leading and trailing side ( $x_{\text{leading}}/D$  and  $x_{\text{trailing}}/D$ ) as a function of dimensionless time  $t^*$  after impact, are plotted and analyzed. The droplet spreading length on the surface is also evaluated and compared by using a dimensionless parameter  $l/D$  versus  $t^*$ . Meanwhile, for A-DCA and AR-DCA models, the evolution of contact angles at the leading and trailing edges ( $\theta_{\text{leading}}$  and  $\theta_{\text{trailing}}$ ) versus time  $t$  are studied by analyzing the data extracted from corresponding UDF code. The Case 2, Case 3, and Case 4 are investigated in this section to better understand and illustrate the differences of the qualitative numerical results from the three models (Case 1 is not discussed here because the numerical results of Case 1 from the three contact angle models are almost identical and the relevant quantitative experimental data is not provided in the literature).

#### 2.5.2.1. Spreading Factor and Dimensionless Spreading Length ( $l/D$ )

For Case 2 (water droplet impact on 45 °inclined smooth glass), comparing the spreading factors from A-DCA, AR-DCA, SCA models and the experiment (data extracted from Ref. [25]), it is noted that the spreading factors at the leading side  $x_{\text{leading}}/D$  from the three contact angle models have excellent agreement with those measured from the experiment, showing the capability of these models to simulate the droplet leading edge; and the

spreading factors at the trailing side  $x_{\text{trailing}}/D$  are also close to those from the experiment and have a similar evolution trend, as shown in Figure 2.15(a).

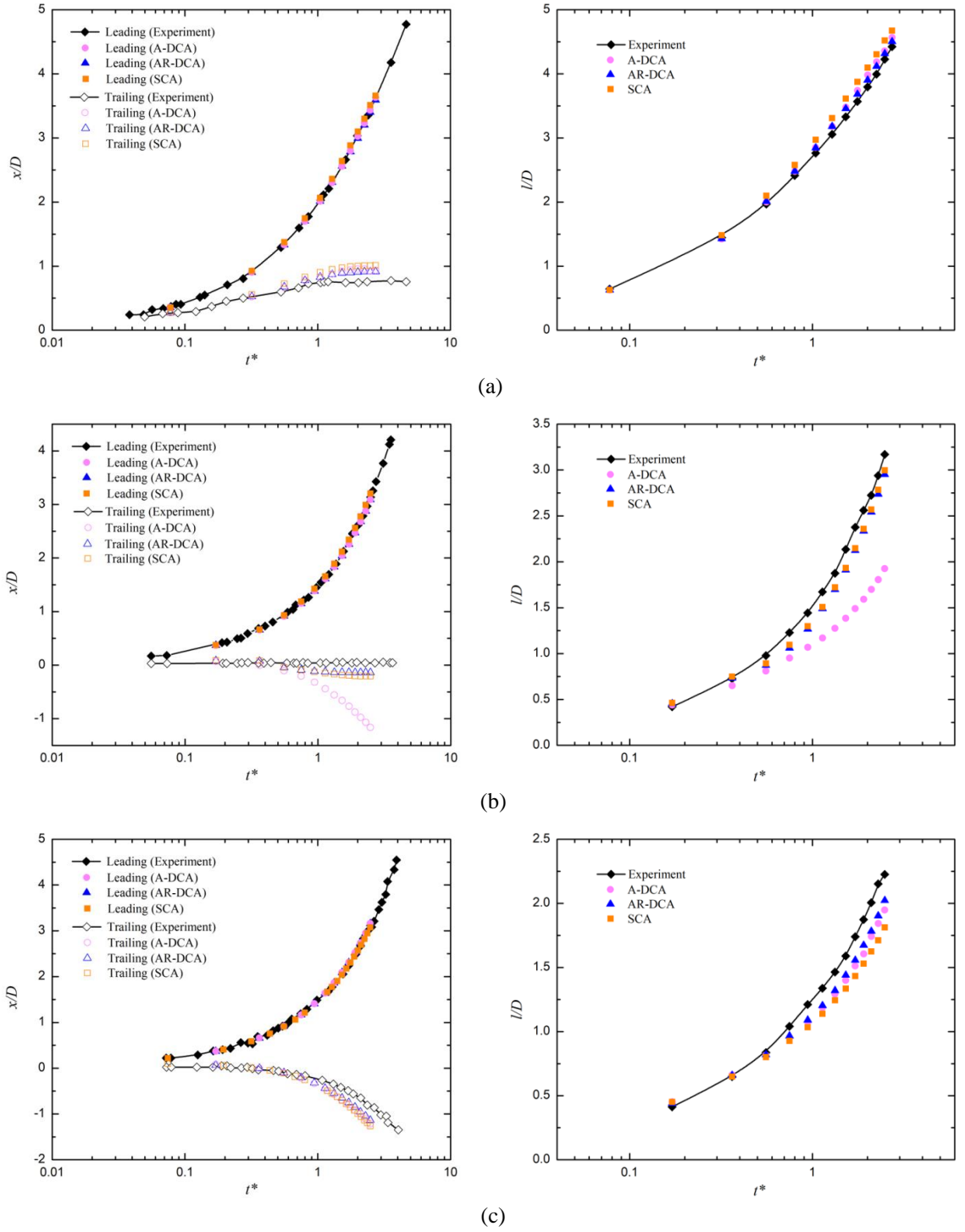


Figure 2.15: Comparisons of the spreading factor  $x/D$  (left column) and dimensionless droplet spreading length  $l/D$  (right column). (a) Case 2; (b) Case 3; (c) Case 4.



For Case 3 (water droplet impact on  $10^\circ$  inclined smooth glass),  $x_{\text{leading}}/D$  from all the three models can match the experiment very well, whereas the trend of  $x_{\text{trailing}}/D$  from A-DCA model is significantly different from the experimental result, as shown in Figure 2.15(b): the value of  $x_{\text{trailing}}/D$  from A-DCA model declines sharply from approximately  $t^* = 0.4$ , which indicates the slipping down of the droplet from the impact point (corresponding to the phenomenological observation of the numerical results in Figure 2.11(b)); and the droplet spreading length from A-DCA model is shorter than that of the AR-DCA and SCA models and the experiment, showing that the A-DCA model is not able to well simulate droplet behaviors in Case 3.

For Case 4 (water droplet impact on  $10^\circ$  inclined wax), the spreading factors from the three models are all in good agreement with the experimental results. However, the value of  $l/D$  from AR-DCA model is slightly higher than that of the A-DCA and SCA model, indicating the spreading length is closer to the experiment (corresponding to the phenomenological observation in Figure 2.13).

#### **2.5.2.2. Contact Angle at the Leading and Trailing Edges**

Figure 2.16(a)-(c) show the comparisons of contact angle values at the leading and trailing edges for A-DCA and AR-DCA models in Case 2, Case 3 and Case 4 respectively. For Case 2,  $\theta_{\text{leading}}$  from A-DCA and AR-DCA models decrease from approximately  $65^\circ$  to  $40^\circ$ , whereas a significant difference in  $\theta_{\text{trailing}}$  can be captured: although  $\theta_{\text{trailing}}$  from both of the two DCA models declines with fluctuation from about  $62^\circ$ , the  $\theta_{\text{trailing}}$  from A-DCA model is always greater than the SCA (the horizontal dashed line in the Figure 2.16(a)) while the  $\theta_{\text{trailing}}$  from AR-DCA model becomes smaller than

SCA after  $t^* = 1.28$ , which is corresponding to the qualitative simulation results in Figure 2.10 (the higher  $\theta_{\text{trailing}}$  values from A-DCA model lead to the partial break-up of the droplet at the trailing edge area).

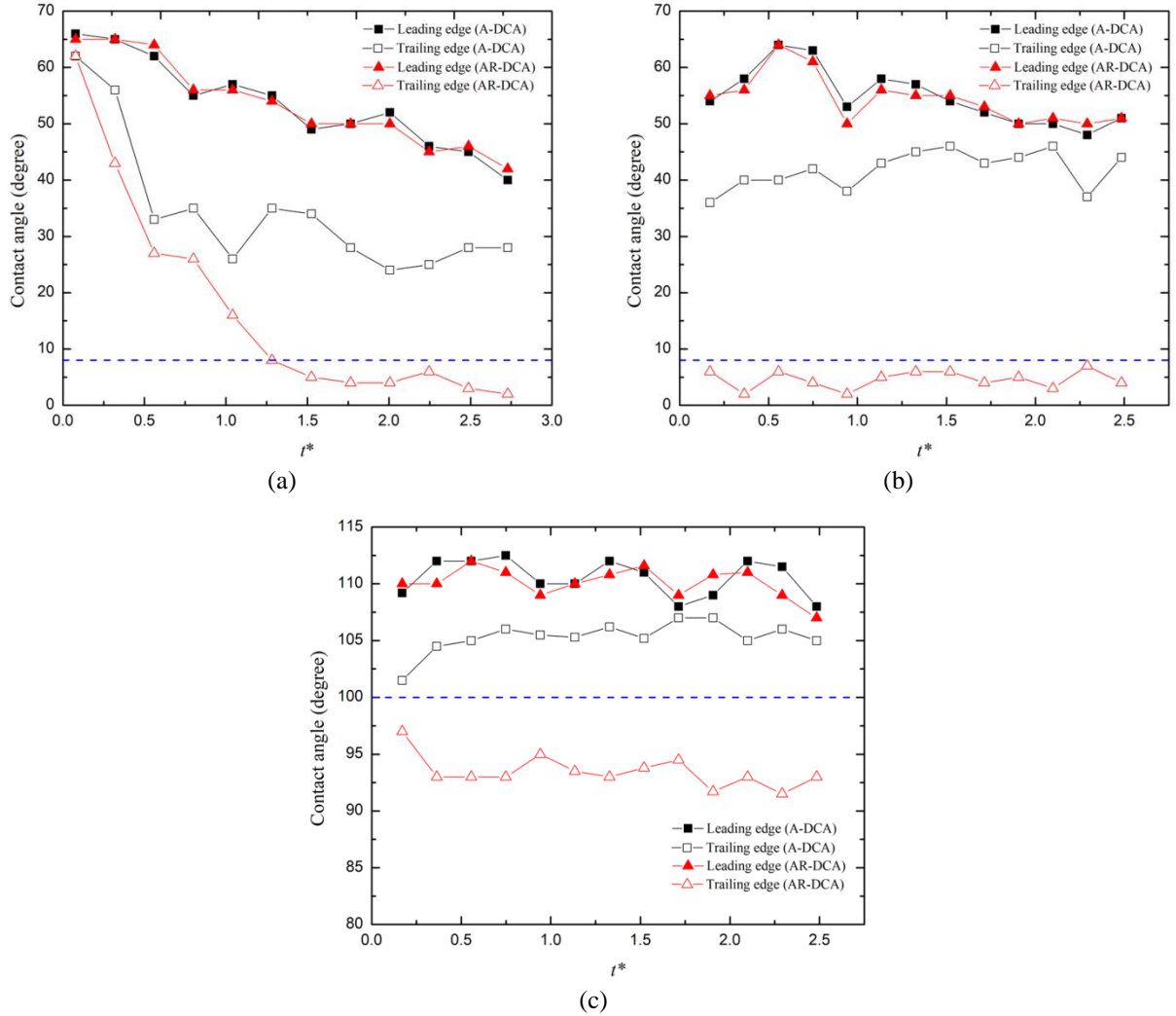


Figure 2.16: Comparisons of contact angles at the leading and trailing edges in terms of  $t^*$ : (a) Case 2; (b) Case 3; (c) Case 4.

For Case 3,  $\theta_{\text{leading}}$  from the two DCA models has a variation range from approximately 48° to 64°,  $\theta_{\text{trailing}}$  from A-DCA model fluctuates around 40° (higher than SCA) while the  $\theta_{\text{trailing}}$  values from AR-DCA model are always below the SCA value, which further explains the reason causing the significantly different numerical results shown in Figure

2.11(b) and (c): for A-DCA model, the trailing edge of the droplet slides down because of the higher  $\theta_{\text{trailing}}$  values (lower wettability); for AR-DCA model, the trailing edge of the droplet remains fixed on the surface due to the lower  $\theta_{\text{trailing}}$  values (higher wettability).

For Case 4,  $\theta_{\text{leading}}$  from the two DCA models varies from about  $107^\circ$  to  $113^\circ$  in the simulation period; the  $\theta_{\text{trailing}}$  from A-DCA model slightly fluctuates from approximately  $102^\circ$  to  $107^\circ$  (always greater than the SCA value  $100^\circ$ ) while the  $\theta_{\text{trailing}}$  from AR-DCA model varies in a range of about  $91^\circ$  to  $97^\circ$  (always smaller than the SCA value). Comparing the corresponding numerical results in Figure 2.13, it is noted that the lower  $\theta_{\text{trailing}}$  values from AR-DCA model enable a longer length of the trailing part and the rebound phenomenon of the droplet tail is only observed from the results of AR-DCA model.

In summary, with the comparisons of contact angle at the leading and trailing edges, it is indicated that the evolution trend of  $\theta_{\text{leading}}$  from A-DCA and AR-DCA model are very similar. However, there is a clear distinction of the  $\theta_{\text{trailing}}$  variations between the two DCA models, which is directly related to the different phenomena in the droplet deformation and evolvement from the qualitative results. It is also further validated that only the AR-DCA model is capable of simulating both advancing and receding phases.

## 2.6. Conclusions

In this study, the A-DCA model and AR-DCA model were proposed to summarize two different methods in Hoffman-function-based DCA simulations, i.e., considering only advancing dynamic contact angles (A-DCA model); considering both advancing and receding dynamic contact angles (AR-DCA model). The comparisons and validations of

A-DCA, AR-DCA and SCA models were conducted systematically for the first time, to investigate the potential of these models to be applied in the PEMFC-related simulations. A DCA evolution map was created to better illustrate and understand the DCA evolving mechanism in the simulation process. For A-DCA and AR-DCA models, the dynamic contact angle is considered as a boundary condition and calculated by Hoffman function using the user defined function (UDF). A series of numerical simulations were conducted based on these three models, and the numerical results were compared to the corresponding experiments documented in Ref. [25, 34]: glycerin droplet impact on horizontal smooth glass (Case 1); water droplet impact on inclined  $45^\circ$  smooth glass (Case 2); water droplet impact on inclined  $10^\circ$  smooth glass (Case 3); water droplet impact on inclined  $10^\circ$  wax (Case 4). The main results and conclusions are summarized as follows:

- (1) For Case 1, the numerical results from these three models were very similar to each other from both side-view and 3D-view, and they all can fit the experimental results very well. This is because Case 1 focused on the early spreading process after the glycerin droplet impact, which makes the DCA effects not evident.
- (2) For Case 2, Case 3, and Case 4, the differences of the numerical results for the three models were remarkable. Compared to the corresponding experiments, it was indicated that only the AR-DCA model is capable of well simulating the droplet deformation and evolvment. The receding effects, e.g., the trailing edge of the droplet fixed on the surface in Case 3, the rebounded trailing edge in Case 4 cannot be well simulated by A-DCA model.

- (3) For Case 2, Case 3, and Case 4, the results from SCA model showed smoother droplet profile than those from DCA models, especially from the 3D-view. However, droplet spreading after impingement on inclined surface is not a stable process, and some phenomena such as raised rim around the edge (Case 2), rebound of trailing edge (Case 4) can be observed from the corresponding experiment and numerical results (AR-DCA model). It was indicated that SCA model can only partially simulate the droplet dynamics and has obvious limitations.
- (4) In order to better understand the phenomena of droplet deformation and evolvment in the spreading process, and investigate the cause of different numerical results between A-DCA and AR-DCA models (especially in Cases 2, 3 and 4), the spreading factor  $x/D$ , dimensionless droplet spreading length  $l/D$  and contact angle values at the leading and trailing edges ( $\theta_{\text{leading}}$  and  $\theta_{\text{trailing}}$ ) were analyzed quantitatively. It was further validated and verified that only the AR-DCA model is able to well simulate the droplet spreading dynamics and phenomena on horizontal and inclined surfaces (Case 1, 2, 3 and 4).

In the future, we will further modify the current AR-DCA model in order to simulate droplet dynamics in gas channel under varied air velocities. In addition, this scientific tool will be used to investigate the gas-liquid phenomena inside the cathodes of proton exchange membrane fuel cells (PEMFCs) with different gas flow field designs, to achieve a fundamental understanding of liquid water behaviors in PEMFCs.

## **Acknowledgements**

The authors are grateful for the support given by the Natural Sciences and Engineering Research Council of Canada (NSERC), the Clean Rail Academic Grant Program from Transport Canada, and the University of Windsor. The authors also would like to thank Compute Canada and Sharcnet for the support of computing resource.

## **References**

- [1] Le AD, Zhou B. A general model of proton exchange membrane fuel cell. *Journal of Power Sources*. 2008 Jul 15;182(1):197-222.
- [2] Jiao K, Zhou B. Accelerated numerical test of liquid behavior across gas diffusion layer in proton exchange membrane fuel cell cathode. *Journal of Fuel Cell Science and Technology*. 2008 Nov 1;5(4):041011.
- [3] Le AD, Zhou B, Shiu HR, Lee CI, Chang WC. Numerical simulation and experimental validation of liquid water behaviors in a proton exchange membrane fuel cell cathode with serpentine channels. *Journal of Power Sources*. 2010 Nov 1;195(21):7302-15.
- [4] Kang S, Zhou B, Cheng CH, Shiu HR, Lee CI. Liquid water flooding in a proton exchange membrane fuel cell cathode with an interdigitated design. *International Journal of Energy Research*. 2011 Dec 1;35(15):1292-311.
- [5] Wang X, Zhou B. Liquid water flooding process in proton exchange membrane fuel cell cathode with straight parallel channels and porous layer. *Journal of Power Sources*. 2011 Feb 15;196(4):1776-94.
- [6] Kang S, Zhou B, Jiang M. Bubble behaviors in direct methanol fuel cell anode with parallel design. *International Journal of Hydrogen Energy*. 2017 Aug 3;42(31):20201-15.

- [7] Zhu X, Sui PC, Djilali N. Numerical simulation of emergence of a water droplet from a pore into a microchannel gas stream. *Microfluidics and Nanofluidics*. 2008 Jun 1;4(6):543-55.
- [8] Zhu X, Sui PC, Djilali N. Three-dimensional numerical simulations of water droplet dynamics in a PEMFC gas channel. *Journal of Power Sources*. 2008 Jun 15;181(1):101-15.
- [9] Qin Y, Du Q, Yin Y, Jiao K, Li X. Numerical investigation of water dynamics in a novel proton exchange membrane fuel cell flow channel. *Journal of Power Sources*. 2013 Jan 15;222:150-60.
- [10] Qin Y, Li X, Jiao K, Du Q, Yin Y. Effective removal and transport of water in a PEM fuel cell flow channel having a hydrophilic plate. *Applied Energy*. 2014 Jan 31;113:116-26.
- [11] Ding Y, Bi X, Wilkinson DP. 3D simulations of the impact of two-phase flow on PEM fuel cell performance. *Chemical Engineering Science*. 2013 Aug 30;100:445-55.
- [12] Ding Y, Anderson R, Zhang L, Bi X, Wilkinson DP. Simulations of two-phase flow distribution in communicating parallel channels for a PEM fuel cell. *International Journal of Multiphase Flow*. 2013 Jun 30;52:35-45.
- [13] Ding Y, Bi XT, Wilkinson DP. Numerical investigation of the impact of two-phase flow maldistribution on PEM fuel cell performance. *International Journal of Hydrogen Energy*. 2014 Jan 2;39(1):469-80.
- [14] Niu Z, Jiao K, Zhang F, Du Q, Yin Y. Direct numerical simulation of two-phase turbulent flow in fuel cell flow channel. *International Journal of Hydrogen Energy*. 2016 Jan 30;41(4):3147-52.
- [15] Niu Z, Wang R, Jiao K, Du Q, Yin Y. Direct numerical simulation of low Reynolds number turbulent air-water transport in fuel cell flow channel. *Science Bulletin*. 2017 Jan 15;62(1):31-9.
- [16] Hoffman RL. A study of the advancing interface. I. Interface shape in liquid—gas systems. *Journal of Colloid and Interface Science*. 1975 Feb 1;50(2):228-41.

- [17]Kistler SF. Hydrodynamics of wetting. Wettability. 1993;6:311-430.
- [18]Šikalo Š, Wilhelm HD, Roisman IV, Jakirlić S, Tropea C. Dynamic contact angle of spreading droplets: Experiments and simulations. Physics of Fluids. 2005 Jun;17(6):062103.
- [19]Mukherjee S, Abraham J. Investigations of drop impact on dry walls with a lattice-Boltzmann model. Journal of Colloid and Interface Science. 2007 Aug 15;312(2):341-54.
- [20]Miller C. Liquid water dynamics in a model polymer electrolyte fuel cell flow channel, MSc Thesis, University of Victoria, 2009.
- [21]Wu TC. Two-phase flow in microchannels with application to PEM fuel cells, PhD Dissertation, University of Victoria, 2015.
- [22]Roisman IV, Opfer L, Tropea C, Raessi M, Mostaghimi J, Chandra S. Drop impact onto a dry surface: Role of the dynamic contact angle. Colloids and Surfaces A: Physicochemical and Engineering Aspects. 2008 Jun 5;322(1):183-91.
- [23]Bussmann M, Mostaghimi J, Chandra S. On a three-dimensional volume tracking model of droplet impact. Physics of Fluids. 1999 Jun;11(6):1406-17.
- [24]Lunkad SF, Buwa VV, Nigam KD. Numerical simulations of drop impact and spreading on horizontal and inclined surfaces. Chemical Engineering Science. 2007 Dec 31;62(24):7214-24.
- [25]Šikalo Š, Tropea C, Ganić EN. Impact of droplets onto inclined surfaces. Journal of Colloid and Interface Science. 2005 Jun 15;286(2):661-9.
- [26]Šikalo Š, Tropea C, Ganić EN. Dynamic wetting angle of a spreading droplet. Experimental Thermal and Fluid Science. 2005 Aug 31;29(7):795-802.
- [27]Fang C, Hidrovo C, Wang FM, Eaton J, Goodson K. 3-D numerical simulation of contact angle hysteresis for microscale two phase flow. International Journal of Multiphase Flow. 2008 Jul 31;34(7):690-705.
- [28]Jiang TS, Soo-Gun OH, Slattery JC. Correlation for dynamic contact angle. Journal of Colloid and Interface Science. 1979 Mar 15;69(1):74-7.



- [29]Tanner LH. The spreading of silicone oil drops on horizontal surfaces. *Journal of Physics D: Applied Physics*. 1979 Sep 14;12(9):1473.
- [30]Legendre D, Maglio M. Numerical simulation of spreading drops. *Colloids and Surfaces A: Physicochemical and Engineering Aspects*. 2013 Sep 5;432:29-37.
- [31]Cox RG. The dynamics of the spreading of liquids on a solid surface. Part 1. Viscous flow. *Journal of Fluid Mechanics*. 1986 Jul;168:169-94.
- [32]Margarinos I, Nikolopoulos N, Marengo M, Antonini C, Gavaises M. VOF simulations of the contact angle dynamics during the drop spreading: standard models and a new wetting force model. *Advances in Colloid and Interface Science*. 2014 Oct 31;212:1-20.
- [33]Shikhmurzaev YD. *Capillary flows with forming interfaces*. CRC Press; 2007 Sep 14.
- [34]Šikalo Š, Ganić EN. Phenomena of droplet–surface interactions. *Experimental Thermal and Fluid Science*. 2006 Nov 30;31(2):97-110.

## CHAPTER 3

### DROPLET BEHAVIORS ON INCLINED SURFACES WITH DYNAMIC CONTACT ANGLES

#### 3.1. Introduction

Proton exchange membrane fuel cell (PEMFC) is a type of energy conversion device that can produce electricity through electrochemical reaction, with the products of only water and heat. In recent years, PEMFCs have received extensive attentions because of the notable features such as low operating temperature, high power density, quick start-up, quietness, etc. [1]. However, water management is still a critical technical barrier that prevents PEMFCs from commercialization. In recent decades, computational modeling and simulation provide viable approaches for the researchers to investigate two-phase flow problems in PEMFCs and obtain a thorough understanding of the liquid water behaviors in flow channels [2].

Among the available literature of the water management simulation in PEMFCs, the static contact angle (SCA) is usually used as a wall boundary condition, such as the previous works [3-8]. However, it is known that when the liquid water interacts with surrounding gas flow in PEMFC channels, the contact angle is unlikely to maintain the equilibrium status and will be altered from the static value. Therefore, the dynamic contact angle (DCA) should be considered in the gas-liquid two-phase flow simulations to predict the real droplet dynamics. So far, very few of research works have been reported for PEMFC-related simulations using DCA model, especially for PEMFCs with complex flow field designs. In a recent work by Wang et al. [9], the DCA model was applied for the first time to simulate the gas-liquid phenomena inside the cathode of

PEMFC with parallel flow design. The liquid water transport, emerging and draining process were studied and the results based on DCA and SCA models are systematically compared. It was noted that the water distribution pattern in the parallel channels from DCA model is more similar to the experiment, indicating the potential of the DCA model in the simulation of liquid water behaviors in PEMFC cathode. Qin et al. [10] developed a dynamic wettability model coupled with dynamic contact angles and sliding angle to simulate water transport in a single straight channel. The results showed that both the dynamic contact angles and sliding angle have significant effects on the liquid water dynamics. Also, it was found the SCA model is not able to well predict the droplet behaviors and the pressure drop in the gas channel.

In order to further develop the DCA model that can be applied in the simulation of water management in PEMFC cathode with complex flow conditions and geometric structures, it is very critical to obtain a fundamental understanding of the droplet behaviors on surfaces or in microchannels with dynamic contact angles. Over the last decades, many research works have been conducted to investigate the contact angle effects on droplet deformation and evolvement, with both experimental and numerical methods. Sikalo et al. [11-15] made significant contributions in this field by investigating droplet behaviors after impingement on surfaces with different conditions, such as droplet property, surface inclined angle, surface wettability, droplet impact Weber number, etc. Different droplet phenomena were observed in the process, e.g., droplet spreading, sliding, rebound, splash, etc. These works not only provide a thorough understanding of droplet characteristics on both inclined and horizontal surfaces, but also indicate that the dynamic contact angle is required to be considered as a boundary condition. Theodorakakos et al.

[16] conducted both experimental and numerical studies to investigate the droplet deformation and detachment from porous material surfaces with air flow. For the experiments, the authors constructed a transparent PEM fuel cell to visualize the water flow and also a single air channel for the visualization of single droplet behaviors. In the corresponding numerical simulation, the advancing and receding contact angles were updated with droplet deformation. It is found that the droplet detachment can be affected by both the air inlet velocity and the droplet location inside the channel. Fang et al. [17] employed a contact angle hysteresis model with volume of fluid (VOF) method to simulate the liquid slug flow in a single microchannel. The Hoffman-Jiang correlation [18] and Hoffman-Voinov-Tanner Law [19] were used to predict the advancing and receding contact angles respectively. An excellent agreement was achieved between the numerical results and corresponding experiment for the slug profile and evolution process, indicating the importance of the DCA model in the simulation of droplet behaviors instead of the SCA model.

Recently, in the work of Malgarinos et al. [20] and Jiang et al. [21], the contact angle models and correlations that have been applied in DCA simulations were summarized. Among the available correlations, Hoffman function is considered as a popular and promising formula to predict dynamic contact angles and has been used in many research works [22-26]. In our previous paper [21], a fundamental understanding of Hoffman function was illustrated by introducing a DCA evolution map. The advancing and receding DCA (AR-DCA) model was proposed based on Hoffman function, which considers both advancing and receding dynamic contact angles in the simulation process. Using the VOF method, the simulations of droplet impact on both horizontal and inclined

surfaces were conducted based on AR-DCA model, advancing DCA (A-DCA) model and SCA model. The results were systematically compared to the corresponding experiments by Sikalo et al. [12, 13], in both qualitative and quantitative ways. It was found that only the AR-DCA model is able to well predict the droplet behaviors among the three models, showing its potential to be applied in the DCA simulation for the complex flow domain.

In this paper, we further extend our previous work [21] by simulating droplet behaviors on inclined surfaces under various conditions, i.e., different impact velocities, impact angles, surface wettabilities and droplet viscosities. The droplet deformation and evolving phenomena from the numerical results based on these parameters will be compared and discussed, in both qualitative and quantitative methods.

### **3.2. Numerical Methodology**

In this paper, the VOF method is employed to track the gas-liquid interface, coupled with the validated AR-DCA model [21] to apply dynamic contact angle as wall boundary conditions. The corresponding governing equations for VOF method and the methodology to implement DCA have been reported in our previous paper. More details can be found in Ref. [21].

### **3.3. Numerical Model Description**

#### **3.3.1. Experiments for Validation**

In this study, a series of cases will be simulated to investigate the droplet behaviors under different inclined angles, surface wettabilities, droplet impact velocities and droplet viscosities. The schematic view of the experiment is shown in Figure 2.2 in Chapter 2. The detailed parameters of each case are identical to those from Sikalo's experiments

[15] and can be found in Table 3.1. The comparisons of these cases will be conducted by the following sections: 1) Effects of impact velocity: Case 1, 2 and 3 (hydrophilic surface), Case 4, 5 and 6 (hydrophobic surface); 2) Effects of impact angle: Case 1, 7 and 8 (hydrophilic surface), Case 4, 9 and 10 (hydrophobic surface); 3) Effects of droplet viscosity: Case 11 (with different viscosities).

**Table 3.1 Detailed Liquid Property, Surface Wettability and Impact Velocity for Selected Cases [15]**

Case #	Liquid	Initial droplet diameter $D$ (mm)	Impact angle $\alpha$ (°)	Viscosity $\mu$ (mPa s)	Surface material	Input SCA (°)	Weber number ( $We$ )	Impact velocity $V_p$ (m/s)
1	Water	2.7	10	1.0	Smooth glass	8	50	1.163
2	Water	2.7	10	1.0	Smooth glass	8	161	2.088
3	Water	2.7	10	1.0	Smooth glass	8	391	3.253
4	Water	2.7	10	1.0	Wax	100	50	1.163
5	Water	2.7	10	1.0	Wax	100	161	2.088
6	Water	2.7	10	1.0	Wax	100	391	3.253
7	Water	2.7	9.5	1.0	Smooth glass	8	50	1.163
8	Water	2.7	20	1.0	Smooth glass	8	50	1.163
9	Water	2.7	5	1.0	Wax	100	50	1.163
10	Water	2.7	20	1.0	Wax	100	50	1.163
11	Glycerin	2.45	9	Varied	Smooth glass	15	51	1.037

### **3.3.2. Computational Domain and Grid Independency**

In this study, the computational domain is the same as the one used in the previous chapter. The grid independency check has also been conducted. More detailed descriptions can be referred to Section 2.4.2 and 2.4.3 in Chapter 2.

## **3.4. Results and Discussion**

Sikalo et al. [15] conducted a comprehensive experimental study on droplet impact on inclined surfaces and investigated the effects of impact parameters on the droplet behavior and spreading phenomena. In this study, we further apply the validated AR-DCA model [21] to simulate the droplet spreading and evolvement process on inclined surfaces under different impact velocities, impact angles and droplet viscosities. The numerical results are presented in the following sections and also compared to the same corresponding experiments from the literature.

### **3.4.1. Effects of Impact Velocity**

#### **3.4.1.1. Qualitative Results**

Figure 3.1(a)-(b) show the experimental and numerical results for the impact of a water droplet on smooth glass ( $\alpha = 10^\circ$ ) with impact Weber number 50, 161 and 391, which is corresponding to the Case 1, 2 and 3 respectively in Table 3.1. From the qualitative comparison, it is noted that the simulation results based on the current DCA model have excellent agreement with the same experiment from the literature. As shown in Figure 3.1(a), under the low impact Weber number (50), the droplet slides down along the surface with small liquid film at the trailing edge, with minor distortion on the droplet shape at the early stage ( $t = 1, 2$  ms, the second and third droplet profile from the top).

When it comes to 9 ms, the droplet almost fully spreads onto the surface. With the increase of the Weber number is to 161 and 391, the droplet leading edge will slide down faster along the surface (at  $t = 1, 2$  ms, the distance between the droplet leading edge and impact point is increased) whereas the trailing edge remains fixed on the surface because of the high wettability of the smooth glass.

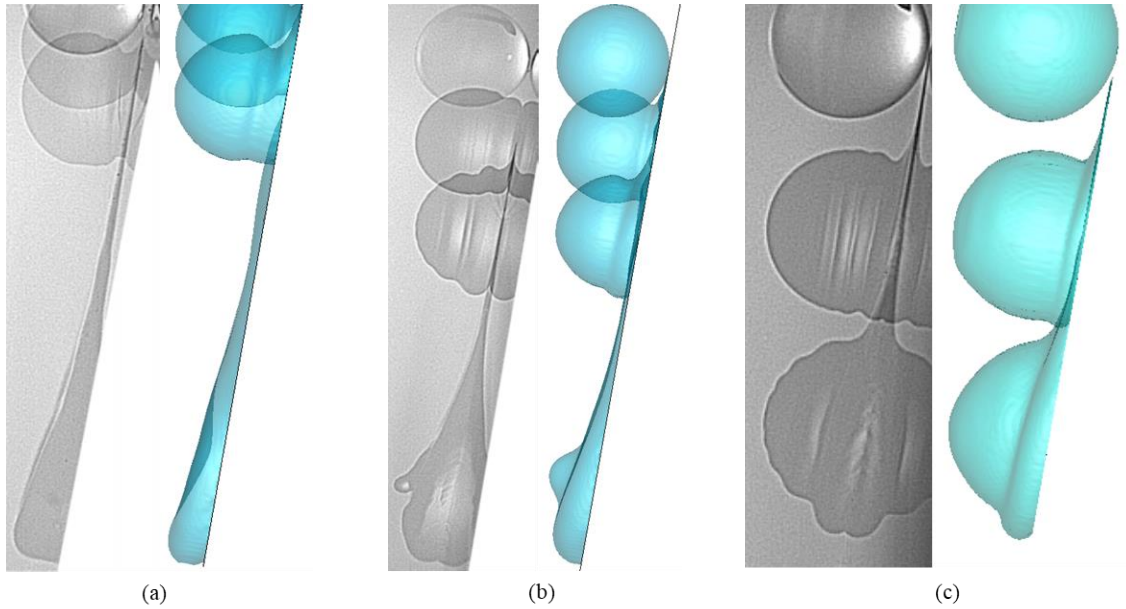


Figure 3.1: Impact of water droplet on smooth glass with  $\alpha = 10^\circ$  and different impact velocities (Left side: experiment from Sikalo [15]; Right side: numerical results in the present study): (a)  $We = 50$ ,  $t = 0, 1, 2, 9$  ms; (b)  $We = 161$ ,  $t = 0, 1, 2, 5$  ms; (c)  $We = 391$ ,  $t = 0, 1, 2$  ms.

Besides the hydrophilic surface, the droplet behaviors on the hydrophobic surface (wax) are also simulated under different impact velocities (Case 4, 5, 6 in Table 3.1) and the results are shown in Figure 3.2(a)-(c). Due to the low wettability, the droplet trailing edge will slide down with the droplet and form a slug shape as shown in the last droplet profile in Figure 3.2(a) ( $t = 9$  ms) and Figure 3.2(b) ( $t = 5$  ms). The effects of impact velocity can also be observed by comparing the first two droplet profile ( $t = 1, 2$  ms) after impact: with the increase of the impact velocity, the droplet slides down faster on the surface, leading to a longer droplet tail formed at the trailing side of the droplet.



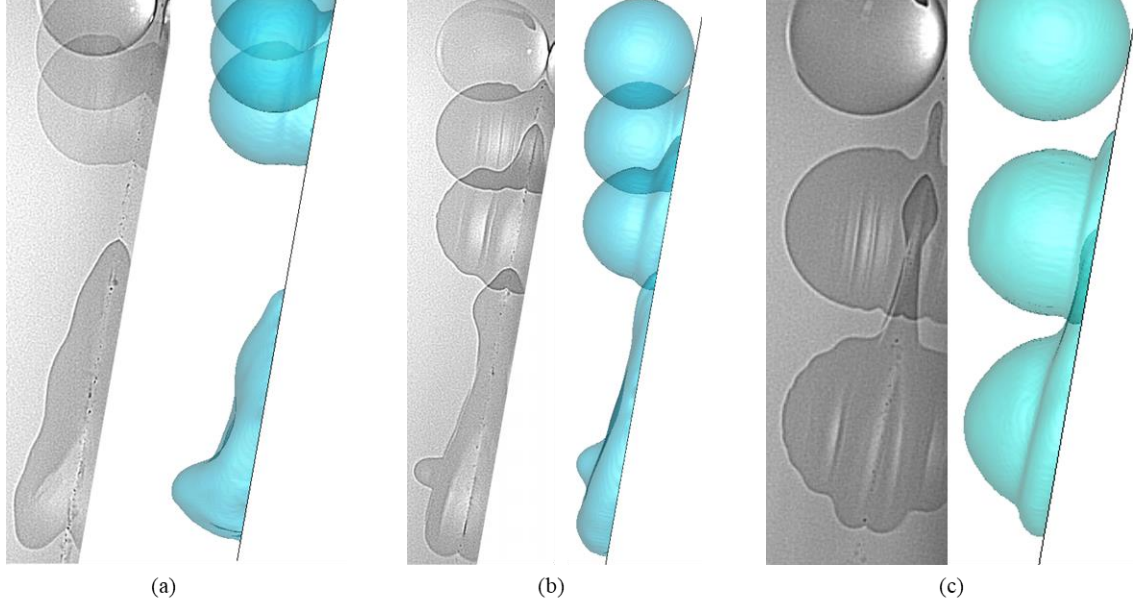


Figure 3.2: Impact of water droplet on wax with  $\alpha = 10^\circ$  and different impact velocities (Left side: experiment from Sikalo [15]; Right side: numerical results in the present study): (a)  $We = 50$ ,  $t = 0, 1, 2, 9$  ms; (b)  $We = 161$ ,  $t = 0, 1, 2, 5$  ms; (c)  $We = 391$ ,  $t = 0, 1, 2$  ms.

#### 3.4.1.2. Quantitative Results

Only from the qualitative observation, it is not sufficient to well reflect the influence of the impact velocity on the droplet spreading process and deformation, therefore the quantitative analysis is conducted based on the spreading factor ( $x/D$ ) at the leading and trailing side ( $x_{\text{leading}}/D$  and  $x_{\text{trailing}}/D$ ) in terms of the dimensionless time  $t^*$  ( $t^* = t V_p/D$ ).

Figure 3.3(a) shows the comparison of spreading factor ( $x/D$ ) versus  $t^*$  under Weber number 50, 161, 391 for water droplet impact on  $10^\circ$  smooth glass from the simulation. It is noted that the variation trends for both leading edge and trailing edge are almost identical: the  $x_{\text{leading}}/D$  continuously grows up with time in the process, which corresponds to the droplet leading edge sliding away from the impact point in the qualitative results (Figure 3.1); whereas for the trailing edge, the values of  $x_{\text{trailing}}/D$  are all close to zero, which represents the phenomenon of the trailing edge fixed on the surface in the droplet spreading. These evolution trends of spreading factor are in good

agreement with the experimental data from Sikalo et al. [15] (Figure 3.3(b)). Also, Figure 3.4 shows the evolution of dimensionless spreading length  $l/D$  versus  $t^*$  from the simulation and it can be seen that nearly no difference occurs for the evolution of  $l/D$  under different impact velocities, indicating the insignificant effects of the impact velocity on the droplet spreading on the hydrophilic surface.

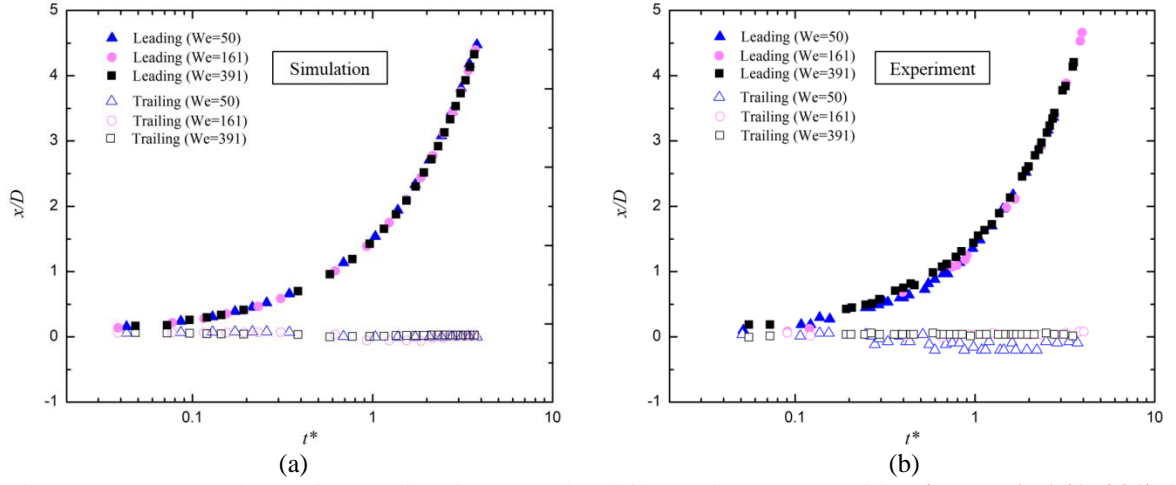


Figure 3.3: Comparison of spreading factor under different impact velocities ( $We = 50, 161, 391$ ) for water droplet impact on  $10^\circ$  smooth glass: a) simulation and b) experiment [15].

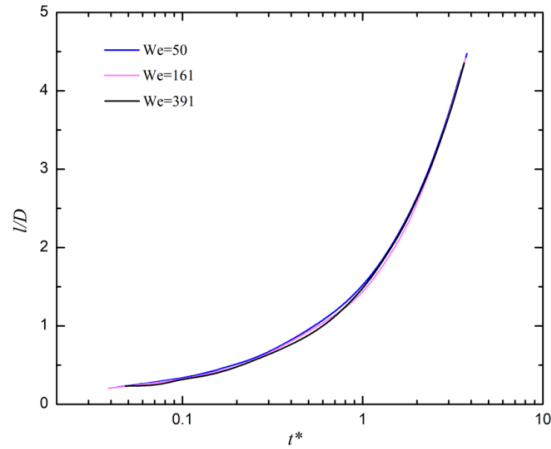


Figure 3.4: Comparison of dimensionless spreading length under different impact velocities ( $We = 50, 161, 391$ ) for water droplet impact on  $10^\circ$  smooth glass (simulation).

For the hydrophobic case, as shown in Figure 3.5(a), the spreading factor at the trailing edge shows a significantly different trend: the  $x_{\text{trailing}}/D$  varies around zero before  $t^* = 0.35$ , indicating that the trailing edge is still fixed on the surface at the early spreading stage; after that, the spreading factor declines with  $t^*$ , which corresponds to the sliding of the droplet trailing edge along with the droplet due to the low wettability of the surface. The negative value of  $x_{\text{trailing}}/D$  means that the trailing edge is sliding down and located on the same side as the leading edge relative to the impact point. It is also noted that after about  $t^* = 2.0$ , the higher impact  $We$  will lead to higher value of  $x_{\text{trailing}}/D$ , indicating the trailing edge slides down less distance from the impact point, which is in good consistency with the experimental data (Figure 3.5(b)) and results in longer droplet spreading length, as shown in Figure 3.6.

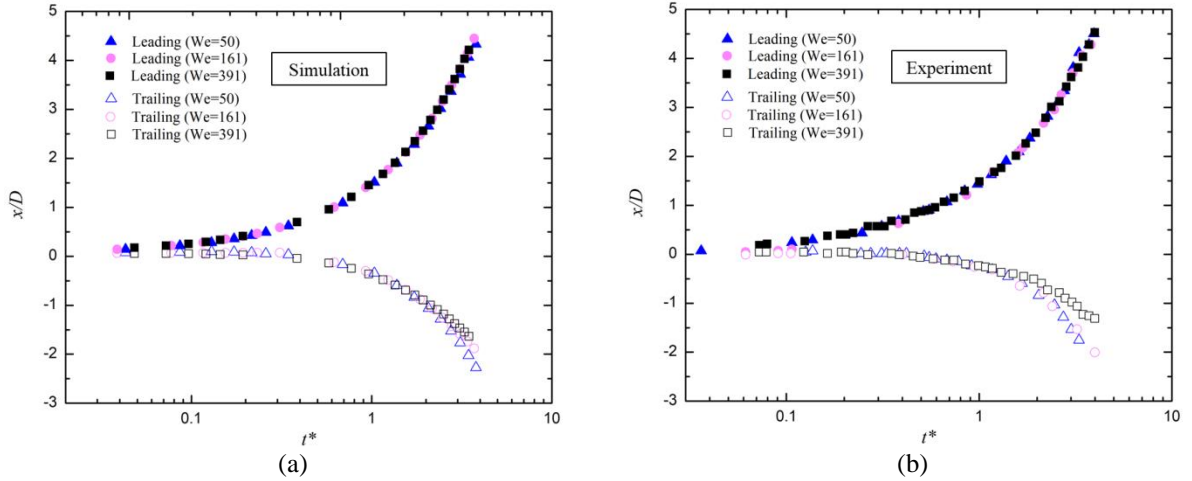


Figure 3.5: Comparison of spreading factor under different impact velocities ( $We = 50, 161, 391$ ) for water droplet impact on 10° wax: a) simulation and b) experiment [15].

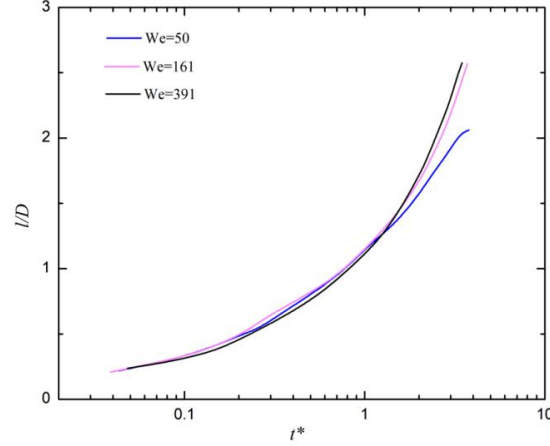


Figure 3.6: Comparison of dimensionless spreading length under different impact velocities ( $We = 50, 161, 391$ ) for water droplet impact on  $10^\circ$  wax (simulation).

### 3.4.2. Effects of Impact Angle

#### 3.4.2.1. Qualitative Results

Figure 3.7(a)-(c) show the droplet behavior on smooth glass under different impact angles ( $\alpha = 9.5^\circ, 10^\circ$  and  $20^\circ$ ) respectively (corresponding to Case 7, 1 and 8), from the experiment [15] and numerical simulation. The impact Weber number is set as 50 for all the three cases. For Case 7, it is observed that the droplet is deformed from the spherical shape to the long liquid film when the droplet leading edge is sliding down; no slipping of the trailing edge occurs, which is a common phenomenon on the hydrophilic surface, as shown in Figure 3.7(a). Excellent agreement is also obtained between the numerical results and the experiment at multiple instants, further demonstrating the capability of the current DCA model to predict the droplet behaviors and evolvement. From the qualitative results, it can be seen that when the impact angle  $\alpha$  is increased from  $9.5^\circ$  to  $20^\circ$ , the droplet has stronger tendency to spread at the leading edge, as shown in Figure 3.7(a-c) at  $t = 2$  ms. This is because under larger impact angle  $\alpha$ , the normal impact Weber number  $We_n$  ( $We_n = We \cdot \sin \alpha$ ) will also increase and in turn facilitate the deposition of droplet on the surface.

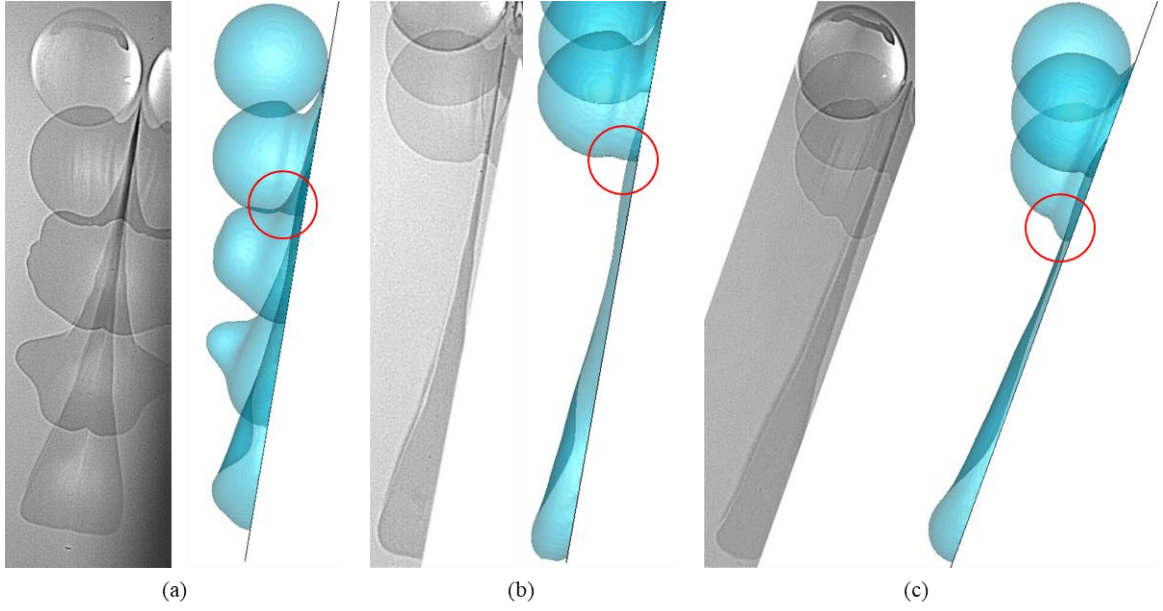


Figure 3.7: Impact of water droplet on smooth glass with  $We = 50$  and different impact angle  $\alpha$  (Left side: experiment from Sikalo [15]; Right side: numerical results in the present study): (a)  $\alpha = 9.5^\circ$ ,  $t = 0, 2, 4, 6, 8$  ms; (b)  $\alpha = 10^\circ$ ,  $t = 0, 1, 2, 9$  ms; (c)  $\alpha = 20^\circ$ ,  $t = 0, 1, 2, 9$  ms.

Similar phenomenon can also be observed on hydrophobic surfaces, as shown in Figure 3.8(a)-(c) for the impact of water droplet on wax with  $\alpha = 5^\circ$ ,  $10^\circ$  and  $20^\circ$ . Meanwhile, some typical characteristics of the water-wax system are reflected: with time, both the leading and trailing edges slide along the surface and the droplet is deformed into the slug shape; the lower impact angle leads to relatively higher apex height of the droplet, mainly because of the dominated inertial force in the tangential direction of the surface. However, from only the phenomenological observation, the distinction of the droplet spreading is not able to be well illustrated. Therefore, the analysis based on quantitative results is required and will be discussed in the following section.

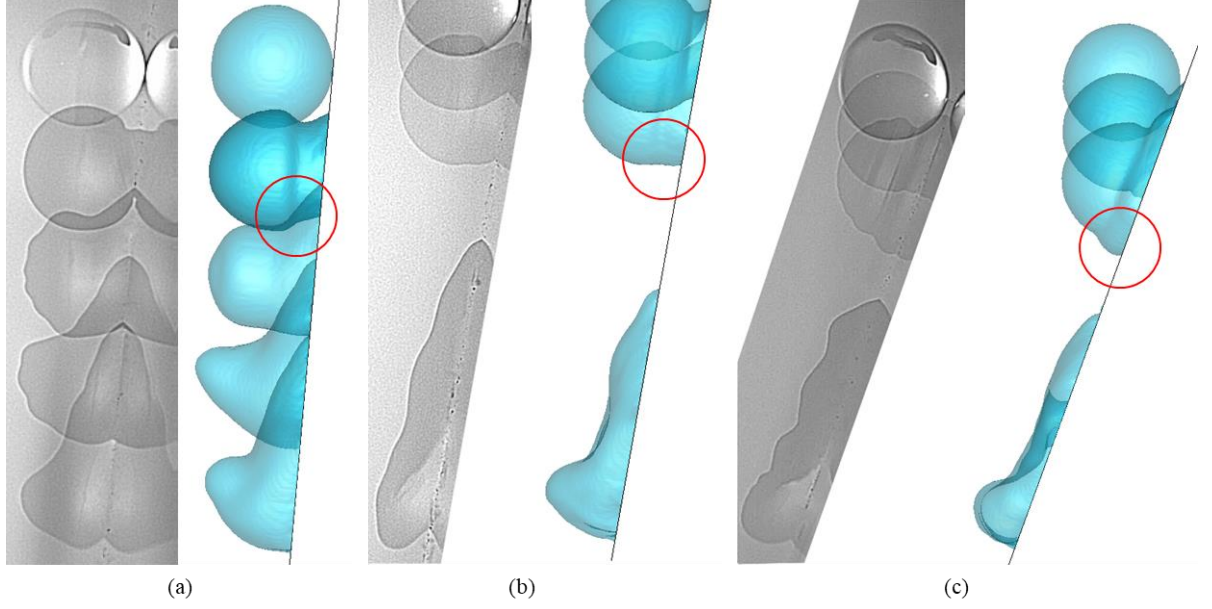


Figure 3.8: Impact of water droplet on wax with  $We = 50$  and different impact angle  $\alpha$  (Left side: experiment from Sikalo [15]; Right side: numerical results in the present study): (a)  $\alpha = 5^\circ$ ,  $t = 0, 2, 4, 6, 8$  ms; (b)  $\alpha = 10^\circ$ ,  $t = 0, 1, 2, 9$  ms; (c)  $\alpha = 20^\circ$ ,  $t = 0, 1, 2, 9$  ms.

### 3.4.2.2. Quantitative Results

Figure 3.9(a) and (b) show the quantitative results for the impact angle effects on droplet behaviors under water-smooth glass system from simulation and experiment respectively (only the experimental data for the cases under  $\alpha = 10^\circ$  and  $20^\circ$  is provided in the literature [15]). It is noted that the evolution of the leading edge is not significantly affected by the impact angle, whereas for the trailing edge, the value of  $x_{\text{trailing}}/D$  will be slightly higher with the increase of the impact angle  $\alpha$ , which results in longer droplet spreading length, as shown in Figure 3.10. This trend is also reflected from the observation of qualitative results in Figure 3.7.

For the water-wax system under various impact angles, the typical evolution trend for spreading factor can also be observed: the  $x_{\text{leading}}/D$  continuously rises up with  $t^*$ , as shown in Figure 3.11, from both simulation and experiment, indicating the fast sliding of

the droplet leading edge; meanwhile, similar to the hydrophilic case, the evolution of  $x_{\text{leading}}/D$  shows less dependence on the impact angle  $\alpha$ ; whereas for the trailing edge, it is noted the higher impact angle leads to higher value of  $x_{\text{trailing}}/D$ , indicating stronger tendency of spreading at the trailing edge, which in turn results in a larger droplet elongation on the surface, as shown in Figure 3.12.

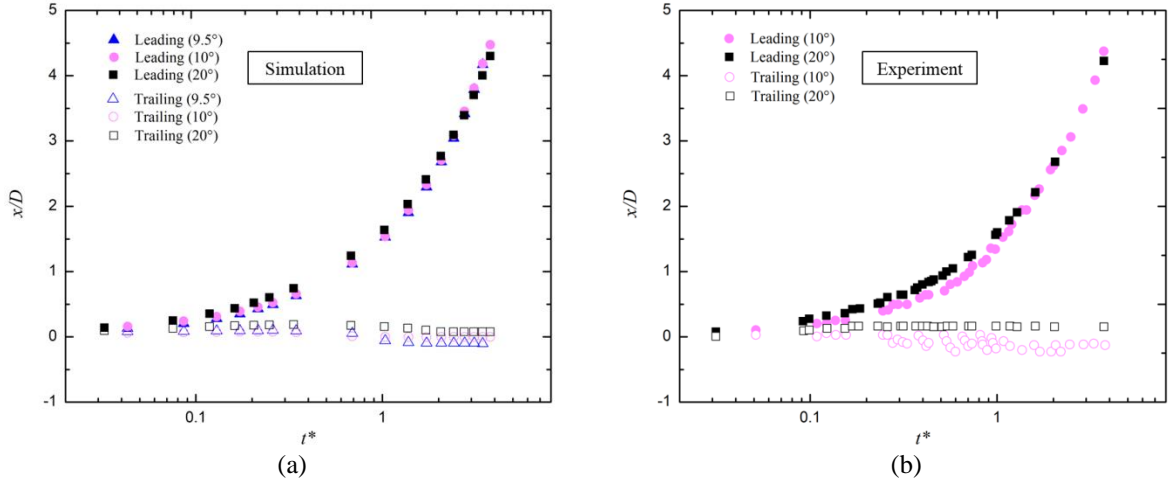


Figure 3.9: Comparison of spreading factor under different impact angles ( $\alpha = 9.5^\circ, 10^\circ, 20^\circ$ ) for water droplet impact on smooth glass with  $We = 50$ : a) simulation and b) experiment [15].

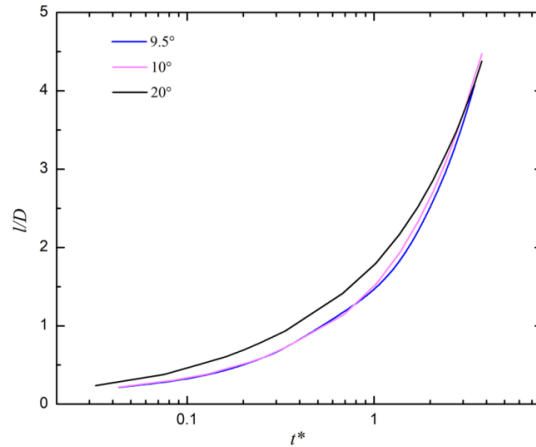


Figure 3.10: Comparison of dimensionless spreading length different impact angles ( $\alpha = 9.5^\circ, 10^\circ, 20^\circ$ ) for water droplet impact on smooth glass with  $We = 50$  (simulation).

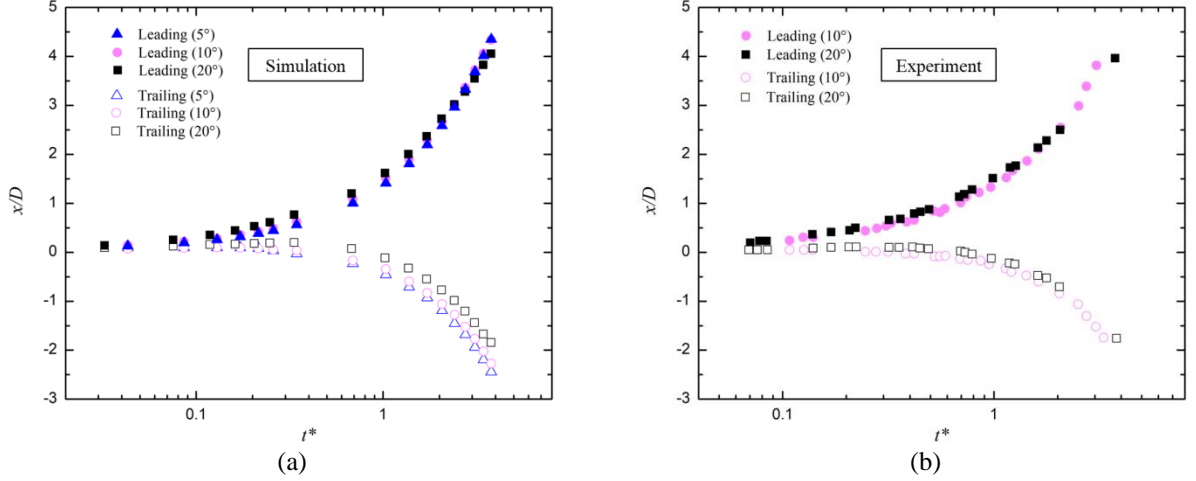


Figure 3.11: Comparison of spreading factor under different impact angles ( $\alpha = 5^\circ, 10^\circ, 20^\circ$ ) for water droplet impact on wax with  $We = 50$ : a) simulation and b) experiment [15].

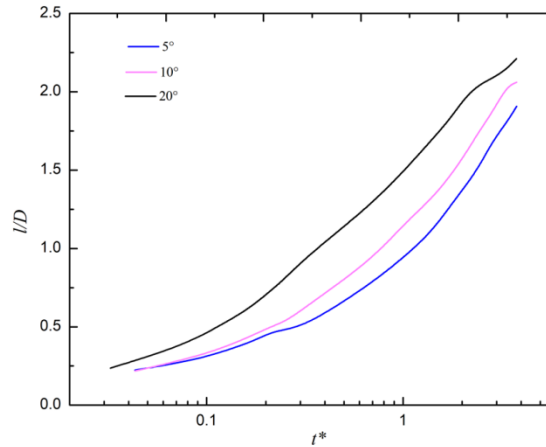


Figure 3.12: Comparison of dimensionless spreading length different impact angles ( $\alpha = 5^\circ, 10^\circ, 20^\circ$ ) for water droplet impact on wax with  $We = 50$  (simulation).

### 3.4.3. Effects of Droplet Viscosity

The case of glycerin impact on  $9^\circ$  smooth glass with impact  $We$  of 391 is selected to investigate the viscosity effects on the droplet behaviors. In the work of Sikalo [15], two different droplet deformation phenomena are reported: one is partial rebound and another is droplet deposition, as shown in Figure 3.13(a) and (b) respectively. The numerical results based on the original viscosity (0.116 Pa s) are shown in Figure 3.13(c) and the time interval among the captured droplets (3 ms) is identical to the experiment. It is



noticed that using the original properties provided in the literature, only the droplet deposition phenomenon can be well simulated based on the current DCA model: the third and fourth droplet profiles (from top to bottom) are still in the spreading stage and the trailing edge of the droplet remains fixed on the surface when it slides down, which is similar to the experimental results in Figure 3.13(b); whereas in Figure 3.13(a), it can be observed that the droplet profile at the same instants start to rebound from the surface.

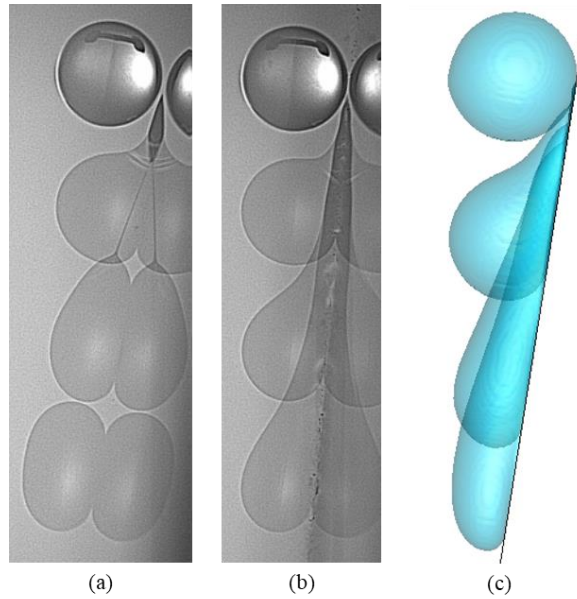


Figure 3.13: Impact of glycerin droplet onto wax with  $We = 391$ : (a) droplet partial rebound in the experiment [15]; (b) droplet deposition in the experiment [15]; (c) simulation results.

Since the glycerin solution used in the experiment is mixed by 85 vol.% glycerin and 15 vol.% water, and the droplet extracted from the solution is very tiny, there could be some unavoidable error in the measurement and experiment process, and some of the liquid properties (such as density, surface tension, viscosity, etc.) of the droplet may become different from those provided in the literature. Considering the “rebound” phenomenon of the droplet is observed from the experiment and it cannot be well-predicted in the numerical simulation, the viscosity could be a potential dominated factor in this case.

Thus, the effects of different viscosities on droplet impact and deformation are investigated in this section.

### 3.4.3.1. Recalculation of the Dynamic Viscosity for the Glycerin Solution

The Refutas Equation [27, 28] is commonly used to calculate the viscosity of the mixture of two or more liquids. Firstly, we applied this Refutas equation to recalculate the viscosity of the 85% glycerin solution. The viscosity bending number (VBN) for each component (glycerin and water in the present study) is calculated by:

$$VBN = 14.534 \times \ln(\ln(\nu + 0.8)) + 10.975 \quad (3.1)$$

where  $\nu$  is the kinematic viscosity (unit: centistokes (cSt)).

Then the VBN of the blend (mixture) can be determined by:

$$VBN_{Blend} = x_A \times VBN_A + x_B \times VBN_B \quad (3.2)$$

where  $x_A$  and  $x_B$  are the mass fraction of glycerin and water in the blend respectively.

Finally, the kinematic viscosity of the blend can be solved by:

$$\nu = \exp(\exp((VBN_{Blend} - 10.975)/14.534)) - 0.8 \quad (3.3)$$

And the dynamic viscosity  $\mu$  of the blend will be:

$$\mu = \rho \cdot \nu \quad (3.4)$$

The calculation results are shown in Table 3.2 (the mixture density and surface tension are the same as provided in the experiment [15] in order to consider only the viscosity effects in this case). Based on the calculation, it is noted that the value of 0.1676 Pa s is

obtained for the droplet viscosity, which is about 44.5% higher than the original viscosity provided in the literature. Therefore, the numerical simulations based on various viscosities, i.e.,  $\mu^*$  (0.1676 Pa s),  $1.5\mu^*$  (0.2514 Pa s),  $2\mu^*$  (0.3352 Pa s) and  $3\mu^*$  (0.5028 Pa s), are further conducted.

**Table 3.2 Calculation Results for the Viscosity of the Glycerin Solution based on Refutas Equation**

Liquid	Volume ( $\text{m}^3$ )	Density ( $\text{kg}/\text{m}^3$ )	Mass (kg)	Dynamic Viscosity (Pa s)	Kinematic Viscosity ( $\text{m}^2/\text{s}$ )	Kinematic Viscosity (cSt)	VBN	Mass fraction
Water	0.15	996	149.4	0.001	1.0E-6	1.004	<b>3.31</b>	0.122
Glycerin	0.85	1260	1071	0.95	7.54E-4	753.97	<b>38.46</b>	0.878
Solution	1	1220.4	1220.4	<b>0.1676</b>	1.37E-4	<b>137.33</b>	<b>34.16</b>	1

#### 3.4.3.2. Numerical Results based on Different Viscosities

Figure 3.14 and Figure 3.15 show the comparisons of numerical results based on the various viscosities at simulation time  $t = 1$  ms, 4 ms, 7 ms and 10 ms, from side-view and 3D-view respectively. From the qualitative results, it can be seen that with the increase of the glycerin solution viscosity, the trailing edge of the droplet starts to detach from the surface in the early stage after the impact (the second droplet profile ( $t = 4$  ms) in Figure 3.14(a)-(d)). With time, the trailing edge of the droplet still remains fixed on the surface under the cases of  $\mu^*$ ,  $1.5\mu^*$ , and  $2\mu^*$  at  $t = 7$  ms and 10 ms, as shown in Figure 3.14 and 3.15(a)-(c). However, when the viscosity is further increased to  $3\mu^*$ , the droplet “rebound” phenomenon is observed at  $t = 7$  ms and 10 ms and the trailing edge is no longer attached on the surface, which is more similar to the “partial rebound” result in the experiment (Figure 3.13(a)).

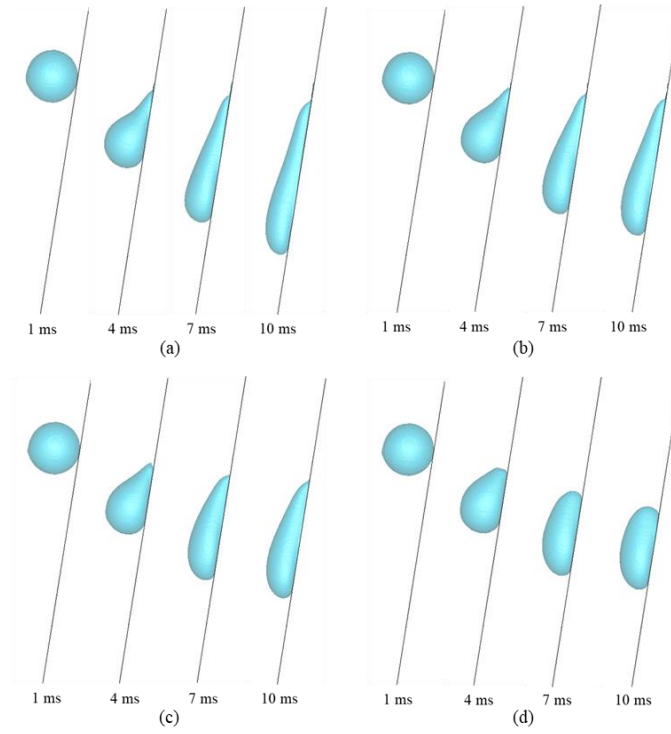


Figure 3.14: Comparison of numerical results with different viscosities (side-view): a)  $\mu^*$ ; b)  $1.5\mu^*$ ; c)  $2\mu^*$ ; d)  $3\mu^*$ .

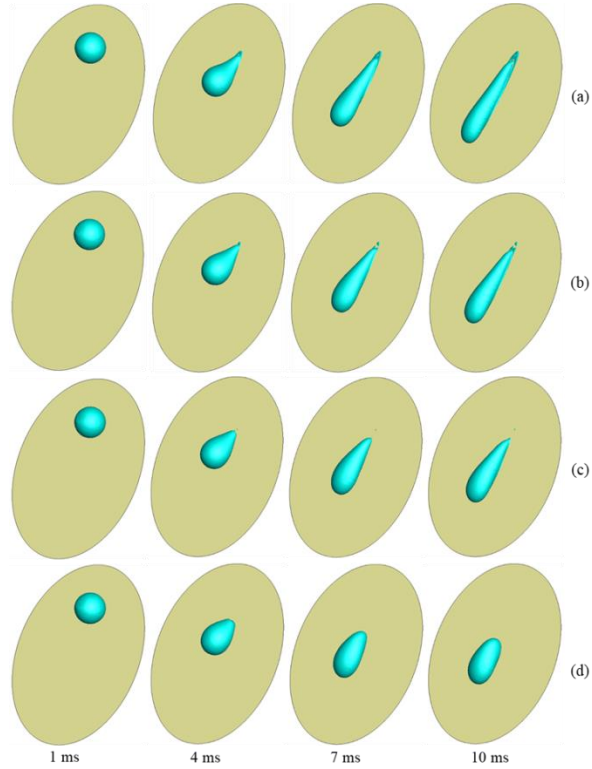


Figure 3.15: Comparison of numerical results with different viscosities (3D-view): a)  $\mu^*$ ; b)  $1.5\mu^*$ ; c)  $2\mu^*$ ; d)  $3\mu^*$ .

Additionally, the evolvement of the droplet spreading factor ( $x/D$ ) and dimensionless spreading length ( $l/D$ ) versus  $t^*$  under  $\mu^*$  to  $3\mu^*$  are also investigated and the results are shown in Figure 3.16.

It is noted that on one hand, the higher droplet viscosity will lead to lower value of  $x_{\text{leading}}/D$ , as shown in Figure 3.16(a), indicating the droplet leading edge slides shorter distance away from the impact point; on the other hand, higher viscosity will also result in lower value of  $x_{\text{trailing}}/D$ , indicating longer distance between droplet trailing edge and the impact point. Also, from Figure 3.16(b), it is reflected that the higher viscosity can significantly shorten the droplet spreading length. Meanwhile, it is observed that the dimensionless spreading length  $l/D$  is continuously increased with  $t^*$  in the sliding process under the cases of  $\mu^*$ ,  $1.5\mu^*$  and  $2\mu^*$ . However, for the viscosity of  $3\mu^*$ , the variation of  $l/D$  firstly increases with  $t^*$  and then at about  $t^* = 3$ ,  $l/D$  will reach a maximum value (1.41); after this point, the dimensionless spreading length starts to decrease, which is corresponding to the rebound phenomenon in Figure 3.14(d) and Figure 3.15(d). Therefore, it can be concluded that the viscosity has notable effects on the droplet behaviors. The higher viscosity will lead to higher adhesive force between the droplet and surface, making the droplet possess a strong tendency to adhere to the boundary wall. Also, the increase of viscosity will cause a transition for the droplet evolvement from deposition to partial rebound.

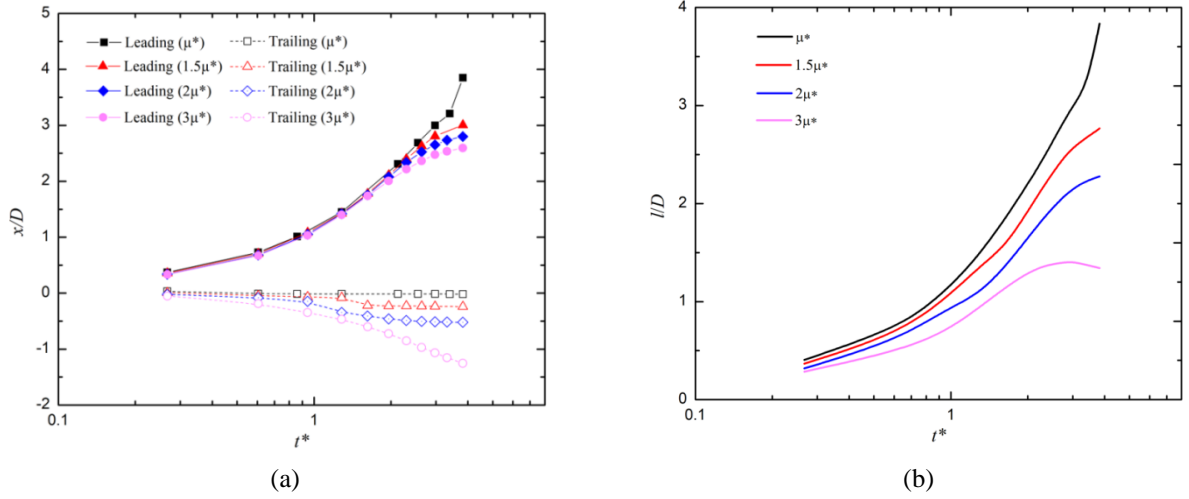


Figure 3.16: Comparison of a) spreading factors and b) dimensionless spreading length ( $l/D$ ) for glycerin droplet with different viscosities impact on smooth glass.

### 3.5. Conclusions

In this study, using the VOF method, a series of simulations for droplet impact on inclined surfaces were conducted based on the DCA model. The effects of the droplet impact velocity (associated to impact Weber number), impact angle  $\alpha$  and the droplet viscosity were considered to investigate different droplet behaviors and evolving phenomena in the spreading process. The numerical results from all the cases were validated against the corresponding experiments from Sikalo [15] and excellent agreement was achieved for the droplet deformation at multiple instants, which further indicated the capability of our AR-DCA model [21] to simulate droplet behaviors and regimes under various conditions. The quantitative results of the selected cases were also compared by analyzing the spreading factor ( $x/D$ ) and dimensionless spreading length ( $l/D$ ) as a function of dimensionless time  $t^*$  ( $t^* = t V_p/D$ ). The main findings are as follows:

- (1) The effects of impact velocity on droplet behaviors were studied by comparing the cases of water droplet impact on 10 ° smooth glass (hydrophilic surface) and wax (hydrophobic surface) under impact Weber number 50, 161 and 391. For the water-smooth glass cases, the droplet leading edge fast slid away from the impact point while the trailing edge remained fixed, which is a typical phenomenon occurring on highly wettable surface. Under this condition, the impact velocity has no significant influence on the spreading factors at the leading and trailing edge. The evolution of  $x_{\text{leading}}/D$  and  $x_{\text{trailing}}/D$  versus  $t^*$  were very similar among different impact  $We$ , leading to no obvious distinction for the  $l/D$  versus  $t^*$ . For the water-wax cases (less wettable surface), the trailing edge also slid down with the droplet. It was found that the higher impact velocity leads to a decrease of the sliding distance of the trailing edge and the leading edge is not affected, which results in an increase of the spreading length (distance between leading and trailing edges).
- (2) The effects of impact angle on droplet behaviors were investigated by comparing the cases of water droplet impact on smooth glass (impact angle 9.5 °, 10 °, 20 °) and wax (impact angle 5 °, 10 °, 20 °) under impact Weber number 50. The results indicated that, for both hydrophilic and hydrophobic cases, the higher impact angle will lead to an increase of  $x_{\text{trailing}}/D$ , whereas the evolution of  $x_{\text{leading}}/D$  shows much less dependence on the impact velocity. Also, both the qualitative and quantitative results showed that higher impact angle leads to a larger droplet elongation.

(3) For the case of glycerin droplet impact on smooth glass, using the original droplet properties provided in the literature, the current DCA model can well predict the deposition process in the experiment while the partial rebound of the droplet was not reflected. However, with the increase of the droplet viscosity in the simulation, some interesting phenomena can be observed: on one hand, higher droplet viscosity causes the droplet to rebound from the surface more easily; on the other hand, higher viscosity leads to the reduction of  $x_{\text{leading}}/D$  and  $x_{\text{trailing}}/D$ , indicating the shortening of the droplet sliding distance on the surface.

## References

- [1] Wang Y, Chen KS, Mishler J, Cho SC, Adroher XC. A review of polymer electrolyte membrane fuel cells: technology, applications, and needs on fundamental research. *Applied Energy*. 2011 Apr 1;88(4):981-1007.
- [2] Ferreira RB, Falcão DS, Oliveira VB, Pinto AM. Numerical simulations of two-phase flow in proton exchange membrane fuel cells using the volume of fluid method—A review. *Journal of Power Sources*. 2015 Mar 1;277:329-42.
- [3] Quan P, Zhou B, Sobiesiak A, Liu Z. Water behavior in serpentine micro-channel for proton exchange membrane fuel cell cathode. *Journal of Power Sources*. 2005 Dec 1;152:131-45.
- [4] Le AD, Zhou B. A general model of proton exchange membrane fuel cell. *Journal of Power Sources*. 2008 Jul 15;182(1):197-222.
- [5] Kang S, Zhou B, Jiang M. Bubble behaviors in direct methanol fuel cell anode with parallel design. *International Journal of Hydrogen Energy*. 2017 Aug 3;42(31):20201-15.



- [6] Qin Y, Li X, Jiao K, Du Q, Yin Y. Effective removal and transport of water in a PEM fuel cell flow channel having a hydrophilic plate. *Applied Energy*. 2014 Jan 31;113:116-26.
- [7] Jo JH, Kim WT. Numerical simulation of water droplet dynamics in a right angle gas channel of a polymer electrolyte membrane fuel cell. *International Journal of Hydrogen Energy*. 2015 Jul 13;40(26):8368-83.
- [8] Ferreira RB, Falcão DS, Oliveira VB, Pinto AM. 1D+ 3D two-phase flow numerical model of a proton exchange membrane fuel cell. *Applied Energy*. 2017 Oct 1;203:474-95.
- [9] Wang X, Zhou B, Jiang M. Dynamic contact angle effects on gas-liquid transport phenomena in proton exchange membrane fuel cell cathode with parallel design. *International Journal of Energy Research*. 2018.
- [10] Qin Y, Li X, Yin Y. Modeling of liquid water transport in a proton exchange membrane fuel cell gas flow channel with dynamic wettability. *International Journal of Energy Research*. 2018.
- [11] Šikalo Š, Marengo M, Tropea C, Ganić EN. Analysis of impact of droplets on horizontal surfaces. *Experimental Thermal and Fluid Science*. 2002 Jan 31;25(7):503-10.
- [12] Šikalo Š, Tropea C, Ganić EN. Impact of droplets onto inclined surfaces. *Journal of Colloid and Interface Science*. 2005 Jun 15;286(2):661-9.
- [13] Šikalo Š, Ganić EN. Phenomena of droplet–surface interactions. *Experimental Thermal and Fluid Science*. 2006 Nov 30;31(2):97-110.
- [14] Šikalo Š, Wilhelm HD, Roisman IV, Jakirlić S, Tropea C. Dynamic contact angle of spreading droplets: Experiments and simulations. *Physics of Fluids*. 2005 Jun;17(6):062103.
- [15] Šikalo Š. Analysis of droplet impact onto horizontal and inclined surfaces, Dissertation, TU Darmstadt, 2002.

- [16]Theodorakakos A, Ous T, Gavaises M, Nouri JM, Nikolopoulos N, Yanagihara H. Dynamics of water droplets detached from porous surfaces of relevance to PEM fuel cells. *Journal of Colloid and Interface Science*. 2006 Aug 15;300(2):673-87.
- [17]Fang C, Hidrovo C, Wang FM, Eaton J, Goodson K. 3-D numerical simulation of contact angle hysteresis for microscale two phase flow. *International Journal of Multiphase Flow*. 2008 Jul 31;34(7):690-705.
- [18]Jiang TS, Soo-Gun OH, Slattery JC. Correlation for dynamic contact angle. *Journal of Colloid and Interface Science*. 1979 Mar 15;69(1):74-7.
- [19]Tanner LH. The spreading of silicone oil drops on horizontal surfaces. *Journal of Physics D: Applied Physics*. 1979 Sep 14;12(9):1473.
- [20]Margarinos I, Nikolopoulos N, Marengo M, Antonini C, Gavaises M. VOF simulations of the contact angle dynamics during the drop spreading: Standard models and a new wetting force model. *Advances in Colloid and Interface Science*. 2014 Oct 1;212:1-20.
- [21]Jiang M, Zhou B, Wang X. Comparisons and validations of contact angle models. *International Journal of Hydrogen Energy*. 2018 Mar 22;43(12):6364-78.
- [22]Mukherjee S, Abraham J. Investigations of drop impact on dry walls with a lattice-Boltzmann model. *Journal of Colloid and Interface Science*. 2007 Aug 15;312(2):341-54.
- [23]Miller C. Liquid water dynamics in a model polymer electrolyte fuel cell flow channel, MSc Thesis, University of Victoria, 2009.
- [24]Wu TC. Two-phase flow in microchannels with application to PEM fuel cells, PhD Dissertation, University of Victoria, 2015.
- [25]Roisman IV, Opfer L, Tropea C, Raessi M, Mostaghimi J, Chandra S. Drop impact onto a dry surface: Role of the dynamic contact angle. *Colloids and Surfaces A: Physicochemical and Engineering Aspects*. 2008 Jun 5;322(1):183-91.
- [26]Jiang M, Zhou B. Numerical Study of Droplet Impact on Inclined Surface: Viscosity Effects. *ECS Transactions*. 2018 Jan 4;83(1):127-36.

- [27] R.E. Maples, Petroleum Refinery Process Economics (2nd ed.), Pennwell Books, ISBN 0-87814-779-9 (2000).
- [28] Zhmud B. Viscosity blending equations. The European lubricants industry magazine.–2014. 2014;93:1-4.

## CHAPTER 4

### IMPROVEMENT AND FURTHER INVESTIGATION ON HOFFMAN-FUNCTION-BASED DYNAMIC CONTACT ANGLE MODEL

#### 4.1. Introduction

Contact angle is referred to the angle formed at the gas-liquid-solid interactions (Figure 4.1), which is between the tangent planes of gas-liquid interface and the solid [1]. The value of the contact angle not only determines the shape of the gas-liquid interface, but also represents the fluid wettability. When the contact angle equals  $0^\circ$ , the solid surface can be perfectly wetted. When the contact angle equals  $180^\circ$ , then the solid surface is dry, i.e., perfectly non-wetted. When the contact angle is between  $0^\circ$  and  $90^\circ$ , the surface is hydrophilic, i.e., liquid tends to adhere to the surface (wetting liquid). When the contact angle is greater than  $90^\circ$ , the surface is hydrophobic, i.e., liquid tends to be repelled by the surface (non-wetting liquid).

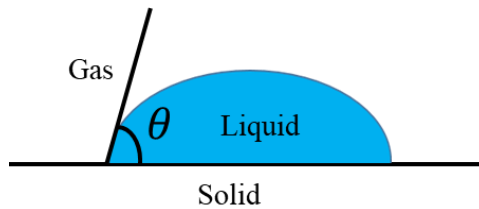


Figure 4.1: Contact angle at the interaction of gas, liquid and solid phases.

With respect to many practical problems involving two-phase flow (e.g., droplet spreading process on surfaces, gas-liquid behaviors and phenomena in microfluidic systems, etc.), the contact angle plays a critical role in the gas-liquid dynamics and the moving of contact line can make the contact angle deviate from its equilibrium value [2, 3]. Therefore, in the numerical modeling of two-phase problems, it is more reliable to use

the dynamic contact angle (DCA) as a boundary condition rather than the static contact angle (SCA).

Over the last decades, many dynamic contact angle models have been proposed and most of them considered the dynamic contact angle as a function of the contact line velocity [4-11]. More information of the available DCA models can be found in a recent comprehensive review by Malgarinos [12]. Recently, the Hoffman function, also known as Kistler's Law [6], has been used by many researchers to conduct DCA simulations [13-19] and it is one of the promising correlations to predict the DCA values. The basic form of Hoffman function is as follows:

$$f_{Hoff}(x) = \arccos \left\{ 1 - 2 \tanh \left[ 5.16 \left( \frac{x}{1 + 1.31x^{0.99}} \right)^{0.706} \right] \right\} \quad (4.1)$$

$$\theta_d = f_{Hoff} [Ca + f_{Hoff}^{-1}(\theta_s)] \quad (4.2)$$

where  $Ca$  is the capillary number and  $f_{Hoff}^{-1}(\theta_s)$  is the shift factor which is dependent only on the static contact angle. In the previous works of Miller [15] and Wu [16], the droplet behaviors on horizontal surface and in a gas channel were simulated using the volume of fluid (VOF) method. The Hoffman function was implemented by using a user defined function (UDF). However, these two works only considered the advancing dynamic contact angles by using the absolute value of contact line velocity in the DCA calculation (Equation (4.2)). In order to obtain the fundamental understanding of Hoffman function and build up a proper manner to implement this formula, Jiang et al. [20] created a DCA evolution map to better illustrate the DCA evolving mechanism in the simulation process. An Advancing-Receding DCA (AR-DCA) model was proposed which is able to predict

both advancing and receding dynamic contact angles. A series of numerical simulations for droplet impact on horizontal and inclined surfaces were conducted using the AR-DCA model and VOF method and the results had excellent agreement with the corresponding experiments from Sikalo et al. [21, 22], showing its superior capability in the simulation of droplet deformation and evolvement process.

However, it is found that there is an obvious limitation existed in the previous works [15, 16, 20] with respect to the evaluation of contact line velocity: all these works employed the VOF method to track the gas-liquid interface and the contact line velocity is obtained by projecting the flow velocity  $V_f$  to the direction of the VOF normal  $\vec{n}$ , as shown in Figure 4.2. This velocity is essentially the interface velocity  $V_i$  whereas the real contact line velocity  $V_{cl}$  should be parallel to the solid wall. Therefore, the evaluation strategy for the contact line velocity in the DCA model with VOF method needs to be further modified.

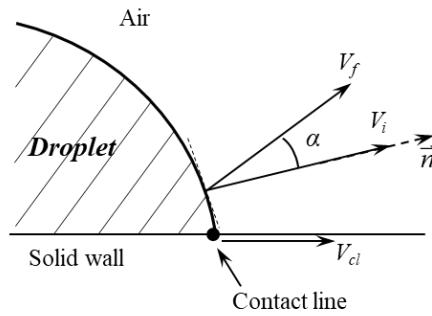


Figure 4.2: Evaluation of contact line velocity in the previous works [15, 16, 20].

In this study, we further modify the evaluation method of contact line velocity in the current AR-DCA model. The numerical simulations of droplet impact on inclined surface and liquid water behavior in a microchannel will be conducted to investigate the effects of this modified methodology on the simulation results.

## 4.2. Numerical Methodology

### 4.2.1. Governing Equations and Dynamic Contact Angle

In this study, the VOF method is employed to track the gas-liquid flow interface. Air is modeled as the gaseous phase and liquid water is modeled as the liquid phase, and these two phases are assumed to be immiscible. The numerical simulations are conducted using the commercial software package ANSYS Fluent. The governing equations for VOF method are the same as those employed in our previous work [20]. The dynamic contact angle  $\theta_d$  is calculated by the Hoffman function (Equation (4.1) and (4.2)) and the detailed description can be referred to Ref. [20].

### 4.2.2. Modification of the Evaluation Method of Contact Line Velocity

From Equation (4.2), it is known that the capillary number and the contact line velocity  $V_{cl}$  is required for the DCA calculation. For the AR-DCA model [20] and the previous models used in Ref. [15, 16], the contact line velocity evaluation process can be described as follows:

- 1) In the simulation process, the flow field velocity  $V_f$  in the vicinity of the boundary wall is obtained.
- 2) The interface velocity  $V_i$  is calculated by projecting the flow field velocity  $V_f$  to the direction of VOF unit normal vector  $\vec{n}$ , i.e.,  $V_i = V_f \cdot \vec{n}$ , as shown in Figure 4.2.
- 3) Then the interface velocity  $V_i$  is used as the contact line velocity in the DCA evaluation using Hoffman function.

In Hoffman's original experiments [23], the liquid moves in a glass tube with relatively small velocities (0.00008 to 0.06 cm/s as claimed in Ref. [23]) by the plunger and the

motion of advancing liquid-air interface was very stable, which makes the interface velocity can be approximately treated as the contact line velocity (i.e., the interface velocity is in the same direction of the liquid movement and parallel to the gas tube wall). However, for some other circumstances involving surrounding gas flow such as the liquid water transport in gas channels, the movement of gas-liquid interface is not a stable process and the direction is not always parallel to the solid wall. When it comes to the numerical modeling and simulation, the direction of the gas-liquid interface is reflected by the VOF normal and it is not reliable to consider the interface velocity as the contact line velocity even in the vicinity area.

Therefore, in this study, we proposed an approach to improve the current evaluation method of the contact line velocity as illustrated in Figure 4.3(b), where  $\vec{n}_w$  and  $\vec{t}_w$  are the surface unit vectors normal and tangential to the wall respectively. In order to get the contact line velocity, the interface velocity should be projected to the direction of  $\vec{t}_w$ . If the angle between  $\vec{n}_w$  and  $\vec{n}$  is  $\beta$ , then the contact line velocity will become  $V_{cl} = V_i \cdot \sin \beta$ . Therefore, with the surface unit normal vector  $\vec{n}_w$  and the VOF unit vector  $\vec{n}$ , the angle  $\beta$  can be determined as:

$$\beta = \arccos(\vec{n} \cdot \vec{n}_w) \quad (4.3)$$

With the flow field velocity  $V_f$  extracted from the computational cells in the contact line area, the contact line velocity can be expressed as:

$$V_{cl} = V_f \cdot \vec{n} \cdot \sin \beta = V_f \cdot \vec{n} \cdot \sin(\arccos(\vec{n} \cdot \vec{n}_w)) \quad (4.4)$$



This modified evaluation method of contact line velocity will be implemented into the AR-DCA model and hereafter we name it as improved-AR-DCA (i-AR-DCA) model.

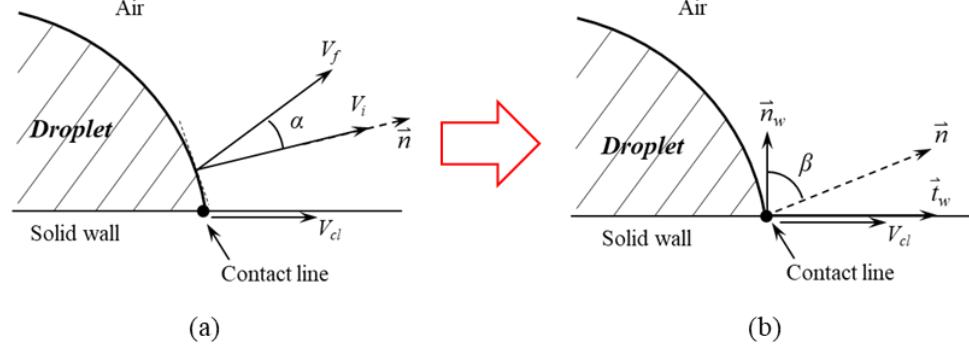


Figure 4.3: Schematic of contact line velocity evaluation in AR-DCA model (a) and modification (b).

### 4.3. Numerical Model Description

#### 4.3.1. Computational Domain and Boundary Conditions

The numerical simulation in the present study is conducted based on two different cases to investigate the effects of the modified strategy of the contact line velocity evaluation. The first case is for the droplet impact on inclined surface and a cylinder computational domain is used as shown in Figure 4.4(a), which is the same as employed in our previous study [20]. The Case 3 and 4 in Ref. [20] (i.e., water droplet impact on  $10^\circ$  smooth glass and wax) are selected for the simulation in this study. More detailed information can be found in Ref. [20] including the dimension of the computational domain, liquid property, surface wettability, droplet impact velocity, etc. Another case is for the liquid water behaviors in a microchannel and the schematic of the computational domain is shown in Figure 4.4(b). The channel has the dimension of 0.05 mm in depth, 0.5 mm in height and 5 mm in length, which is similar to the experimental set up from Hidrovo et al. [24]. The liquid water inlet is a 0.02 mm rectangular slot located on the bottom wall and 1.65 mm

away from the air inlet boundary. In the numerical simulation, the no-slip boundary condition is applied at channel walls. The DCA is applied on both side walls and bottom wall and the initial contact angle (i.e., SCA) is  $108^\circ$  which is the same as the hydrophobic channel used in the experiments [24]. In the numerical simulation, the time step is set as  $1 \times 10^{-6}$  s for the cases of droplet impact on inclined surface and  $1 \times 10^{-7}$  s for the microchannel case.

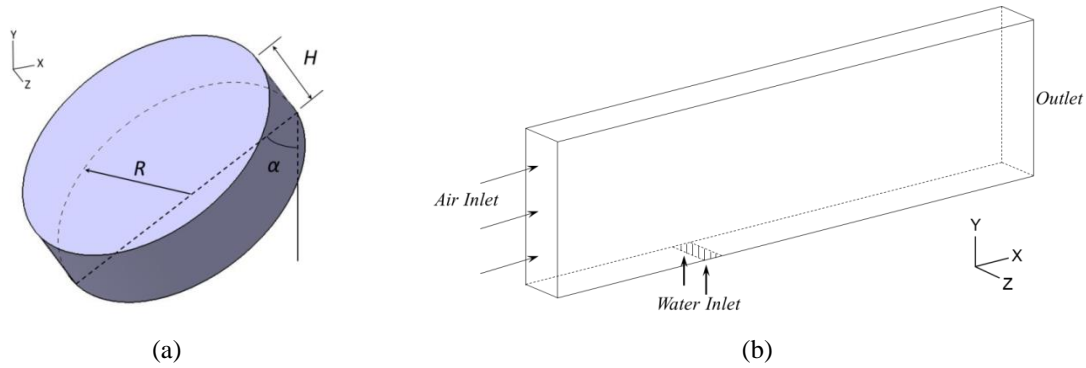


Figure 4.4: Schematic of computational domains used in the present study: (a) droplet impact on inclined surface; (b) liquid water behaviors in a single straight microchannel.

#### 4.3.2. Grid Independency

The grid independency check for the case of droplet impact on inclined surface has been conducted and reported in the Section 2.4.3 of Chapter 2 in this thesis. In this chapter, the grid independency for the microchannel case is further conducted by comparing four sets of mesh with different number of nodes in the channel cross-section and along the channel length. The detailed information for each of these meshes is listed in Table 4.1.

The liquid water behaviors in microchannel are simulated and compared based on these four meshes with the air inlet velocity  $V_{\text{air}} = 7.9$  m/s and water inlet flow rate  $Q_{\text{water}} = 10$   $\mu\text{L}/\text{min}$  using the original AR-DCA model. Reynolds number  $Re$  and Capillary number  $Ca$  are used to evaluate the air and water inlet flow rate respectively where  $Re = 49.2$  and

$Ca = 0.0023$ . The numerical results are shown in Table 4.2 for the liquid water evolvment in microchannel in terms of dimensionless time  $t_a$  ( $t_a = t V_{\text{air}}/L_c$ , where  $t$  is the simulation time from liquid water emergence and  $L_c$  is the length of the microchannel). It can be observed that with the increase of the computational nodes (from Resolution A to D), the water slug height is also slightly increased. Also, under the relatively coarse meshes (Resolution A and B), the liquid water detachment occurs earlier than that of the refined meshes (Resolution C and D). Figure 4.6 shows the comparison of the ratio of slug length to height ( $l/h$ ) versus  $t_a$  under different grid resolutions (a schematic view of the liquid water slug in microchannel is shown in Figure 4.5). It is further indicated that increase of the nodes leads to the decrease of  $l/h$  and there is no significant difference between the Resolution C and D. Considering both the computational cost and numerical accuracy, the grid type C is adopted for the simulation.

**Table 4.1: Information of Different Grid Resolutions for Microchannel Domain**

Grid resolution type	Number of nodes in the channel cross-section	Number of nodes along channel length	Total number of nodes
A	42×5	420	87,780
B	51×6	505	153,918
C	63×7	629	276,507
D	84×9	837	631,260

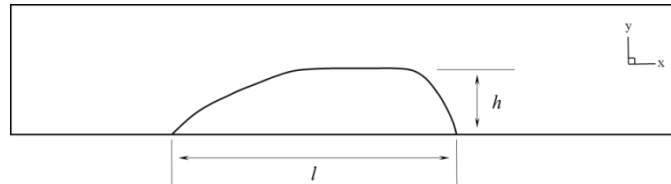




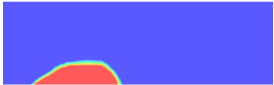
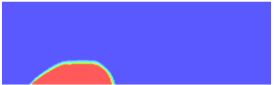


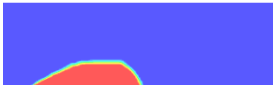
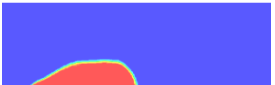
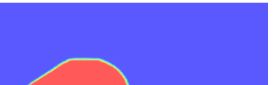
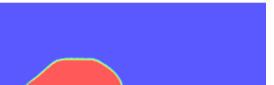
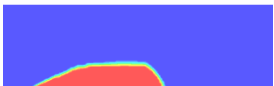
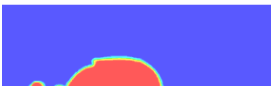
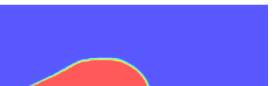
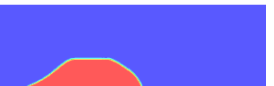
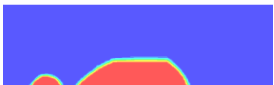
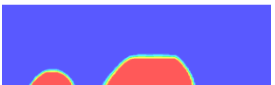
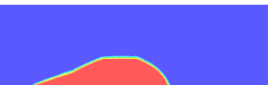
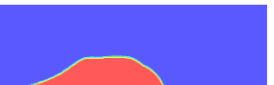


Figure 4.5: Schematic of a liquid water slug in microchannel with the length  $l$  and height  $h$ .

**Table 4.2: Comparison of Numerical Results under Different Grid Resolutions ( $Re = 49.2$ ,  $Ca = 0.0023$ )**

$t_a$	Resolution A	Resolution B	Resolution C	Resolution D
15.8				
23.7				
31.6				
39.5				
47.4				

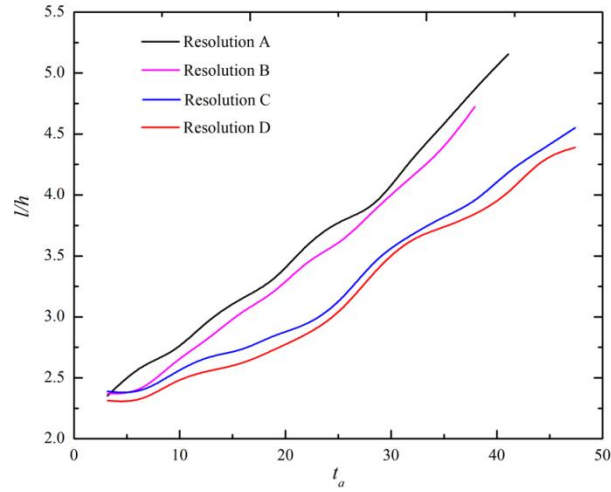


Figure 4.6: Comparison of the ratio of water slug length to height ( $l/h$ ) under different grid resolution.

## 4.4. Results and Discussion

### 4.4.1. Droplet Impact on Inclined Surface

Figure 4.7 and 4.8 show the comparison of the numerical results for the droplet impact on smooth glass and wax respectively based on AR-DCA and i-AR-DCA models. It can be observed from the qualitative results that the general droplet spreading and deformation

exhibit no significant difference between the AR-DCA and i-AR-DCA models, for both the water-smooth glass and water-wax systems. This is because for the cases of droplet impact on surface, there is no surrounding gas flow and the droplet spreading and sliding process is dominated by the inertial force (induced by the gravitational force when the droplet falls down), leading to a stable process for the interface motion. Also, by comparing the spreading factor  $x/D$  at the leading and trailing side ( $x_{\text{leading}}/D$  and  $x_{\text{trailing}}/D$ ) versus the dimensionless time  $t^*$  ( $t^* = t V_p/D$  [20, 21], where  $t$  is the time from impact) as shown in Figure 4.9, it is noted that for the both cases, the evolvement of the spreading factor at leading and trailing edges are almost identical between the AR-DCA and i-AR-DCA models and share the same evolution trend, which further indicates that the droplet spreading and deformation process has less dependence on the modification of the contact line velocity evaluation.

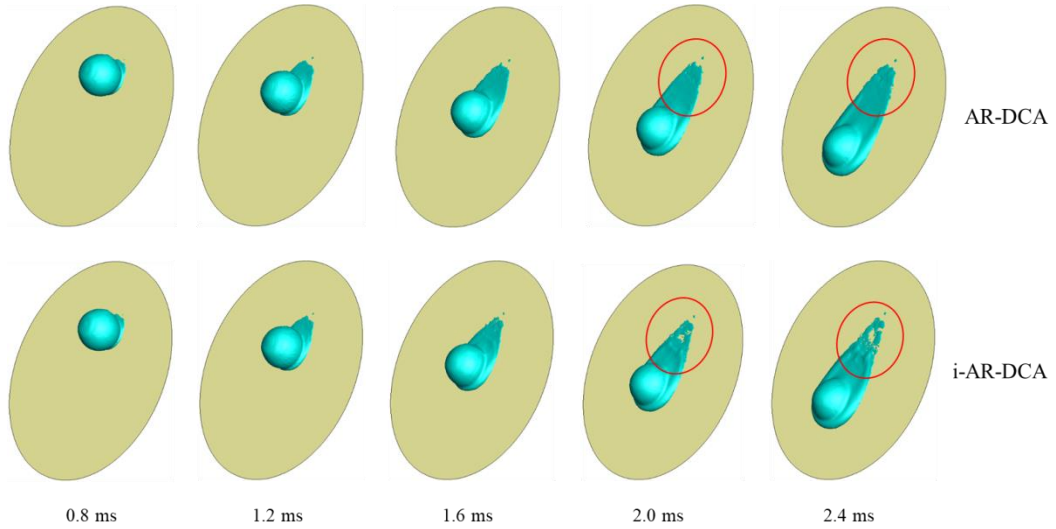


Figure 4.7: Comparison of numerical results for water droplet impact on wax (Case 3 in Ref. [20]) from AR-DCA and i-AR-DCA models.

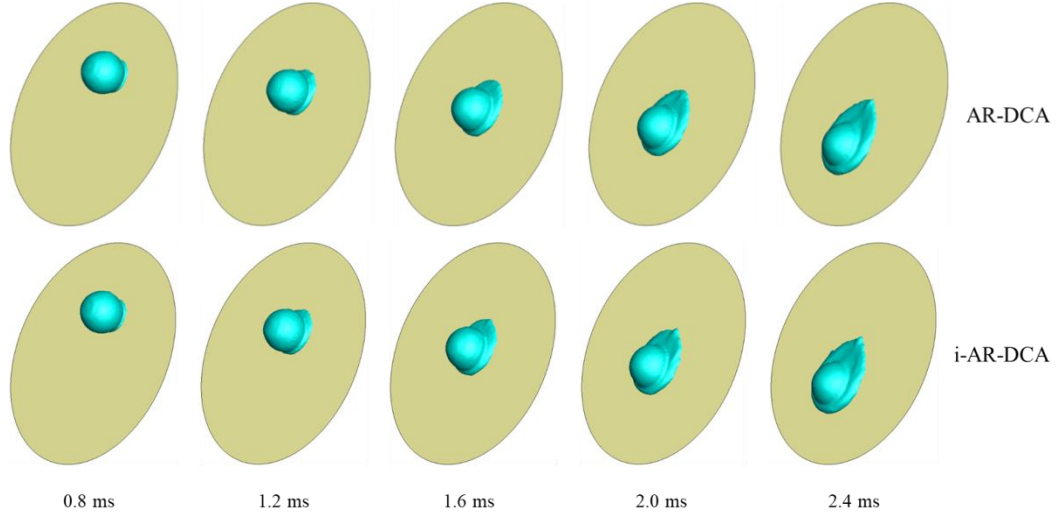


Figure 4.8: Comparison of numerical results for water droplet impact on wax (Case 4 in Ref. [20]) from AR-DCA and i-AR-DCA models.

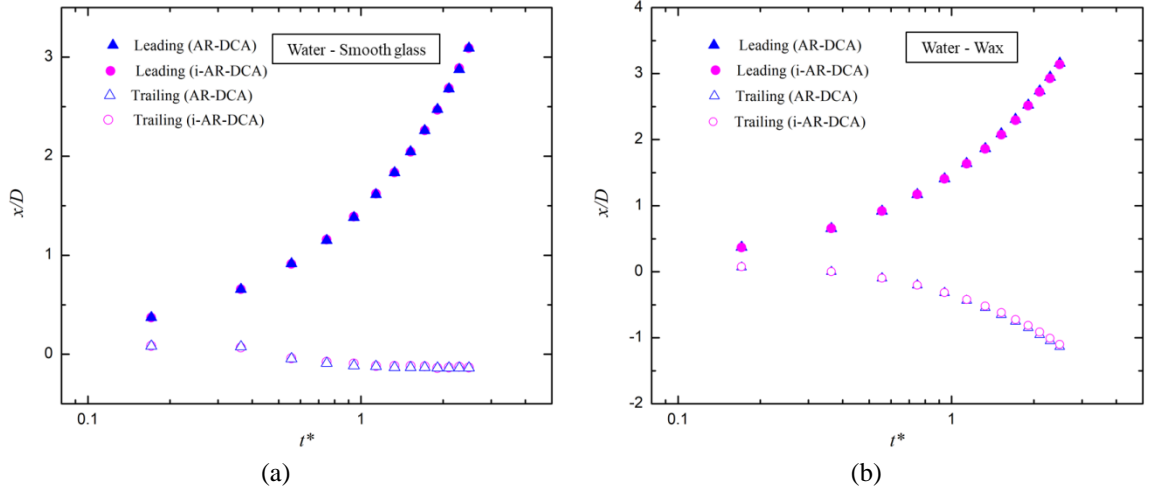


Figure 4.9: Comparison of the spreading factor  $x/D$  from AR-DCA and i-AR-DCA models: (a) water droplet impact on smooth glass (Case 3 in Ref. [20]); (b) water droplet impact on wax (Case 4 in Ref. [20]).

However, the effects from the i-AR-DCA model can also be reflected in the following aspects. From the phenomenological observation in Figure 4.7, it is noted that due to the high wettability of the surface ( $\text{SCA} = 8^\circ$ ), the trailing edge of the droplet remains fixed on the surface when the droplet slides down, forming the liquid film at the droplet tail. However, for the last two droplet profiles ( $t = 2.0$  ms and 2.4 ms), the liquid film from

the i-AR-DCA model tends to recoil more from the surface and makes the film broken compared to the results from the AR-DCA model. This is because on the trailing side, most interface velocity  $V_i$  is negative. By projecting the interface velocity to the contact line direction, the contact line velocity will have a smaller negative value than the interface velocity ( $V_{cl} = V_i \cdot \sin \beta$  and  $|V_{cl}| < |V_i|$ ), which makes the receding dynamic contact angles in the i-AR-DCA model larger than those from the AR-DCA models. Therefore, the liquid film at the trailing side from the i-AR-DCA model is easier to repel from the surface. Also, by comparing the contact angle values at the leading and trailing edges (as shown in Figure 4.10), it is found that for both water droplet impact on smooth glass and wax, the contact angles at the leading edge (mainly advancing dynamic contact angles) from i-AR-DCA model are lower than those of the original AR-DCA model under same  $t^*$ ; whereas for the trailing edges, approximately all the contact angles from i-AR-DCA model are higher than those of the AR-DCA model under same  $t^*$  (mainly receding dynamic contact angles), which further illustrates the distinctions between the AR-DCA and i-AR-DCA model.

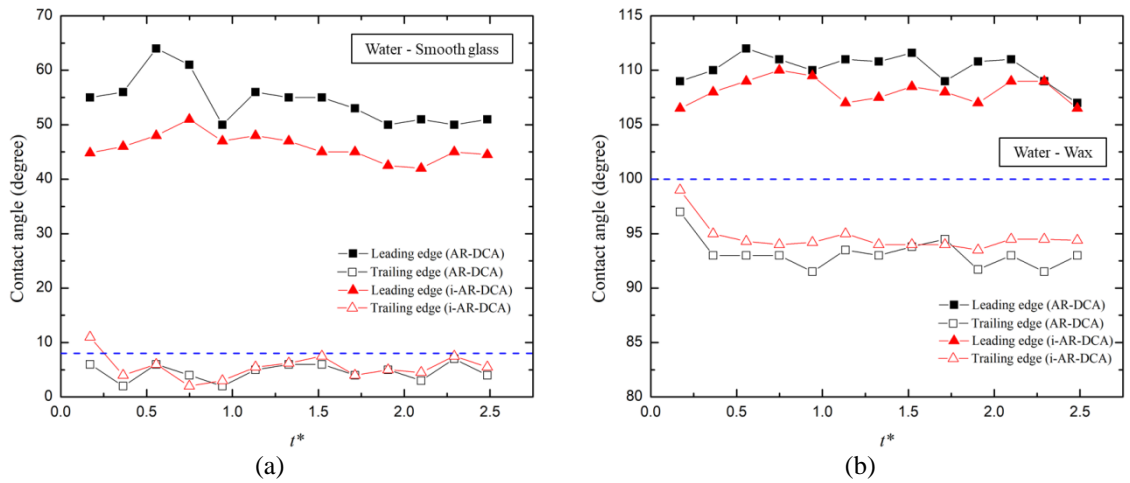


Figure 4.10: Comparison of contact angles at the leading and trailing edges from AR-DCA and i-AR-DCA models: (a) water droplet impact on smooth glass (Case 3 in Ref. [20]); (b) water droplet impact on wax (Case 4 in Ref. [20]).

#### 4.4.2. Liquid Water Behaviors in a Single Straight Microchannel

Figure 4.11 shows the comparison of the liquid water evolvement process in a microchannel at selected dimensionless time  $t_a$  from the AR-DCA and i-AR-DCA models. The air inlet velocity ( $V_{\text{air}}$ ) is 10.7 m/s ( $Re = 66.6$ ), which is equivalent to the mass flow rate of  $3.28 \times 10^{-7}$  kg/s. The water inlet volume flow rate ( $Q_{\text{water}}$ ) is 10  $\mu\text{L}/\text{min}$  ( $Ca = 0.0023$ ), which is equivalent to the velocity of 0.167 m/s and mass flow rate of  $1.66 \times 10^{-7}$  kg/s. From the qualitative comparison, it is noted that the general water slug evolvement and deformation from these two models are very the similar: at first, the liquid water enters into the channel and form the water slug with time; meanwhile, the slug height and length continuously grow under the constant water volume flow rate; with time, the slug partially blocks the microchannel and induces the detachment because the wall adhesion force is not able to balance the drag force by the air flow [25]. Also, the ratio of slug length to height ( $l/h$ ) is presented to evaluate the slug deformation in the process, as shown in Figure 4.12, and the results show that the evolution of  $l/h$  has a good agreement between these two models before detachment. However, it is noticed that the slug detachment from the i-AR-DCA model occurs at about  $t_a = 33.2$ , which is earlier than that of the AR-DCA model ( $t_a = 45.7$ ). This is because, for the i-AR-DCA model, the receding dynamic contact angles (mainly located at the liquid inlet area before detachment) are larger than those from the AR-DCA model as discussed above. The previous works from Zhu et al. [26] and Andersson et al. [27] indicated that higher contact angle will lead to earlier droplet detachment mainly due to the decreased area of liquid–solid interface. Unlike the previous cases such as liquid moving in a glass tube (Hoffman’s experiments [23]) or droplet spreading on surfaces, the evolvement of liquid



water in microchannel is not a stable process with surrounding air flow exerted on the gas-liquid interface. Therefore, it is very critical to implement the real contact line velocity in the numerical model and the results indicate that the i-AR-DCA model can lead to early liquid water detachment compared to the previous AR-DCA model.

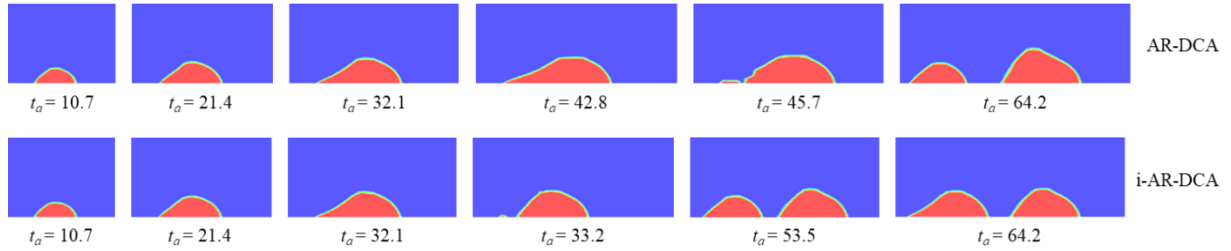


Figure 4.11: Comparison of liquid water evolution process based on AR-DCA and i-AR-DCA models ( $Re = 66.6$ ,  $Ca = 0.0023$ ).

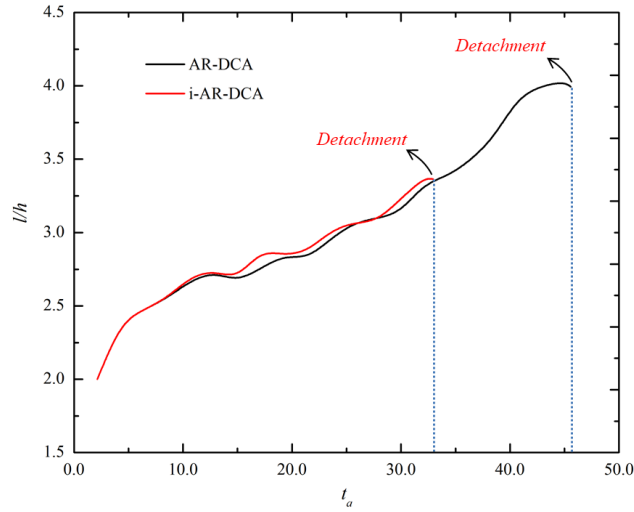


Figure 4.12: Comparison of the ratio of water slug length to height ( $l/h$ ) before detachment under AR-DCA and i-AR-DCA models.

#### 4.5. Conclusions

This study introduces a modification strategy for the contact line velocity evaluation method in the original AR-DCA model and an i-AR-DCA model is proposed, in order to reflect the real contact line treatment. The simulations of droplet impact on inclined

surface and liquid water behaviors in a microchannel are conducted using VOF method with the AR-DCA and i-AR-DCA models to investigate the effects of the modification strategy. It is indicated that the modified methodology can lead to the increase of receding dynamic contact angle and decrease of advancing dynamic contact angle, which makes the liquid film repel from the surface more easily and form small droplets at the trailing edge for the case of the water droplet impact on smooth glass; also, it is noticed there is no significant difference for the droplet general spreading and deformation process between the AR-DCA and i-AR-DCA models. For the case of liquid water evolvment in the microchannel, the i-AR-DCA model can facilitate the liquid water detachment, indicating the importance for the implementation of real contact line velocity evaluation in the DCA models under complex surrounding gas flow.

In the future, the validation experiments should be conducted for the i-AR-DCA model in order to further apply it to the simulation of gas-liquid phenomena in PEMFCs.

## References

- [1] Blake TD. Dynamic contact angles and wetting kinetics. *Wettability*. 1993;251.
- [2] Šikalo Š, Tropea C, Ganić EN. Dynamic wetting angle of a spreading droplet. *Experimental Thermal and Fluid Science*. 2005 Aug 1;29(7):795-802.
- [3] Blake TD. The physics of moving wetting lines. *Journal of Colloid and Interface Science*. 2006 Jul 1;299(1):1-3.
- [4] Tanner LH. The spreading of silicone oil drops on horizontal surfaces. *Journal of Physics D: Applied Physics*. 1979 Sep 14;12(9):1473.
- [5] Cox RG. The dynamics of the spreading of liquids on a solid surface. Part 1. Viscous flow. *Journal of Fluid Mechanics*. 1986 Jul;168:169-94.

- [6] Kistler SF. Hydrodynamics of wetting. *Wettability*. 1993;6:311-430.
- [7] Jiang TS, Soo-Gun OH, Slattery JC. Correlation for dynamic contact angle. *Journal of Colloid and Interface Science*. 1979 Mar 15;69(1):74-7.
- [8] Bracke M, De Voeght F, Joos P. The kinetics of wetting: the dynamic contact angle. *Trends in Colloid and Interface Science III* 1989 (pp. 142-149).
- [9] Seebergh JE, Berg JC. Dynamic wetting in the low capillary number regime. *Chemical Engineering Science*. 1992 Dec 1;47(17-18):4455-64.
- [10] Yu D, Choi C, Kim MH. Pressure drop and dynamic contact angle of triple-line motion in a hydrophobic microchannel. *Experimental Thermal and Fluid Science*. 2012 May 31;39:60-70.
- [11] Yokoi K, Vadillo D, Hinch J, Hutchings I. Numerical studies of the influence of the dynamic contact angle on a droplet impacting on a dry surface. *Physics of Fluids*. 2009 Jul;21(7):072102.
- [12] Malgarinos I, Nikolopoulos N, Marengo M, Antonini C, Gavaises M. VOF simulations of the contact angle dynamics during the drop spreading: standard models and a new wetting force model. *Advances in Colloid and Interface Science*. 2014 Oct 31;212:1-20.
- [13] Šikalo Š, Wilhelm HD, Roisman IV, Jakirlić S, Tropea C. Dynamic contact angle of spreading droplets: Experiments and simulations. *Physics of Fluids*. 2005 Jun;17(6):062103.
- [14] Mukherjee S, Abraham J. Investigations of drop impact on dry walls with a lattice-Boltzmann model. *Journal of Colloid and Interface Science*. 2007 Aug 15;312(2):341-54.
- [15] Miller C. Liquid water dynamics in a model polymer electrolyte fuel cell flow channel, MASC Thesis, University of Victoria, 2009.
- [16] Wu TC. Two-Phase Flow in Microchannels with Application to PEM Fuel Cells, PhD dissertation, University of Victoria, 2015.

- [17]Roisman IV, Opfer L, Tropea C, Raessi M, Mostaghimi J, Chandra S. Drop impact onto a dry surface: Role of the dynamic contact angle. *Colloids and Surfaces A: Physicochemical and Engineering Aspects*. 2008 Jun 5;322(1):183-91.
- [18]Jiang M, Zhou B, Droplet Behaviors on Inclined Surfaces with Dynamic Contact Angle. Submitted to *International Journal of Multiphase Flow*. 2018.
- [19]Wang X, Zhou B, Jiang M. Dynamic Contact Angle Effects on Gas-liquid Transport Phenomena in Proton Exchange Membrane Fuel Cell cathode with Parallel Design. *International Journal of Energy Research*. 2018.
- [20]Jiang M, Zhou B, Wang X. Comparisons and validations of contact angle models. *International Journal of Hydrogen Energy*. 2018 Mar 22;43(12):6364-78.
- [21]Šikalo Š, Tropea C, Ganić EN. Impact of droplets onto inclined surfaces. *Journal of Colloid and Interface Science*. 2005 Jun 15;286(2):661-9.
- [22]Šikalo Š, Ganić EN. Phenomena of droplet–surface interactions. *Experimental Thermal and Fluid Science*. 2006 Nov 30;31(2):97-110.
- [23]Hoffman RL. A study of the advancing interface. I. Interface shape in liquid—gas systems. *Journal of Colloid and Interface Science*. 1975 Feb 1;50(2):228-41.
- [24]Hidrovo CH, Wang FM, Lee ES, Vigneron S, Steinbrenner JE, Paidipati JV, Kramer TA, Eaton JK, Goodson KE. Experimental investigation and visualization of two-phase flow and water transport in microchannels. In *ASME 2004 International Mechanical Engineering Congress and Exposition 2004 Jan 1* (pp. 205-212). American Society of Mechanical Engineers.
- [25]Cho SC, Wang Y, Chen KS. Droplet dynamics in a polymer electrolyte fuel cell gas flow channel: Forces, deformation, and detachment. I: Theoretical and numerical analyses. *Journal of Power Sources*. 2012 May 15;206:119-28.
- [26]Zhu X, Sui PC, Djilali N. Three-dimensional numerical simulations of water droplet dynamics in a PEMFC gas channel. *Journal of Power Sources*. 2008 Jun 15;181(1):101-15.

- [27] Andersson M, Mularczyk A, Lamibrac A, Beale SB, Eller J, Lehnert W, Büchi FN. Modeling and synchrotron imaging of droplet detachment in gas channels of polymer electrolyte fuel cells. *Journal of Power Sources*. 2018 Nov 15;404:159-71.

## CHAPTER 5

### NUMERICAL STUDY OF FLOW REGIMES IN MICROCHANNEL WITH DYNAMIC CONTACT ANGLE

#### 5.1. Introduction

In recent decades, proton exchange membrane fuel cell (PEMFC) has received extensive attention due to its remarkable features such as high power density, quick start-up, low operating temperature and quietness. However, liquid water management is still a very critical issue in the PEMFC development. On one hand, too much liquid water will cause the water flooding and hinder the oxygen transport, resulting in the poor performance of PEMFC; on the other hand, too little liquid water will cause the membrane dehydration and lead to the degradation of PEMFC performance [1]. Therefore, a proper balance should be maintained between membrane humidification and liquid water flooding in order to achieve the optimization of fuel cell performance.

Numerical modeling and simulation based on computational fluid dynamics (CFD) are promising approaches to obtain the actual liquid water behaviors in PEMFCs, especially in gas flow channels [2], which help conquer the difficulties in performing experiments. Among the available numerical models, the volume of fluid (VOF) method has the advantage of tracking and locating the gas-liquid interface, making it the most popular approach in the simulation of two-phase flow in PEMFCs. Since the first study by Quan et al. [3], numerous works have been reported for water management simulations in PEMFCs and a recent comprehensive review for these works was conducted by Ferreira et al. [2]. However, among the available literature, it is found that the static contact angle (SCA) is generally used as wall boundary condition while very limited amount of works

consider dynamic contact angle (DCA) for two-phase flow simulation in PEMFC with complex flow field. Recently, for the first time, Wang et al. employed both DCA and SCA models to study the liquid water behavior and transport inside a PEMFC cathode with parallel flow design [4] and a stirred tank reactor (STR) design [5]. It was indicated that the liquid water distribution and transport process from the DCA model are significantly different compared to those from the SCA model, showing the remarkable DCA effects on the simulation results. However, the comparison to the experimental results is still needed to further validate the DCA model in PEMFC-related simulations.

Recently, it has been noted that dynamic contact angle plays a critical role in the prediction of gas-liquid behaviors and the results from the DCA model are more reasonable compared to the SCA model [6, 7]. However, most DCA-related works focus on the two-phase flow with simple geometries such as droplet impact on horizontal or inclined surfaces [6-14]. A more reliable DCA model is still needed to be developed in order to well simulate gas-liquid behaviors and flow regimes in more complex flow field [4, 5, 15]. The gas-liquid two-phase flow problems in PEMFC gas channels can be classified as a typical “water-in-air” system in a microchannel, where the air is considered as the continuous phase and the liquid water is considered as the disperse phase in microchannel. Over the last decades, many researchers have made efforts to understand gas-liquid flow patterns and regimes in microchannels, using both experimental and numerical methods. Hidrovo et al. [16] conducted visualization studies on two-phase flow in a U-shaped microchannel with hydrophilic and hydrophobic conditions. It was found that the channel surface wettability and air/water inlet flow rate have significant effects on the flow structure: for the hydrophilic channel, the liquid water

will flood the channel under low pressure drop while the thin film (or stratified flow) is observed under high pressure drop conditions; whereas for the hydrophobic channel, the liquid water “blobs” (namely the slug flow) are formed at low air flow rate and can induce the blockage to the air flow. Hidrovo et al. [17] also studied water slug formation and detachment with air flow in the hydrophobic microchannel. The experiments were conducted under varied air inlet velocity based on two samples with different widths of water injection side slot. It was indicated that for low Reynolds number ( $Re < 200$ ), the pressure gradient drag force significantly affect the water slug detachment while the inertial drag is mainly responsible for the detachment. Carroll et al. [18] investigated water droplet detachment process in a T-junction microchannel with different aspect ratios. The experimental tests were conducted within a range of air Reynold number ( $10 < Re < 200$ ) to examine the effects of relevant forces (inertial, viscous and hydrodynamic pressure forces) on the droplet detachment. It was noted that, when the Reynolds number is increased, the droplet shape at detachment transforms from the elongated slug to the droplet with nearly uniform aspect ratio. The authors also found that the dominant detachment mechanism is turned from the hydrostatic pressure difference to the inertial drag when  $Re$  is increased to 100. Wu et al. [19] conducted flow visualization to investigate the water droplet dynamics in a single straight microchannel under different air and water flow rates. Three typical flow regimes were categorized from the experimental observation: 1) slug flow, when the air flow rate is low and the drag force has minor effect on the droplet deformation; 2) droplet flow, when the air flow velocity is increased and the evolution of droplet emergence, growth and detachment can be observed; 3) film flow, when the air superficial velocity is further increased and the drag



force plays a dominant role in the droplet formation. It was also indicated that the higher contact angle hysteresis can improve the stability of water droplet and increase its capability to withstand the drag force. Cho et al. [20] theoretically studied the water droplet dynamics in a single channel by analyzing the forces exerted on the droplet, the forces causing the droplet deformation and the forces on droplet detachment. The numerical tests were conducted based on different droplet sizes and locations (in the fully developed region or the entrance region) to examine the relation between drag forces (viscous and pressure) and air velocity. The results showed that the viscous plays a major role for small droplets whereas the pressure drag is dominant for large droplets. Also, more drag is exerted on small droplets in the entrance region and on larger droplets in the fully developed region. In the sequel paper [21], the authors extended this study by conducting both the experiment and VOF simulation on the droplet deformation and detachment. The numerical and experimental results were compared to the analytical solutions presented in Ref. [20] and a good agreement was achieved. Andersson et al. [22] performed both experiment and VOF simulation to study air-water two-phase behavior in the gas channel with GDL surface. It was noted that the two-phase flow in the microchannel is affected by a series of parameters including the liquid inlet area, the channel height, air flow velocity and the contact angle. The small liquid inlet size and increased gas velocity can lead to smaller droplets. Also, higher GDL contact angle results in earlier droplet detachment (i.e., smaller droplet size), which was also confirmed in the previous study by Zhu et al. [23]. A recent study by Mastiani et al. [24] presented different flow regimes under various air Reynolds numbers ( $Re$ ) and liquid water Capillary numbers ( $Ca$ ) in a T-junction microchannel, including squeezing and dripping

flow (low  $Ca$  and  $Re$ ), unstable dripping flow (low  $Ca$  and high  $Re$ ), jetting flow (middle  $Ca$  and a wide range of  $Re$ ) and unstable jetting flow (high  $Ca$  and  $Re$ ). It was also found that the increase of contact angle can result in the decrease of droplet detachment time and the droplet size is affected by both the  $Ca$  and  $Re$  numbers.

From the available literature, it is known that many studies have been reported for water flow behaviors in microchannels using experimental or numerical approaches. However, the simulation work considering the three-dimensional, dynamic contact angle model is very limited. Therefore, in this study, we aim to further apply the DCA model to simulate the gas-liquid behaviors and flow regimes in a single straight microchannel under various water and air inlet flow rates.

## **5.2. Numerical Model Description**

### **5.2.1. Computational Domain and Boundary Conditions**

As shown in Figure 5.1, a three-dimensional single straight channel with rectangular cross section is built up as the computational domain. The dimensions of the channel are 0.05 mm in depth, 0.5 mm in height and 5 mm in length. The geometry is similar to the experimental set up from Hidrovo et al. [16] by simplify the U-shaped channel to the straight channel. The liquid water enters into the channel through a 0.02 mm rectangular slot on the bottom wall, which is located at 1.65 mm away from the air inlet boundary. In the numerical simulation, the no-slip boundary condition is applied at channel walls. The DCA is considered on both side wall and bottom wall and the initial contact angle (i.e., SCA) is set as  $108^\circ$  which is the same as the hydrophobic channel used in the experiments [16]. Different air inlet velocities ( $V_{\text{air}}$ ) and water inlet volume flow rate ( $Q_{\text{water}}$ ) are considered in this study and converted to mass flow rate (kg/s) as the air and

water inlet boundary condition in the simulation. Reynolds number  $Re$  and Capillary number  $Ca$  are used to evaluate the air and water inlet flow rate respectively.

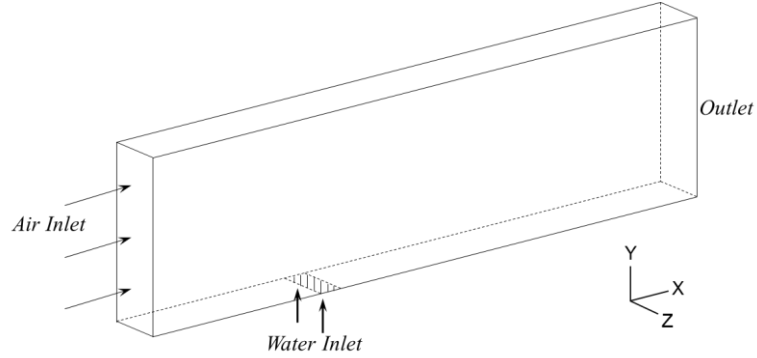


Figure 5.1: Schematic of computational domain for microchannel.

### 5.2.2. Governing Equations and Dynamic Contact Angle

In this study, the VOF method is employed to track the gas-liquid flow interface. Air is modeled as the gaseous phase and liquid water is modeled as the liquid phase, and these two phases are assumed to be immiscible. The governing equations for VOF method are the same as those employed in our previous work [13] and the detailed description can be found in Ref. [13].

The dynamic contact angle  $\theta_d$  is calculated by the Hoffman function:

$$f_{Hoff}(x) = \arccos \left\{ 1 - 2 \tanh \left[ 5.16 \left( \frac{x}{1 + 1.31x^{0.99}} \right)^{0.706} \right] \right\} \quad (5.1)$$

and  $\theta_d$  is described by the following formula:

$$\theta_d = f_{Hoff} [Ca + f_{Hoff}^{-1}(\theta_s)] \quad (5.2)$$

where the shift factor,  $f_{Hoff}^{-1}(\theta_s)$ , is obtained from the inverse of the Hoffman function under SCA. In the previous study [13], using a DCA evolution map, we have clarified a

proper manner to implement Hoffman function in the DCA model to consider both advancing and receding dynamic contact angles. Also, in the previous chapter in this thesis, we further modified the evaluation method of contact line velocity in the AR-DCA model [13] and proposed an i-AR-DCA model. In this study, the i-AR-DCA model is employed to simulate the liquid water behaviors and flow regimes in the microchannel. The time step is set as  $1 \times 10^{-7}$  s for the cases under relatively lower  $Re$  (29.9, 66.6) and  $5 \times 10^{-8}$  s for the cases under higher  $Re$  (112.7).

### 5.2.3. Grid Independency

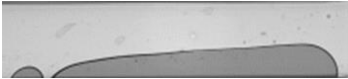
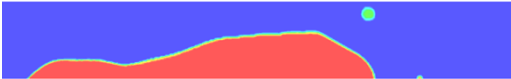

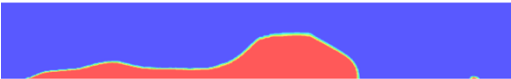


The computational domain has a total of 276507 nodes and the number of nodes along the X, Y and Z direction is 629, 63 and 7 respectively. The grid independency check has been conducted in the previous chapter and more details can be referred to the Section 4.3.2 in this thesis.

## 5.3. Results and Discussion

Hidrovo et al. [16] performed experimental visualization on the liquid water behavior and transport in a hydrophobic microchannel. Table 5.1 shows the comparison of the liquid water flow pattern between the experimental and numerical results. The air inlet velocity  $V_{\text{air}}$  is set as 4.8 m/s, 10.7 m/s, 18.1 m/s ( $Re = 29.9, 66.6$  and  $112.7$ ) and the water injection rate is  $50 \mu\text{L}/\text{min}$  ( $Ca = 0.011$ ) for both the experiment and simulation. It can be seen that in the experiment, the liquid water forms the slug flow under relatively low air inlet velocity (4.8 m/s and 10.7 m/s) and water blob with liquid film under higher air inlet velocity (18.1 m/s). However, the liquid water flow pattern captured in the simulation is difficult to fit well with the corresponding experimental results. Using the same air and

water flow rates provided in the experiment, the liquid water tends to form the jetting flow regime that continuously attaches to the water inlet without detachment. The work of Hidrovo et al. [16] only provides one single image for each of the flow conditions without time instant and the liquid water evolvement process is not able to be tracked. Therefore, in this study, we will further conduct numerical simulations to investigate the flow regimes under various air and water flow rates.

**Table 5.1: Comparison of Liquid Water Behavior between the Numerical Simulation and Experimental Visualization [16] under  $Ca = 0.011$**

$Re$	Expeimental visualization [16]	Numerical results
29.9		
66.6		
112.7		

### 5.3.1. Liquid Water Behaviors under Different Water Inlet Flow Rates

In the first section, the liquid water behaviors and flow regimes in the microchannel under various water inlet flow rates are investigated and discussed. The water inlet volume flow rate  $Q_{\text{water}}$  is ranged from  $5 \mu\text{L}/\text{min}$  to  $50 \mu\text{L}/\text{min}$  (corresponding to  $Ca$  0.0011 to 0.011) under the fixed air inlet velocity of  $10.7 \text{ m/s}$  ( $Re = 66.6$ ). Detailed information and parameters are listed in Table 5.2. For the cases under different water inlet flow rates and same air inlet velocity, a dimensionless time  $t_a$  is used to present the liquid water evolvement process in the microchannel ( $t_a = t V_{\text{air}}/L_c$ , where  $t$  is the simulation time from liquid water emergence and  $L_c$  is the length of the microchannel).

**Table 5.2: Simulation Cases under Various Water Inlet Flow Rates with Fixed Air  $Re$  66.6**

Case #	Air inlet velocity $V_{\text{air}}$ (m/s)	Air inlet $Re$	Water inlet volume flow rate $Q_{\text{water}}$ ( $\mu\text{L}/\text{min}$ )	Water inlet $Ca$
1	10.7	66.6	5	0.0011
2	10.7	66.6	10	0.0023
3	10.7	66.6	15	0.0034
4	10.7	66.6	20	0.0046
5	10.7	66.6	25	0.0057
6	10.7	66.6	30	0.0069
7	10.7	66.6	50	0.011

Figure 5.2, Figure 5.3 and Figure 5.4 show the liquid water behaviors and transport process in the microchannel under various water injection rates, with the air inlet velocity fixed at 10.7 m/s ( $Re = 66.6$ ). The dark blue area represents the gas phase while the red area represents the liquid water. The liquid water evolvement process and flow regimes can be classified into the following categories: squeezing flow (Figure 5.2), partial-jetting flow (Figure 5.3) and jetting flow (Figure 5.4).

#### ***A. Squeezing flow***

The squeezing flow is observed under lower water injection rate (5  $\mu\text{L}/\text{min}$  and 10  $\mu\text{L}/\text{min}$ , corresponding to  $Ca = 0.0011$  and 0.0023) as shown in Figure 5.2(a) and (b). At the very beginning, the liquid water emerges into the microchannel and forms the water blob [16]. Under the low water inlet flow rate, the water slug grows stably with no significant distortion and partially blocks the channel. At this stage, a pressure drop is induced across the blob and the air flow continuously acts on the water and squeezes its windward-side interface [24], which makes the neck of the water blob (connection

between the windward interface and liquid inlet) thinner. When the wall adhesion force is not able to balance the drag force from the air flow, the liquid water detaches from the liquid inlet and forms a single separated blob. This first detached blob moves towards the channel outlet and liquid water will be continuously squeezed out from the liquid inlet and form a queue of small blobs in the microchannel.

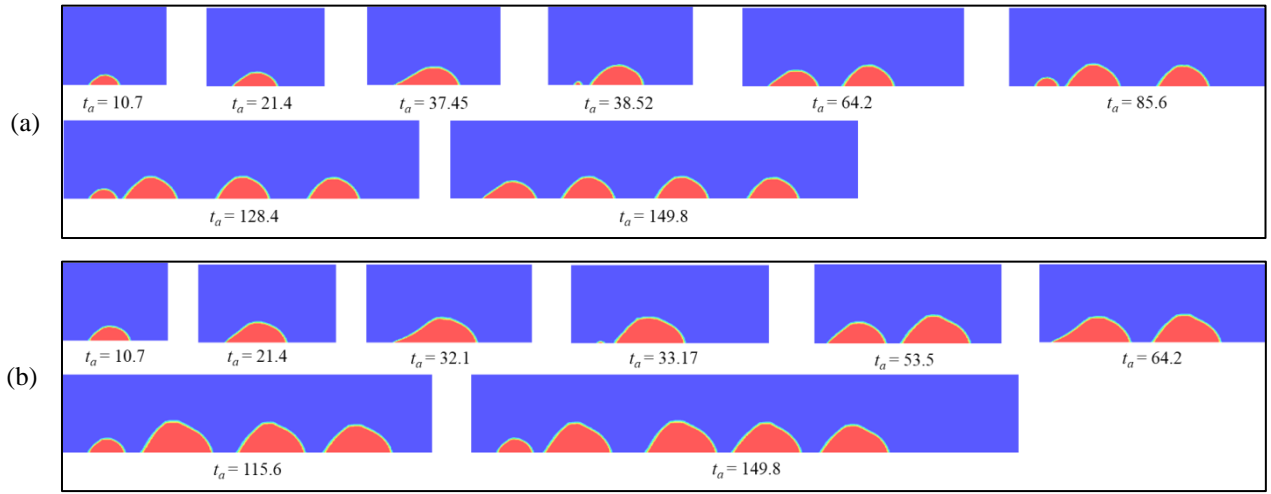


Figure 5.2: Liquid water evolution (squeezing flow) at  $V_{\text{air}} = 10.7 \text{ m/s}$  ( $Re = 66.6$ ) under various water injection rates: (a)  $5 \mu\text{L}/\text{min}$  ( $Ca = 0.0011$ ); (b)  $10 \mu\text{L}/\text{min}$  ( $Ca = 0.0023$ ).

### ***B. Partial-jetting flow***

As shown in Figure 5.3, when the water inlet flow rate  $Q_{\text{water}}$  is increased to  $15 \mu\text{L}/\text{min}$  ( $Ca = 0.0034$ ), the water blob is able to remain at the inlet area for longer time and form a concave interface at the windward side. After the detachment of the first blob (around  $t_a = 49.22$ ), some interesting phenomena can be observed for the liquid water deformation: for the first detached blob, the gas-liquid interface at the windward side significantly recedes under the continuous air flow and the blob height is also increased; at a critical point (about  $t_a = 68.76$ ), the upper part of the blob is squeezed and blown away ( $t_a = 69.66$ ) and reattaches to the bottom wall, mainly caused by the enhanced shear stress due to the reduced gap between the slug surface and the channel top wall. The water blob shape is

also deformed from “tall-standing” to “long-lying” ( $t_a = 72.27$ ). This evolvement process of the detached blob is significantly different from the squeezing flow and can be considered as partial-jetting flow regime. Afterwards, under the combined effects of continuous air flow and surface tension, the windward side will retract and the slug deforms to the “tall-standing” shape again ( $t_a = 85.6$ ) and move towards the channel outlet.

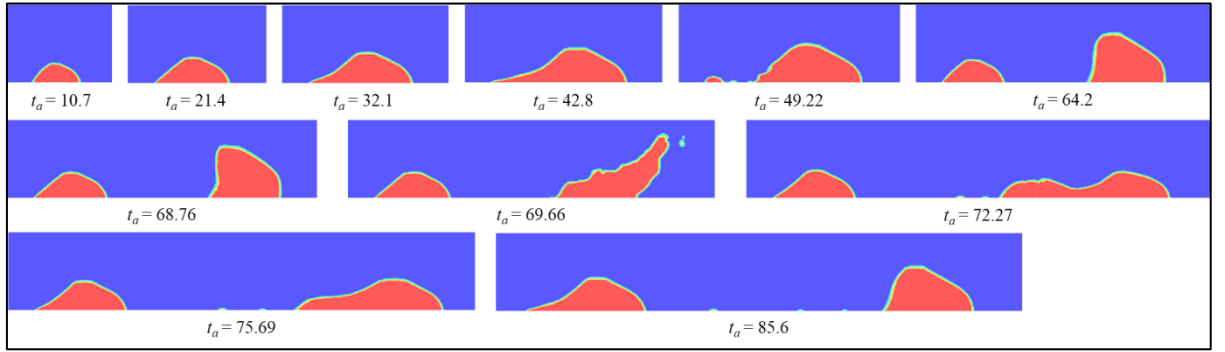


Figure 5.3: Liquid water evolvement (partial-jetting flow) at  $V_{\text{air}} = 10.7$  m/s ( $Re = 66.6$ ) and water injection rate  $15 \mu\text{L}/\text{min}$  ( $Ca = 0.0034$ ).

### C. Jetting flow

The jetting flow is observed when the  $Q_{\text{water}}$  is further increased to  $20 \mu\text{L}/\text{min}$  ( $Ca = 0.0046$ ) and higher, as shown in Figure 5.4(a-d). At the first stage, it can be seen that the liquid water forms a small liquid film at the trailing side of the blob. Unlike the case of  $Q_{\text{water}} = 15 \mu\text{L}/\text{min}$  ( $Ca = 0.0034$ ), the head of the water blob is directly blown away by the air flow without detachment from the liquid inlet and the liquid water deforms significantly and converts into jetting flow. In some cases where  $Q_{\text{water}} = 20 \mu\text{L}/\text{min}$ ,  $30 \mu\text{L}/\text{min}$  and  $50 \mu\text{L}/\text{min}$  ( $Ca = 0.0046$ ,  $0.069$  and  $0.011$ ), the stream of water re-accumulates and form a slug head, and the head slug will be blown away again. Finally, the liquid water drains out of the microchannel in the form of long, thin film. It is also



noted that, the higher liquid water injection rate can facilitate blockage and induce faster transition from squeezing stage to jetting flow.

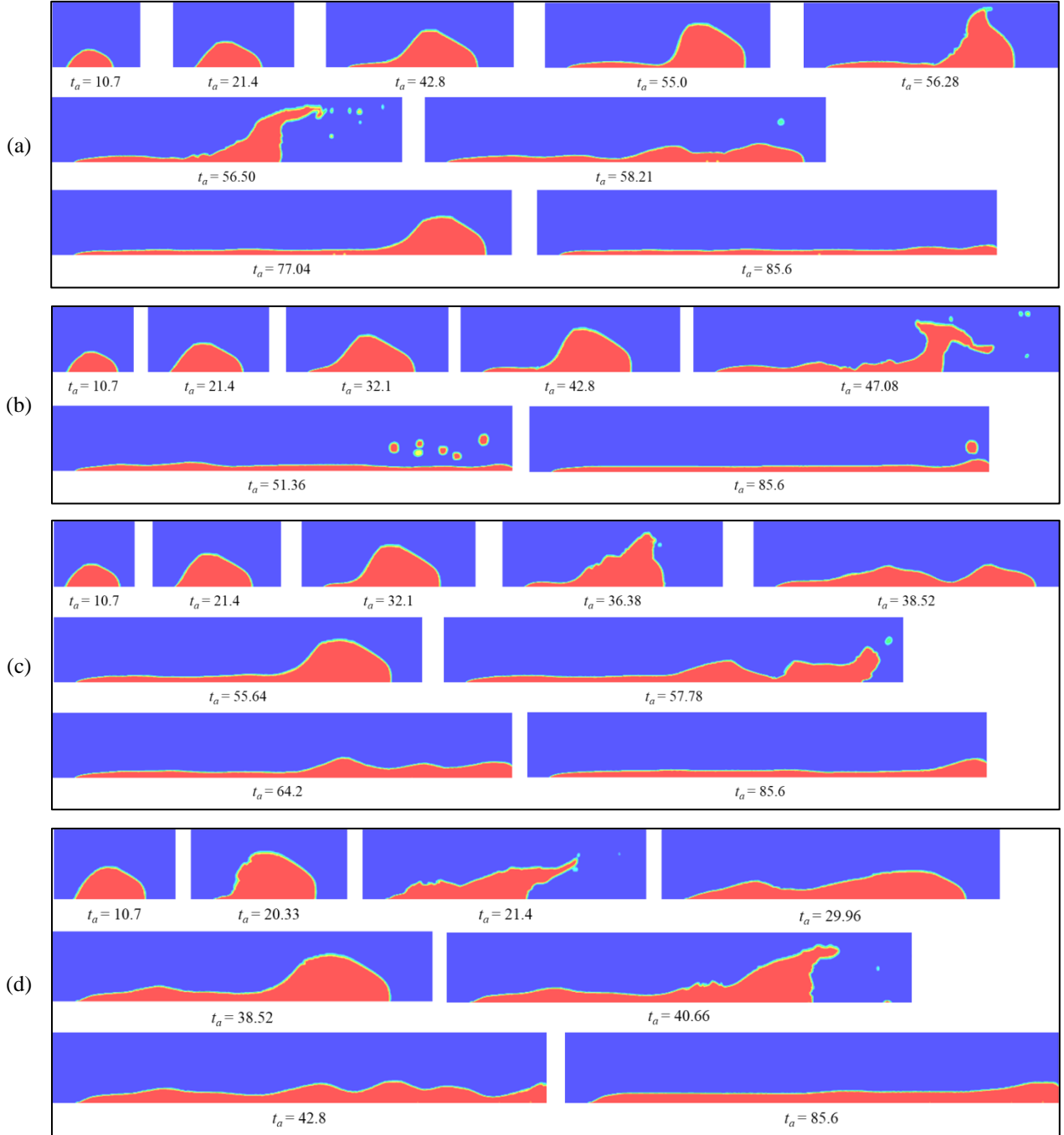


Figure 5.4: Liquid water evolution (squeezing flow) at  $V_{\text{air}} = 10.7$  m/s ( $Re = 66.6$ ) under various water injection rates: (a) 20  $\mu\text{L}/\text{min}$  ( $Ca = 0.0046$ ); (b) 25  $\mu\text{L}/\text{min}$  ( $Ca = 0.0057$ ); (c) 30  $\mu\text{L}/\text{min}$  ( $Ca = 0.0069$ ); (d) 50  $\mu\text{L}/\text{min}$  ( $Ca = 0.011$ ).

### 5.3.2. Liquid Water Behaviors under Different Air Inlet Flow Rates

In addition to the water inlet flow rate, the air inlet velocity could be another critical factor that leads to different flow patterns. Therefore, in the second section, the liquid water behaviors with different air inlet velocities (4.8 m/s, 10.7 m/s and 18.1 m/s, corresponding to the  $Re$  of 29.9, 66.6, and 112.7 respectively) are studied, under various water injection rates (5  $\mu\text{L}/\text{min}$ , 10  $\mu\text{L}/\text{min}$ , 25  $\mu\text{L}/\text{min}$ , corresponding to the  $Ca$  number of 0.0011, 0.0023, 0.0057). A dimensionless time  $t_w$  is used to present the liquid water evolvment process in the microchannel instead of  $t_a$  in the previous section ( $t_w = t V_{\text{water}}/H_c$ , where  $t$  is the simulation time from liquid water emergence and  $H_c$  is the height of the microchannel).

Figure 5.5(a)-(c) show the comparison of the liquid water behaviors under different air inlet velocities when the water injection rate is set as 5  $\mu\text{L}/\text{min}$  ( $Ca = 0.0011$ ). It is noticed that, with the increase of the air inlet velocity, the liquid water detachment process will be significantly accelerated. As shown in Figure 5.5(a), due to the lower air inlet velocity ( $Re = 29.9$ ) and water injection rate ( $Ca = 0.0011$ ), the liquid water continuously accumulates and forms a water slug; whereas for the higher  $V_{\text{air}}$  ( $Re = 66.6$ ), the liquid water detaches earlier and forms the squeezing flow in the microchannel as discussed in the previous section; when the  $V_{\text{air}}$  is further increased to 18.1 m/s ( $Re = 112.7$ ), the stronger air flow will further facilitate the liquid water detachment and a string of water blob is formed with smaller size compared to the case of  $Re = 66.6$ . Some interesting phenomena can also be observed in Figure 5.5(c): due to the high inertial air flow, some of the small water blobs will merge together and form a new blob.

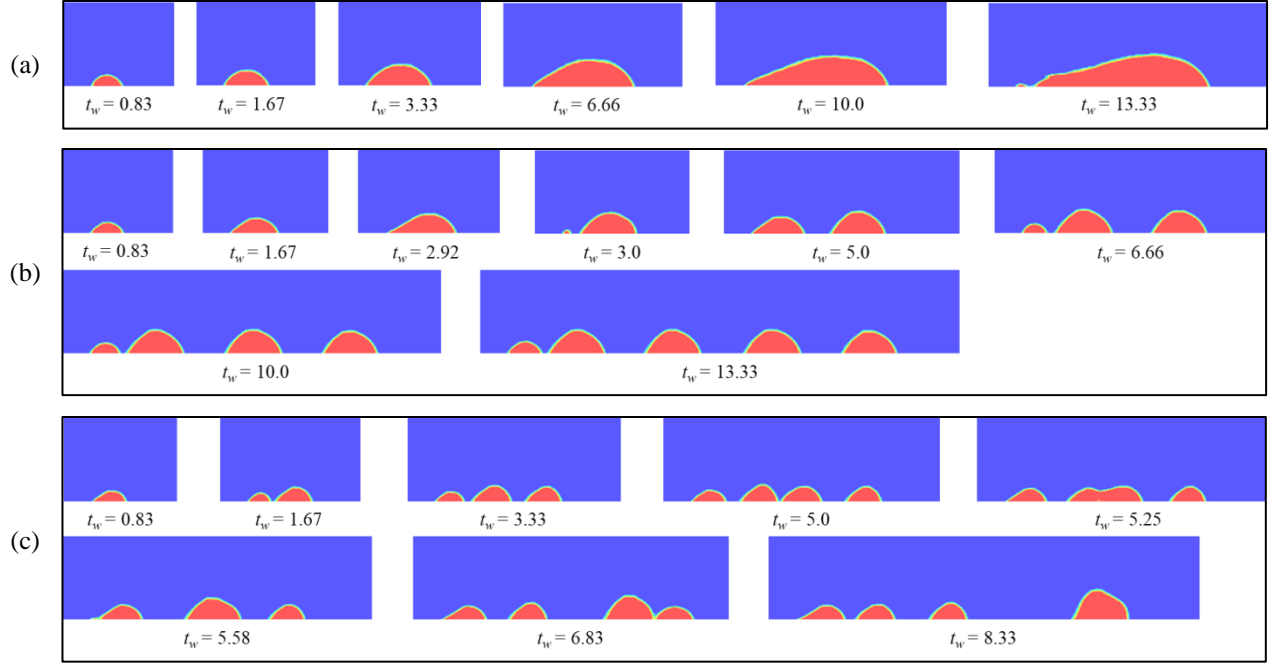


Figure 5.5: Liquid water evolution under different air inlet velocities at  $Q_{\text{water}} = 5 \mu\text{L}/\text{min}$  ( $Ca = 0.0011$ ): (a)  $V_{\text{air}} = 4.8 \text{ m/s}$  ( $Re = 29.9$ ) (b)  $V_{\text{air}} = 10.7 \text{ m/s}$  ( $Re = 66.6$ ), (c)  $V_{\text{air}} = 18.1 \text{ m/s}$  ( $Re = 112.7$ ).

Figure 5.6(a)-(c) show the flow behaviors from different  $V_{\text{air}}$  at the water injection rate of  $10 \mu\text{L}/\text{min}$  ( $Ca = 0.0023$ ). Under the lower  $V_{\text{air}}$  (4.8 m/s), the slug flow is observed inside the microchannel. Meanwhile, the air flow will continuously press the air-water interface at the windward side, leading to the formation of a long film attached to the water slug, as shown in Figure 5.6(a). For the  $V_{\text{air}} = 10.7 \text{ m/s}$  ( $Re = 66.6$ ), the squeezing flow regime is dominated as discussed above. When the  $Re$  number is further increased to 112.7, the water blobs quickly detach from the water injection area and merge together as shown in Figure 5.6(c); then the merged blob will experience an unstable evolution process including being blown away toward the downstream, reattaching to the bottom wall and re-accumulating, which is similar to the partial-jetting flow as shown in Figure 5.3.

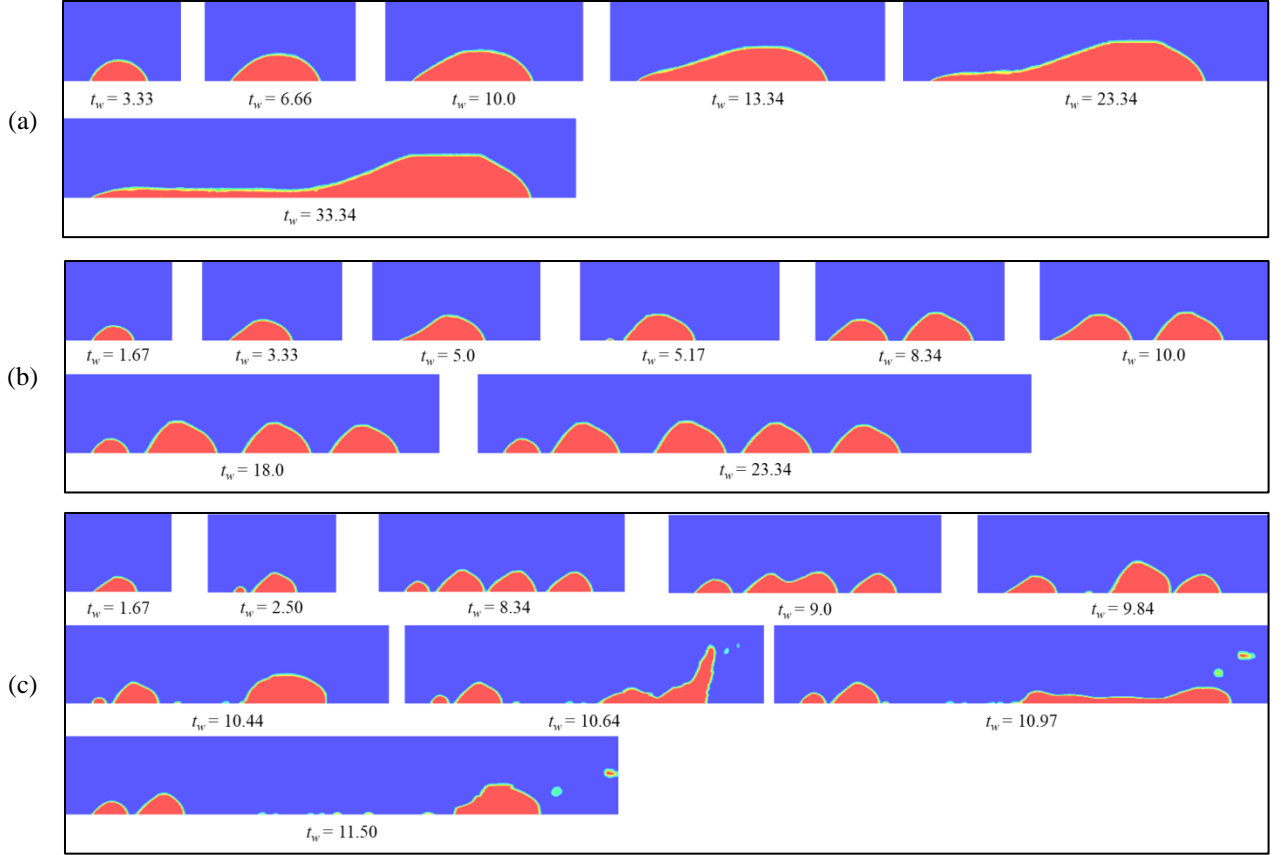


Figure 5.6: Liquid water evolution under different air inlet velocities at  $Q_{\text{water}} = 10 \mu\text{L}/\text{min}$  ( $Ca = 0.0023$ ): (a)  $V_{\text{air}} = 4.8 \text{ m/s}$  ( $Re = 29.9$ ) (b)  $V_{\text{air}} = 10.7 \text{ m/s}$  ( $Re = 66.6$ ), (c)  $V_{\text{air}} = 18.1 \text{ m/s}$  ( $Re = 112.7$ ).

When the water injection rate is further increased to  $25 \mu\text{L}/\text{min}$  ( $Ca = 0.0057$ ), the typical jetting flow regime in the microchannel is observed in Figure 5.7. Comparing with the simulation results among different  $V_{\text{air}}$  under fixed water injection rate, it is noted that with the increase of the air inlet velocity, the transition process from water blob or slug to the jetting flow is accelerated, i.e., the liquid water can be blown away by the air flow more quickly. Also, the higher air  $Re$  can lead to thinner liquid film attached on the bottom wall.

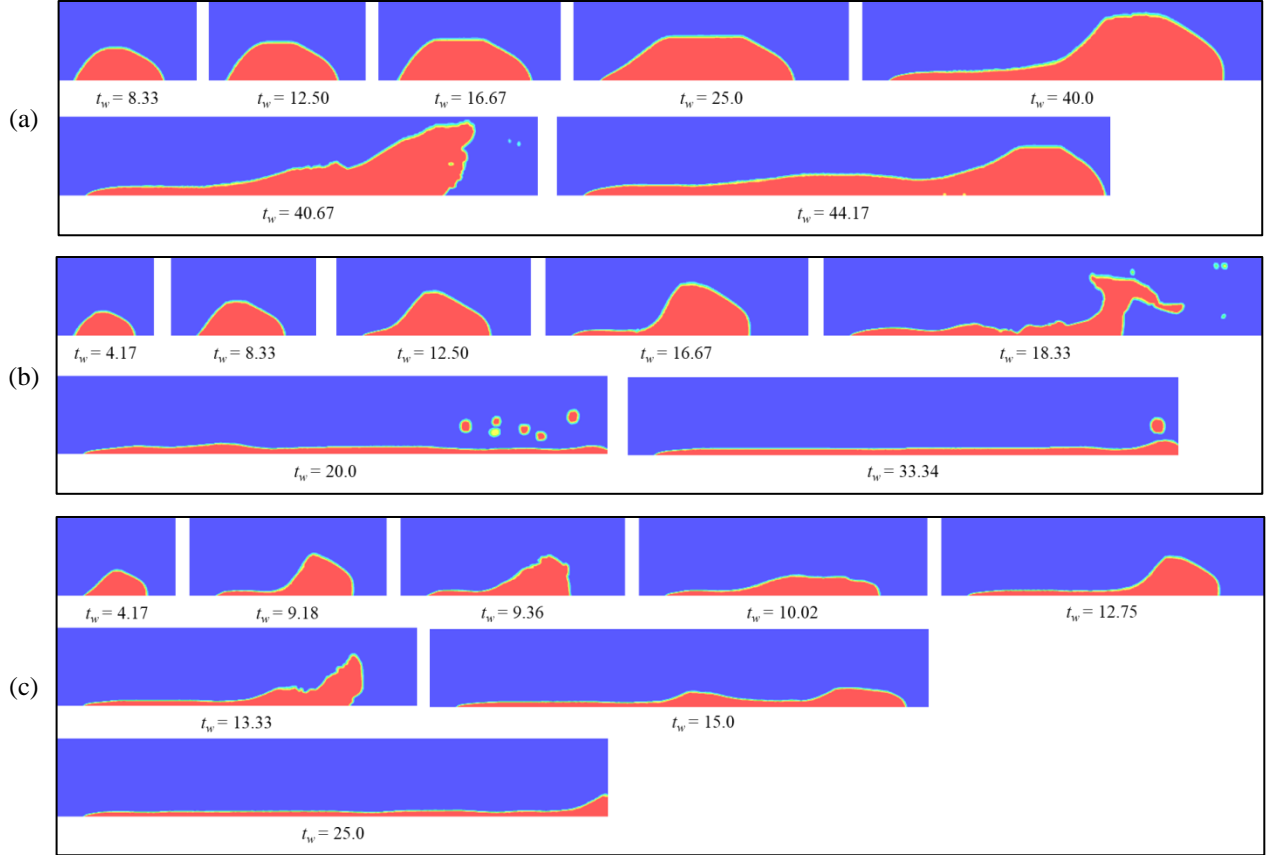


Figure 5.7: Liquid water evolution under different air inlet velocities at  $Q_{\text{water}} = 25 \mu\text{L}/\text{min}$  ( $Ca = 0.0057$ ): (a)  $V_{\text{air}} = 4.8 \text{ m/s}$  ( $Re = 29.9$ ) (b)  $V_{\text{air}} = 10.7 \text{ m/s}$  ( $Re = 66.6$ ), (c)  $V_{\text{air}} = 18.1 \text{ m/s}$  ( $Re = 112.7$ ).

## 5.4. Conclusions

In this study, the liquid water behavior and flow regimes in a single straight microchannel are simulated using the VOF method and dynamic contact angle, considering various water injection rates  $Q_{\text{water}}$  ( $5 \mu\text{L}/\text{min}$  to  $50 \mu\text{L}/\text{min}$ , with  $Ca$  ranged from 0.0011 to 0.011) and air inlet velocities  $V_{\text{air}}$  ( $4.8 \text{ m/s}$ ,  $10.7 \text{ m/s}$  and  $18.1 \text{ m/s}$ , with  $Re$  of 29.9, 66.6 and 112.7 respectively). The numerical results indicate that the water injection rate plays a dominant role in the formation of different flow regimes. The squeezing flow occurs at low  $Q_{\text{water}}$  ( $Ca = 0.0011$  and  $0.0023$ ) where the liquid water continuously detach from the water inlet and form a queue of water blobs in the microchannel. The jetting flow is

observed under high  $Q_{\text{water}}$  ( $Ca \geq 0.0046$ ) where the water blob head will be blown away by the air flow and forms a steam of water in the microchannel without detachment. An interesting partial-jetting flow is also captured ( $Ca = 0.0034$  and  $Re = 66.6$ ) where the first detached water blob has similar evolvement process as the jetting flow. In addition to the liquid water injection rate, the air inlet velocity  $V_{\text{air}}$  also has notable effects on the flow patterns in the microchannel. It is found that for the squeezing flow, the low  $V_{\text{air}}$  will significantly delay the liquid water detachment and form a water slug in the microchannel; whereas for the high  $V_{\text{air}}$ , the liquid water quickly detaches from the water inlet and form a string of water blobs. Also, due to the high inertial air flow, the detached water blobs can also merge together as observed at  $V_{\text{air}} = 18.1$  m/s ( $Re = 112.7$ ). On the other hand, for the jetting flow, the increased air flow velocity will facilitate the transition process from water blob or slug to the water film.

## References

- [1] Li H, Tang Y, Wang Z, Shi Z, Wu S, Song D, Zhang J, Fatih K, Zhang J, Wang H, Liu Z. A review of water flooding issues in the proton exchange membrane fuel cell. *Journal of Power Sources*. 2008 Mar 15;178(1):103-17.
- [2] Ferreira RB, Falcão DS, Oliveira VB, Pinto AM. Numerical simulations of two-phase flow in proton exchange membrane fuel cells using the volume of fluid method—A review. *Journal of Power Sources*. 2015 Mar 1;277:329-42.
- [3] Quan P, Zhou B, Sobiesiak A, Liu Z. Water behavior in serpentine micro-channel for proton exchange membrane fuel cell cathode. *Journal of Power Sources*. 2005 Dec 1;152:131-45.

- [4] Wang X, Zhou B, Jiang M. Dynamic Contact Angle Effects on Gas-liquid Transport Phenomena in Proton Exchange Membrane Fuel Cell cathode with Parallel Design. *International Journal of Energy Research*. 2018.
- [5] Wang X, Zhou B, Jiang M. Dynamic Contact Angle Effects on Gas-Liquid Behaviors in the Cathode of Proton Exchange Membrane Fuel Cell with Stirred Tank Reactor Design. Submitted to *International Journal of Green Energy*. 2018.
- [6] Šikalo Š, Wilhelm HD, Roisman IV, Jakirlić S, Tropea C. Dynamic contact angle of spreading droplets: Experiments and simulations. *Physics of Fluids*. 2005 Jun;17(6):062103.
- [7] Miller C. Liquid water dynamics in a model polymer electrolyte fuel cell flow channel, MASC Thesis, University of Victoria, 2009.
- [8] Lunkad SF, Buwa VV, Nigam KD. Numerical simulations of drop impact and spreading on horizontal and inclined surfaces. *Chemical Engineering Science*. 2007 Dec 31;62(24):7214-24.
- [9] Roisman IV, Opfer L, Tropea C, Raessi M, Mostaghimi J, Chandra S. Drop impact onto a dry surface: Role of the dynamic contact angle. *Colloids and Surfaces A: Physicochemical and Engineering Aspects*. 2008 Jun 5;322(1):183-91.
- [10] Legendre D, Maglio M. Numerical simulation of spreading drops. *Colloids and Surfaces A: Physicochemical and Engineering Aspects*. 2013 Sep 5;432:29-37.
- [11] Malgarinos I, Nikolopoulos N, Marengo M, Antonini C, Gavaises M. VOF simulations of the contact angle dynamics during the drop spreading: standard models and a new wetting force model. *Advances in Colloid and Interface Science*. 2014 Oct 31;212:1-20.
- [12] Jiang M, Zhou B. Numerical Study of Droplet Impact on Inclined Surface: Viscosity Effects. *ECS Transactions*. 2018 Jan 4;83(1):127-36.
- [13] Jiang M, Zhou B, Wang X. Comparisons and validations of contact angle models. *International Journal of Hydrogen Energy*. 2018 Mar 22;43(12):6364-78.
- [14] Jiang M, Zhou B, Droplet Behaviors on Inclined Surfaces with Dynamic Contact Angle. Submitted to *International Journal of Multiphase Flow*. 2018.

- [15]Qin Y, Li X, Yin Y. Modeling of liquid water transport in a proton exchange membrane fuel cell gas flow channel with dynamic wettability. *International Journal of Energy Research*. 2018.
- [16]Hidrovo CH, Wang FM, Lee ES, Vigneron S, Steinbrenner JE, Paidipati JV, Kramer TA, Eaton JK, Goodson KE. Experimental investigation and visualization of two-phase flow and water transport in microchannels. In *ASME 2004 International Mechanical Engineering Congress and Exposition 2004 Jan 1* (pp. 205-212). American Society of Mechanical Engineers.
- [17]Hidrovo CH, Wang FM, Steinbrenner JE, Lee ES, Vigneron S, Cheng CH, Eaton JK, Goodson KE. Water slug detachment in two-phase hydrophobic microchannel flows. In *ASME 3rd International Conference on Microchannels and Minichannels 2005 Jan 1* (pp. 709-715). American Society of Mechanical Engineers.
- [18]Carroll B, Hidrovo C. Droplet detachment mechanism in a high-speed gaseous microflow. *Journal of Fluids Engineering*. 2013 Jul 1;135(7):071206.
- [19]Wu TC, Djilali N. Experimental investigation of water droplet emergence in a model polymer electrolyte membrane fuel cell microchannel. *Journal of Power Sources*. 2012 Jun 15;208:248-56.
- [20]Cho SC, Wang Y, Chen KS. Droplet dynamics in a polymer electrolyte fuel cell gas flow channel: Forces, deformation, and detachment. I: Theoretical and numerical analyses. *Journal of Power Sources*. 2012 May 15;206:119-28.
- [21]Cho SC, Wang Y, Chen KS. Droplet dynamics in a polymer electrolyte fuel cell gas flow channel: Forces, Deformation and detachment. II: Comparisons of analytical solution with numerical and experimental results. *Journal of Power Sources*. 2012 Jul 15;210:191-7.
- [22]Andersson M, Mularczyk A, Lamibrac A, Beale SB, Eller J, Lehnert W, Büchi FN. Modeling and synchrotron imaging of droplet detachment in gas channels of polymer electrolyte fuel cells. *Journal of Power Sources*. 2018 Nov 15;404:159-71.
- [23]Zhu X, Sui PC, Djilali N. Three-dimensional numerical simulations of water droplet dynamics in a PEMFC gas channel. *Journal of Power Sources*. 2008 Jun 15;181(1):101-15.



- [24] Mastiani M, Mosavati B, Kim MM. Numerical simulation of high inertial liquid-in-gas droplet in a T-junction microchannel. *RSC Advances*. 2017;7(77):48512-25.

## CHAPTER 6

### CONCLUSIONS AND FUTURE WORKS

#### 6.1. Summary and Conclusions

This thesis mainly focused on the numerical simulation of two phase flow using the VOF method with dynamic contact angle, including the droplet impact on horizontal and inclined surfaces and liquid water behaviors in microchannel. The main findings and conclusions are summarized as follows:

- (1) The AR-DCA model was proposed based on the fundamental understanding of Hoffman function, which considers both advancing and receding dynamic contact angles in the simulation process. This model overcomes the obvious limitation of the A-DCA model, which evaluates only the advancing dynamic contact angles in the simulation. Also, the AR-DCA model was successfully validated by comparing the simulations of droplet impact and spreading on horizontal and inclined surfaces to the corresponding experiments from literature, in both qualitative and quantitative methods. It was indicated that the AR-DCA model has superior capability in the prediction of droplet behaviors compared to A-DCA model and SCA model.
- (2) Following the work of comparisons and validations of different contact angle models (Chapter 2), the AR-DCA model was further applied to simulate the droplet behaviors on inclined surfaces under different impact velocities, impact angles and droplet viscosities. It was indicated that, on one hand, the droplet impact velocity has no significant effects on the spreading factors at both leading

and trailing edges for hydrophilic cases, whereas under the hydrophobic condition, the higher impact velocity leads to less sliding distance of the trailing edge relative to the impact point; on the other hand, the larger impact angle can reduce the sliding distance between the trailing edge and the impact point for both hydrophilic and hydrophobic cases. The effects of droplet viscosity were studied based on the case of glycerin droplet impact on smooth glass and the results showed that higher droplet viscosity facilitates the droplet rebound phenomena but also leads to decrease of droplet sliding distance on the surface. Moreover, the droplet deformation and evolving phenomena from the simulation had excellent agreement with the corresponding experiments, which further demonstrated the capability of the AR-DCA model in the prediction of droplet behaviors on surfaces under various conditions.

- (3) In Chapter 4, the i-AR-DCA model was developed by improving the evaluation method of contact line velocity in the AR-DCA model. The droplet impact on inclined surface and liquid water behaviors in a microchannel were simulated using the AR-DCA and i-AR-DCA models to investigate the effects of the modified methodology. It was indicated that the improved methodology can lead to the increase of receding dynamic contact angle and decrease of advancing dynamic contact angle, which makes the liquid film repel from the surface more easily and form small droplets at the trailing edge for water droplet spreading on smooth glass; whereas for the microchannel case, the i-AR-DCA model can lead to early detachment of liquid water compared to the results from the original AR-DCA model. Therefore, under complex surrounding gas flow, it is very critical to

implement the real contact line velocity evaluation in the DCA models for the simulations.

- (4) The liquid water behaviors and flow regimes in a single straight microchannel were simulated and investigated under various air and water inlet flow rates. The results showed that the water injection rates significantly affect the formation of different flow regimes: the squeezing flow, partial-jetting flow and jetting flow occur with the increase of water inlet flow rate. Also, the air inlet velocity can lead to different liquid water evolvment and flow patterns. The lower air inlet velocity induced the delay of liquid water detachment for the squeezing flow and water slug was formed in the microchannel; whereas under higher air flow rate, the unique merging process of liquid blob was observed. Also, for the jetting flow, the higher inertial air flow can facilitate the transition from water blob to film flow.

## **6.2. Recommendations and Future Works**

This thesis presented a systematic study on the two-phase flow simulation with dynamic contact angle. The AR-DCA model provides a very promising methodology to predict the droplet spreading phenomena and evolvment process on surfaces, and can be further applied in some future research related to gas-liquid two-phase flow problems.

This study also proposed a methodology to further improve the AR-DCA model with respect to the evaluation method of contact line velocity and the i-AR-DCA model was developed. The liquid water behaviors and flow regimes in a microchannel under various air and water inlet flow rates were simulated. However, more reliable experiments should be carried out to further validate the proposed i-AR-DCA model for its capability in the

simulation of liquid water behaviors in more complex domains, such as the cathodes of PEMFCs with different flow field designs.

The author also tried to apply the Eulerian multi-fluid VOF model to simulate liquid water behaviors in microchannel but only a few preliminary results were presented (see Appendix A). In the future, this numerical methodology needs to be further tested and developed to investigate its potential in the delay of droplet/slug detachment in microchannels. Specifically, a user-defined-function (UDF) code can be developed to adjust the interface exchange coefficient  $K_{pq}$ . Moreover, the implementation of DCA model with the multi-fluid VOF model also needs to be investigated.

## APPENDICES

### *Appendix A*

#### NUMERICAL SIMULATION OF LIQUID WATER BEHAVIORS IN MICROCHANNEL USING THE MULTI-FLUID VOLUME OF FLUID METHOD

##### **A.1. Introduction**

Liquid water management is still a very critical challenge in the commercialization of proton exchange membrane fuel cells (PEMFCs). Using the numerical modeling and simulation based on computational fluid dynamics (CFD), researchers can obtain basic understanding on the two-phase flow phenomena in PEMFCs. In early years, the mixture model and the multi-fluid model (also known as two-fluid model) were used to simulate two-phase flow in PEMFCs, such as the previous works [1-7]. However, these two methods are not able to well reflect the formation or flow patterns of liquid water such as droplet, slug or film flow. In addition, the location and transport process of liquid water in gas channel or porous media are not able to be predicted. Therefore, the numerical model that is capable of gas-liquid interface tracking is further considered in the simulation of two-phase flow in PEMFCs, such as the level set method [8-10], the Lattice Boltzmann method [11-13] and the volume of fluid (VOF) method.

So far, among the available literature in regards to gas-liquid behavior simulations in PEMFCs, the VOF method is the most widely used approaches [14]. The first study in this research field was proposed by Quan et al. [15]. The authors numerically studied the air-water flow behaviors in a PEMFC serpentine channel and compared five different cases with increasing initial water content to predict potential fuel cell operating conditions. Later, Jiao et al. [16] proposed an accelerated model to increase the water

velocity from the PEMFC reaction in the simulation, which greatly reduced the computational time and also provided a promising approach to the numerical simulation of two-phase flow in PEMFCs. In 2008, Le et al. [17] developed the one of the most complete PEMFC models which includes detailed thermos-electrochemistry, fluid flow, multi species, energy transport, etc., as well as all the necessary PEMFC components. Following the work of Le et al. [18] for a simplified general model, Wang et al. [19] and Kang et al. [20] studied the liquid water transport process in PEMFC cathode with parallel and interdigitated design respectively. In addition to the conventional flow field designs, some novel flow channel designs were also introduced and the liquid water transport was simulated using the VOF method, such as the innovative channel inserted with a hydrophilic needle [21] and a hydrophilic plate [22], novel channels with air and water baffle inside [23], etc. Recently, researchers also employed the VOF method to simulate CO<sub>2</sub> bubble behaviors in direct methanol fuel cell (DMFC, which is one type of PEMFC consuming methanol and oxygen and producing water and CO<sub>2</sub>) [24-26].

To the best of the author's knowledge, most of the PEMFC-related simulations with VOF method use static contact angle (SCA) as the wall boundary condition, including all the aforementioned studies [15-26]. However, the dynamic contact line treatment is very critical in order to predict the real droplet dynamics and deformation [27, 28]. Therefore, the dynamic contact angle (DCA) model should be considered instead of the SCA model. In terms of DCA simulation, the Hoffman function [29] has been used as a promising correlation in the simulation of droplet behavior on surfaces [30-32]. Jiang et al. [33] proposed an AR-DCA model to simulate the droplet spreading phenomena and behaviors on horizontal and inclined surfaces, using the VOF method. Both the advancing and

receding dynamic contact angles are considered in the simulation process and calculated by Hoffman function. The numerical results have excellent agreement with the corresponding experiments from Sikalo et al. [34, 35], showing the capability of the AR-DCA model in the prediction of droplet behaviors. However, the Hoffman function coupled with VOF method has an obvious limitation when it is applied to simulate droplet behaviors in gas channels: in the previous work by Wang [36], the numerical result of the droplet deformation and evolvement in a microchannel is not able to well match the experiment [37], unless the gas inlet velocity is decreased to the 1/3 of the original value; in the work of Wu [28], although the droplet shape in one emergence cycle showed good consistency with the experiment, the detachment time in the simulation (25.4ms for SCA model and 22.8 ms for DCA model) are much earlier than that of the experiment (75 ms). As facts, the liquid water transport and droplet dynamics are determined by many factors such as drag force, wall adhesion, gas/liquid inlet mass flow rate, etc. Considering the droplet motion in the simulation is always faster than that in the experiment, the drag force can be over-predicted in the current numerical model. Therefore, one potential solution is to modify the drag force exerted on the droplet to investigate the potential of slowing down the droplet motion and transport in microchannels.

For the current VOF model, only a single momentum equation is solved in the simulation process and resulting velocity field is shared among the phases [18], where the modification of the gas-liquid interface drag force is not able to be implemented. In ANSYS Fluent, the multi-fluid VOF model couples the VOF model and the Eulerian multiphase model, which enables the interface tracking as well as the drag force



modeling. However, so far, very limited amount of research has been reported for the multi-fluid VOF model application. Chen et al. [38] employed the multi-fluid VOF model to simulate the flooding phenomenon in an inclined pipe. Zahedi et al. [39] used both VOF method and multi-fluid VOF approach to simulate the annular flow behavior and validate the capability of CFD multiphase simulation in the erosion prediction. To date, no one has tried the multi-fluid VOF model in the simulation of droplet/slug flow in gas channels or microchannels.

In this study, we apply the multi-fluid VOF method to investigate its potential in the simulation of gas-liquid two-phase flow in microchannel. Some preliminary results will be presented and discussed, and compared to those based on the VOF method.

## **A.2. Numerical Model Description**

### **A.2.1. Computational Domain and Boundary Conditions**

For the numerical simulation, a single straight microchannel is used as the computational domain as shown in Figure A.1, which is the same as the one employed in Wang's work [36]. The length of the channel is 5 mm and the cross-section is  $500\ \mu\text{m} \times 45\ \mu\text{m}$ . The air inlet velocity is set as 15.56 m/s and the water inlet velocity is set as 0.09 m/s. In the current progress, SCA model is employed and the contact angle on the bottom wall and side wall is set as  $105^\circ$  and  $135^\circ$  respectively.

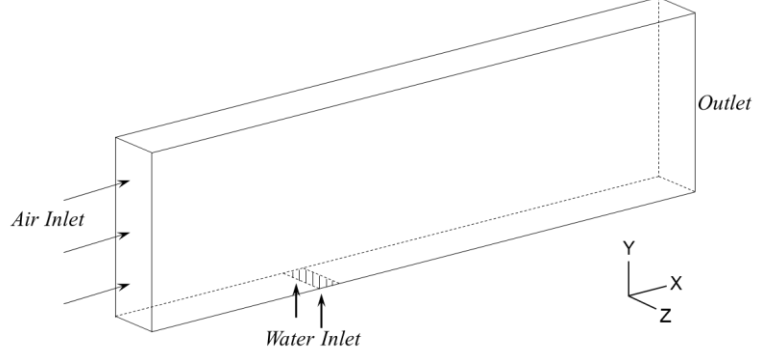


Figure A.1: Schematic of computational domain for microchannel.

### A.2.2. Numerical Methodology

In ANSYS Fluent, the multi-fluid VOF model couples the Eulerian model with the VOF model for the surface tracking. The general conservation equations are based on the Eulerian multiphase model, where the momentum and continuity equations are solved for each phase (normally named phase  $p$  and phase  $q$ . In this study, the air is considered as the primary phase  $q$  while the liquid water is the secondary phase  $p$ ) [40]. The main governing equations and interface force correlations are briefly introduced in this section. More detailed descriptions can be found in ANSYS Fluent Theory Guide [40].

For phase  $q$ , the continuity equation has the following form:

$$\frac{\partial}{\partial t}(\alpha_q \rho_q) + \nabla \cdot (\alpha_q \rho_q \vec{v}_q) = 0 \quad (\text{A.1})$$

where  $\alpha_q$  and  $\rho_q$  are the volume fraction and density of phase  $q$  respectively;  $\vec{v}_q$  is the velocity of phase  $q$ ;

The momentum equation for phase  $q$ :

$$\frac{\partial}{\partial t}(\alpha_q \rho_q \vec{v}_q) + \nabla \cdot (\alpha_q \rho_q \vec{v}_q \vec{v}_q) = -\alpha_q \nabla p + \nabla \cdot \vec{\tau}_q + \alpha_q \rho_q \vec{g} + \vec{R}_{pq} \quad (\text{A.2})$$

where  $p$  is the pressure shared by all phases;  $\vec{\tau}_q$  is the stress-strain tensor for the phase  $q$ ;  $\vec{R}_{pq}$  is an interaction force between phase  $p$  and phase  $q$ .

In the multi-fluid VOF model, the interface force  $\vec{R}_{pq}$  can be determined by the following form:

$$\sum_{p=1}^n \vec{R}_{pq} = \sum_{p=1}^n K_{pq}(\vec{v}_p - \vec{v}_q) \quad (\text{A.3})$$

In our case, only one phase  $p$  is modeled (liquid phase), therefore the Equation (A.3) becomes:

$$\vec{R}_{pq} = K_{pq}(\vec{v}_p - \vec{v}_q) \quad (\text{A.4})$$

where  $K_{pq}$  is the interphase momentum exchange coefficient;  $\vec{v}_p$  and  $\vec{v}_q$  represents the velocity of phase  $p$  and phase  $q$  respectively.

#### ▪ *Symmetric Drag Law*

The symmetric model is the default method for the multi-fluid VOF model. The density and viscosity are determined by the averaged properties based on volume fraction:

$$\rho_{pq} = \alpha_p \rho_p + \alpha_q \rho_q \quad (\text{A.5})$$

$$\mu_{pq} = \alpha_p \mu_p + \alpha_q \mu_q \quad (\text{A.6})$$

The diameter is the average of  $d_p$  and  $d_q$ :

$$d_{pq} = \frac{1}{2} (d_p + d_q) \quad (\text{A.7})$$

In the ANSYS Fluent Theory Guide [40], it is clarified that if there is only one dispersed phase, then  $d_p = d_q$ . Therefore, the diameter  $d_{pq}$  can be replaced by  $d_p$ .

In the fluid-fluid system, the exchange coefficient is expressed as:

$$K_{pq} = \frac{\rho_{pq} f}{6\tau_{pq}} d_p A_i \quad (\text{A.8})$$

where  $\tau_{pq}$  is the particulate relaxation time and defined as:

$$\tau_{pq} = \frac{\rho_{pq} d_p^2}{18\mu_{pq}} \quad (\text{A.9})$$

$A_i$  is the interfacial area concentration, i.e., the interfacial area between gas phase and liquid phase per unit mixture volume:

$$A_i = \frac{6\alpha_p(1 - \alpha_p)}{d_p} \quad (\text{A.10})$$

The drag function  $f$  in the symmetric model is defined as:

$$f = \frac{C_D Re}{24} \quad (\text{A.11})$$

where  $C_D$  is the drag coefficient and determined as:

$$C_D = \begin{cases} 24(1 + 0.15Re^{0.687})/Re & Re \leq 1000 \\ 0.44 & Re > 1000 \end{cases} \quad (\text{A.12})$$

$Re$  is the relative Reynolds number:

$$Re = \frac{\rho_{pq} |\vec{v}_p - \vec{v}_q| d_p}{\mu_{pq}} \quad (\text{A.13})$$

The numerical test of liquid water behaviors in a microchannel in the present study is conducted based on the multi-fluid VOF method with the default symmetric model.

### **A.3. Preliminary Results and Discussion**

The numerical simulation of liquid water behavior in microchannel is conducted using the multi-fluid VOF method with the default symmetric drag law in ANSYS Fluent [40], and the results are compared to those based on the VOF model with SCA under the same conditions (air and water inlet flow rate, wall contact angles, etc.), as shown in Figure A.2. A dimensionless time  $t_a$  is used to present the liquid water evolvement process in the microchannel ( $t_a = t V_{\text{air}}/L_c$ , where  $t$  is the simulation time from liquid water emergence and  $L_c$  is the length of the microchannel. From the qualitative observation, it is found that the general liquid water evolvement and transport process from these two methods are very similar: at the very beginning, the liquid water is supplied into the channel through the liquid inlet with a constant flow rate and the formation of water slug is initiated. With time, the slug size is growing in both length and height direction, and the profile has no significant distortion in this process. When it comes to about  $t_a = 21.16$ , the first water slug is detached from the inlet area and quickly moves toward the outlet. In order to further evaluate and compare the slug deformation before the detachment, the ratio of slug length to height ( $l/h$ ) is plotted, as shown in Figure A.3. It is noted that before approximately  $t_a = 12.45$ , the evolution of  $l/h$  from these two methods are almost identical and the value of  $l/h$  are around 2.25 before  $t_a = 9.34$ . After that till the slug detachment, the value of  $l/h$  increases with time for both methods and the results from the multi-fluid VOF model becomes higher than that of the VOF model, indicating that the multi-fluid VOF method can leads to slightly longer elongation of the slug.

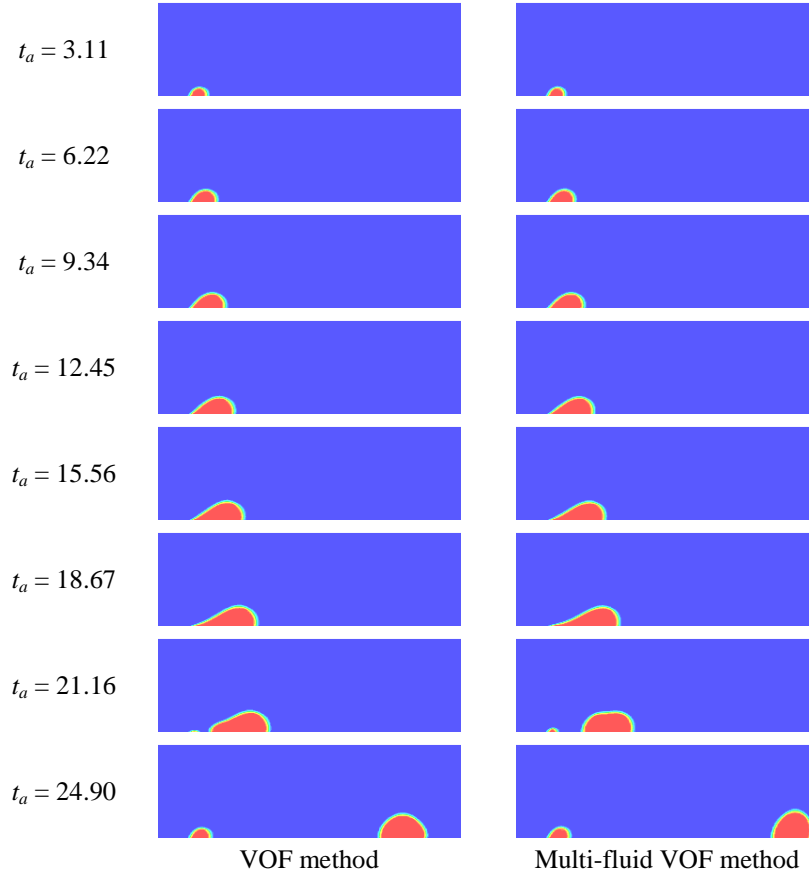


Figure A.2: Numerical results of liquid water evolution based on the VOF method (left column) and the multi-fluid VOF method (right column).

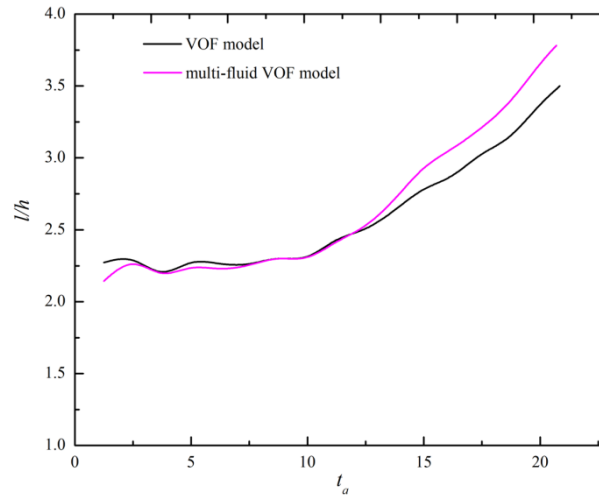


Figure A.3: Comparison of the ratio of water slug length to height ( $l/h$ ) before detachment of the first slug from VOF model and multi-fluid VOF model.

#### **A.4. Summary and Future Work**

In this study, the numerical simulation of liquid water behaviors in a single straight microchannel was conducted using the ANSYS Fluent multi-fluid VOF model. The results were compared qualitatively and quantitatively to those based on the VOF model. It was indicated that the general liquid water evolvment and transport process between these two models had no significant difference. However, by comparing the ratio of the water slug length to height, it was found that the multi-fluid VOF method can lead to slightly longer elongation of the slug. In addition, using the multi-fluid VOF method with the default symmetric drag law in ANSYS Fluent [40], the slug detachment time was nearly identical to that from the VOF model. Further investigation is still needed to investigate the potential of the multi-fluid VOF model in the delay of slug detachment in microchannels.

For the future work, a user-defined-function (UDF) code can be developed to modify the interface exchange coefficient  $K_{pq}$ , and investigate the effects on the liquid water evolvment process. Also, this paper only presents some preliminary results based on the multi-fluid VOF model using the SCA as the boundary condition, and a proper methodology needs to be further developed to implement DCA model.

#### **References**

- [1] Wang ZH, Wang CY, Chen KS. Two-phase flow and transport in the air cathode of proton exchange membrane fuel cells. Journal of power sources. 2001 Feb 15;94(1):40-50.

- [2] Meng H, Wang CY. Model of two-phase flow and flooding dynamics in polymer electrolyte fuel cells. *Journal of the Electrochemical Society*. 2005 Sep 1;152(9):A1733-41.
- [3] Koido T, Furusawa T, Moriyama K. An approach to modeling two-phase transport in the gas diffusion layer of a proton exchange membrane fuel cell. *Journal of Power Sources*. 2008 Jan 3;175(1):127-36.
- [4] Basu S, Li J, Wang CY. Two-phase flow and maldistribution in gas channels of a polymer electrolyte fuel cell. *Journal of Power Sources*. 2009 Feb 15;187(2):431-43.
- [5] Berning T, Djilali N. A 3D, multiphase, multicomponent model of the cathode and anode of a PEM fuel cell. *Journal of the Electrochemical Society*. 2003 Dec 1;150(12):A1589-98.
- [6] He G, Ming P, Zhao Z, Abudula A, Xiao Y. A two-fluid model for two-phase flow in PEMFCs. *Journal of Power Sources*. 2007 Jan 1;163(2):864-73.
- [7] Ye Q, Van Nguyen T. Three-dimensional simulation of liquid water distribution in a PEMFC with experimentally measured capillary functions. *Journal of the Electrochemical Society*. 2007 Dec 1;154(12):B1242-51.
- [8] Choi J, Son G. Numerical study of droplet motion in a microchannel with different contact angles. *Journal of mechanical science and technology*. 2008 Dec 1;22(12):2590.
- [9] Choi J, Son G. Numerical study of droplet dynamics in a PEMFC gas channel with multiple pores. *Journal of mechanical science and technology*. 2009 Jul 1;23(7):1765-72.
- [10] Akhtar N, Kerkhof PJ. Dynamic behavior of liquid water transport in a tapered channel of a proton exchange membrane fuel cell cathode. *International Journal of Hydrogen Energy*. 2011 Feb 1;36(4):3076-86.
- [11] Park J, Li X. Multi-phase micro-scale flow simulation in the electrodes of a PEM fuel cell by lattice Boltzmann method. *Journal of Power Sources*. 2008 Mar 15;178(1):248-57.



- [12]Kim KN, Kang JH, Lee SG, Nam JH, Kim CJ. Lattice Boltzmann simulation of liquid water transport in microporous and gas diffusion layers of polymer electrolyte membrane fuel cells. *Journal of Power Sources*. 2015 Mar 15;278:703-17.
- [13]Deng H, Jiao K, Hou Y, Park JW, Du Q. A lattice Boltzmann model for multi-component two-phase gas-liquid flow with realistic fluid properties. *International Journal of Heat and Mass Transfer*. 2019 Jan 1;128:536-49.
- [14]Ferreira RB, Falcão DS, Oliveira VB, Pinto AM. Numerical simulations of two-phase flow in proton exchange membrane fuel cells using the volume of fluid method—A review. *Journal of Power Sources*. 2015 Mar 1;277:329-42.
- [15]Quan P, Zhou B, Sobiesiak A, Liu Z. Water behavior in serpentine micro-channel for proton exchange membrane fuel cell cathode. *Journal of Power Sources*. 2005 Dec 1;152:131-45.
- [16]Jiao K, Zhou B. Accelerated numerical test of liquid behavior across gas diffusion layer in proton exchange membrane fuel cell cathode. *Journal of Fuel Cell Science and Technology*. 2008 Nov 1;5(4):041011.
- [17]Le AD, Zhou B. A general model of proton exchange membrane fuel cell. *Journal of Power Sources*. 2008 Jul 15;182(1):197-222.
- [18]Le AD, Zhou B, Shiu HR, Lee CI, Chang WC. Numerical simulation and experimental validation of liquid water behaviors in a proton exchange membrane fuel cell cathode with serpentine channels. *Journal of Power Sources*. 2010 Nov 1;195(21):7302-15.
- [19]Wang X, Zhou B. Liquid water flooding process in proton exchange membrane fuel cell cathode with straight parallel channels and porous layer. *Journal of Power Sources*. 2011 Feb 15;196(4):1776-94.
- [20]Kang S, Zhou B, Cheng CH, Shiu HR, Lee CI. Liquid water flooding in a proton exchange membrane fuel cell cathode with an interdigitated design. *International Journal of Energy Research*. 2011 Dec 1;35(15):1292-311.

- [21]Qin Y, Du Q, Yin Y, Jiao K, Li X. Numerical investigation of water dynamics in a novel proton exchange membrane fuel cell flow channel. *Journal of Power Sources*. 2013 Jan 15;222:150-60.
- [22]Qin Y, Li X, Jiao K, Du Q, Yin Y. Effective removal and transport of water in a PEM fuel cell flow channel having a hydrophilic plate. *Applied Energy*. 2014 Jan 1;113:116-26.
- [23]Niu Z, Fan L, Bao Z, Jiao K. Numerical investigation of innovative 3D cathode flow channel in proton exchange membrane fuel cell. *International Journal of Energy Research*. 2018.
- [24]Falcão DS, Pereira JP, Pinto AM. Numerical simulations of anode two-phase flow in Micro-DMFC using the volume of fluid method. *International Journal of Hydrogen Energy*. 2016 Nov 16;41(43):19724-30.
- [25]Kang S, Zhou B. Numerical study of bubble generation and transport in a serpentine channel with a T-junction. *International Journal of Hydrogen Energy*. 2014 Feb 4;39(5):2325-33.
- [26]Kang S, Zhou B, Jiang M. Bubble behaviors in direct methanol fuel cell anode with parallel design. *International Journal of Hydrogen Energy*. 2017 Aug 3;42(31):20201-15.
- [27]Miller C. Liquid water dynamics in a model polymer electrolyte fuel cell flow channel, MSc Thesis, University of Victoria, 2009.
- [28]Wu TC. Two-phase flow in microchannels with application to PEM fuel cells, PhD Dissertation, University of Victoria, 2015.
- [29]Kistler SF. Hydrodynamics of wetting. *Wettability*. 1993;6:311-430.
- [30]Šikalo Š, Wilhelm HD, Roisman IV, Jakirlić S, Tropea C. Dynamic contact angle of spreading droplets: Experiments and simulations. *Physics of Fluids*. 2005 Jun;17(6):062103.

- [31]Mukherjee S, Abraham J. Investigations of drop impact on dry walls with a lattice-Boltzmann model. *Journal of Colloid and Interface Science*. 2007 Aug 15;312(2):341-54.
- [32]Roisman IV, Opfer L, Tropea C, Raessi M, Mostaghimi J, Chandra S. Drop impact onto a dry surface: Role of the dynamic contact angle. *Colloids and Surfaces A: Physicochemical and Engineering Aspects*. 2008 Jun 5;322(1):183-91.
- [33]Jiang M, Zhou B, Wang X. Comparisons and validations of contact angle models. *International Journal of Hydrogen Energy*. 2018 Mar 22;43(12):6364-78.
- [34]Šikalo Š, Tropea C, Ganić EN. Impact of droplets onto inclined surfaces. *Journal of Colloid and Interface Science*. 2005 Jun 15;286(2):661-9.
- [35]Šikalo Š, Ganić EN. Phenomena of droplet–surface interactions. *Experimental Thermal and Fluid Science*. 2006 Nov 30;31(2):97-110.
- [36]Wang X. Gas-liquid phenomena with dynamic contact angle in cathode of proton exchange membrane fuel cells. MASc Thesis, University of Windsor, 2011.
- [37]Fang C, Hidrovo C, Wang FM, Eaton J, Goodson K. 3-D numerical simulation of contact angle hysteresis for microscale two phase flow. *International Journal of Multiphase Flow*. 2008 Jul 31;34(7):690-705.
- [38]Chen J, Tang Y, Zhang W, Wang Y, Qiu L, Zhang X. Computational fluid dynamic simulations on liquid film behaviors at flooding in an inclined pipe. *Chinese Journal of Chemical Engineering*. 2015 Sep 1;23(9):1460-8.
- [39]Zahedi P, Zhang J, Arabnejad H, McLaury BS, Shirazi SA. CFD simulation of multiphase flows and erosion predictions under annular flow and low liquid loading conditions. *Wear*. 2017 Apr 15;376:1260-70.
- [40]ANSYS Fluent Theory Guide 15.0. ANSYS Inc., 2013.

## Appendix B

### PERMISSIONS FOR PREVIOUS PUBLISHED WORKS

#### Chapter 2: Comparisons and Validations of Contact Angle Models

- According to Elsevier's Journal Author Right, the author of the publication retains the right to include it in a thesis or dissertation and the permission is not required, provided it is not published commercially.

#### Chapter 3 (partial): Numerical Study of Droplet Impact on Inclined Surface: Viscosity Effects

##### Order Details

##### ECS transactions

**Order detail ID:** 71685628  
**Order License Id:** 4478420800136  
**ISSN:** 1938-6737  
**Publication Type:** e-Journal  
**Volume:**  
**Issue:**  
**Start page:**  
**Publisher:** ELECTROCHEMICAL SOCIETY  
**Author/Editor:** Electrochemical Society

**Permission Status:**  **Granted**

**Permission type:** Republish or display content  
**Type of use:** Republish in a thesis/dissertation

**Requestor type** Author of requested content

**Format** Print, Electronic

**Portion** chapter/article

**The requesting person/organization** Mengcheng Jiang

**Title or numeric reference of the portion(s)** Numerical Study of Droplet Impact on Inclined Surface: Viscosity Effects

**Title of the article or chapter the portion is from** N/A

**Editor of portion(s)** N/A

**Author of portion(s)**

	Mengcheng Jiang, Biao Zhou
<b>Volume of serial or monograph</b>	83
<b>Issue, if republishing an article from a serial</b>	1
<b>Page range of portion</b>	
<b>Publication date of portion</b>	2018
<b>Rights for</b>	Main product
<b>Duration of use</b>	Life of current edition
<b>Creation of copies for the disabled</b>	no
<b>With minor editing privileges</b>	yes
<b>For distribution to</b>	Worldwide
<b>In the following language(s)</b>	Original language of publication
<b>With incidental promotional use</b>	yes
<b>Lifetime unit quantity of new product</b>	Up to 999
<b>Title</b>	Two-Phase Flows with Dynamic Contact Angle Effects for Fuel Cell Applications
<b>Institution name</b>	University of Windsor
<b>Expected presentation date</b>	Dec 2018

**Note:** This item will be invoiced or charged separately through CCC's **RightsLink** service. [More info](#)

**\$ 0.00**

## VITA AUCTORIS

NAME: Mengcheng Jiang

PLACE OF BIRTH: Zhenjiang, Jiangsu, China

YEAR OF BIRTH: 1993

EDUCATION: Jiangsu Provincial Zhenjiang No.1 High School,  
Zhenjiang, China.  
2008-2011.

Nanjing University of Aeronautics and Astronautics,  
Nanjing, China.  
2011-2015, B. Eng.

University of Windsor, Windsor, ON,  
2016-2018, M.A.Sc.